

Nagaoka University of Technology,
Graduate School of Engineering
Academic Dissertation for Doctor of Philosophy

Materials Design Strategy of
 Ti_2AlC MAX Phase Ceramics
Based on Microstructure Control
and Composition Optimization

Department: Science of Technology Innovation

Program: Doctoral Program for World-leading
Innovative & Smart Education

Name: Naoya Yamaguchi

Student ID number: 16309682

Supervisor: Makoto Nanko Professor

List of contents

List of contents	I
Chapter 1: Introduction	1
1.1 Ceramics materials.....	1
1.2 Machinability of ceramics materials.....	1
1.3 Machinable ceramics	2
1.4 MAX phase ceramics.....	3
1.5 Ti ₂ AlC MAX phase ceramics	4
1.6 Circular economy of Ti ₂ AlC ceramics	4
1.7 Status of social implementation of MAX phase ceramics.....	6
1.8 TRL of Ti ₂ AlC ceramics.....	8
1.9 Materials design strategy for Ti ₂ AlC ceramics.....	8
1.10 Objective and structure of the present thesis	9
References.....	11
Chapter 2: Improvement of oxidation resistance of Ti ₂ AlC ceramics	19
2.1 Introduction.....	19
2.2 Experimental.....	21
2.3 Results.....	22
2.4 Discussion.....	25
2.5 Conclusions.....	30
References.....	30
Chapter 3: Improvement of mechanical strength of Ti ₂ AlC ceramics	44
3.1 Introduction.....	44
3.2 Experimental.....	45
3.2.1 Materials	45
3.2.2 Mechanical tests.....	46

3.3. Results.....	48
3.3.1 Initial microstructural features.....	48
3.3.2 Fracture strength and behavior	50
3.4. Discussion.....	50
3.4.1 Microstructural features of Ti ₂ AlC ceramics.....	50
3.4.2 Fracture mechanics analysis	52
3.5 Conclusions.....	53
References.....	54
Chapter 4: Influences of the cutting damage on Ti ₂ AlC ceramics.....	64
4.1 Introduction.....	64
4.2 Experimental.....	66
4.2.1 Materials	66
4.2.2 Machining conditions	67
4.2.3 Mechanical tests.....	69
4.3 Results.....	71
4.3.1 Initial microstructural features.....	71
4.3.2 Roughness and cutting mode.....	72
4.3.3 Bending strength and behavior	73
4.3.4 Cutting-induced damages	74
4.4 Discussion.....	74
4.4.1 Cutting-induced damage mechanism in the MAX phase	74
4.4.2 Fracture mechanics analysis	75
4.5 Conclusions.....	78
References.....	80
Chapter 5: Materials design strategy for Ti ₂ AlC ceramics for high-temperature components	95
5.1 Introduction.....	95
5.2 Summary of materials design strategy.....	95

5.3 Future of materials design strategy.....	96
References.....	97
Chapter 6: The potential of Ti ₂ AlC ceramics screw components	99
6.1 Introduction.....	99
6.2 Experimental.....	101
6.2.1 Materials	101
6.2.2 Cutting process	102
6.2.3 Mechanical test	102
6.3 Results.....	103
6.3.1 Thread shape of Ti ₂ AlC ceramic nut	103
6.3.2 Mechanical strength of Ti ₂ AlC ceramic nut	103
6.3.3 Thread shape of Ti ₂ AlC ceramic bolt	104
6.3.4 Mechanical strength of Ti ₂ AlC ceramic bolt	104
6.4 Dissection	105
6.5 Conclusions.....	106
References.....	107
Chapter 7: Summary and conclusions.....	117
7.1 Conclusions of the present thesis.....	117
7.2 Future research.....	119
Nomenclature	122
List of tables and figures	124
Tables.....	124
Figures	124
Research activities.....	130
Acknowledgments.....	136

Chapter 1: Introduction

1.1 Ceramics materials

Demands for structural ceramic materials with excellent heat and corrosion resistance are increasing in the energy and environmental fields, as well as academic interests. Ceramic components are still used in a variety of fields. In the energy production industries, ceramics materials are used in products used in high-temperature atmospheres, such as gas turbines, combustors, and nuclear reactors, because of their superior resistance to heat and oxidation. In the industry of physics and industries are used in crucibles for pharmaceuticals and chemical synthesis, chemical pumps, and semiconductor jigs because of their high corrosion resistance to acids, alkalis, and molten metals, their high chemical stability, and their resistance to the formation of impurities [1].

1.2 Machinability of ceramics materials

The high machining cost in the manufacturing process of structural ceramic components is a critical issue to limit the application of these materials [2]. Because ceramic materials are hard and brittle, it is difficult to achieve complex shapes through cutting process. The mechanical damage introduced during cutting contributes to a significant reduction in mechanical strength and strength reliability [3,4]. As well, expensive special tools such as diamond cutting tools must be used for cutting ceramic materials [5]. Other issues include short tool life and the need for highly rigid cutting machines [6]. In general, ceramics are machined by grinding with diamond wheels

rather than cutting [7]. Fabrication of complex-shaped pieces by grinding is difficult and time-consuming. The cutting damage is introduced to the cutting surface of the ceramic material without exception. The resulting subsurface damage must be removed by grinding or lapping to ensure the strength and reliability of ceramic components. Cutting costs may account for 80–96% of the total manufacturing cost of a ceramic component and thus, must be reduced [2].

1.3 Machinable ceramics

There are ceramics that can be machined, called machinable ceramics [8,9]. Typical machinable ceramics include mica and boron nitride. The layered structure of these machinable ceramics suppresses the propagation of cracks even in the event of brittle fracture, allowing machining with minimal damage to the material [8]. However, ordinary machinable ceramics are brittle and have low strength. The machinable ceramics cannot be used for products with severe stresses [9]. The machinable ceramics also have the problem of being difficult to machine to precise dimensions because the machining is based on grain dropout from the surface. For this reason, general machinable ceramics are not used for products with complex shapes. Improving machinable ceramics to be precisely machined with ordinary tools and machine tools and have mechanical strength equivalent to that of ordinary ceramics, the materials would be ideal as materials for ceramic parts. Ti_2AlC MAX phase ceramics are expected to be such a material.

1.4 MAX phase ceramics

In the 1960s, Nowotny's group researched the fabrication of carbides and nitrides and reported more than 100 types of materials. Among them were over 30 materials called "MAX phase ceramics" [14]. Nowotny's group did no further work on MAX phase ceramics. Barsoum's group focused on the $M_{n+1}AX_n$ phase. In 2000, the term " $M_{n+1}AX_n$ phase" was used in their paper [14]. $M_{n+1}AX_n$ was shortened to MAX and became known as MAX phase ceramics.

MAX phase ceramics are layered ternary compounds with the general formula $M_{n+1}AX_n$, where M is a transition metal, A is an A-group element, and X is C or N. Where M stands for a transition metal (Sc, Ti, V, Cr, Mn, Fe, Y, Zr, Nb, Mo, Lu, Hf, Ta or W), A is a group A element (Al, Si, P, S, Cu, Zn, Ga, Ge, As, Pd, Cd, In, Sn, Ir, Au, Tl, Pb or Bi) and X represents C or N [10]. Figure 1-1 shows constituent elements of MAX phase ceramics. MAX phase ceramics have both metallic and ceramic features because of the presence of both metallic and covalent bonds in the crystal [11]. Since Ti_2AlC belongs to this group, it also exhibits both metallic and ceramic properties, including high electrical and thermal conductivity, high thermal shock resistance, lower density than Ni alloys and steels, good high-temperature oxidation resistance and high hardness [12,13]. MAX phase ceramics have a microstructure with crystals piled up like mille-feuille. The most unique feature of MAX phase ceramics is that the materials can be cut with cemented carbide tools [11]. MAX phase ceramics are attracting attention as a new ceramic material that can be used as an alternative to conventional structural ceramics.

1.5 Ti₂AlC MAX phase ceramics

There are various types of MAX phase ceramics depending on the combination of constituent elements. Ti₂AlC MAX phase ceramics have attracted particular attention. The constituent elements of Ti₂AlC ceramics, Ti, Al, and C, are almost non-toxic, relatively inexpensive, and readily available. In addition, Ti₂AlC ceramics have excellent mechanical properties, oxidation resistance, and machinability [13].

According to many literature papers, Ti₂AlC ceramics has a density of 4.06 g/cm³, which is equivalent to that of Al₂O₃, a commonly used ceramic, a Vickers hardness of 6.1 GPa, which is equivalent to that of heat-treated steel, and a fracture toughness of 6.5 MPam^{1/2}, which is equivalent to that of silicon nitride ceramics [14]. When Ti₂AlC is exposed to high-temperature environment, a continuous Al₂O₃ scale is formed on the surface [14]. The Al₂O₃ scale acts as a protective scale and exhibits excellent high-temperature oxidation resistance. In addition, Ti₂AlC ceramics has a self-healing capability that automatically repairs surface cracks in high-temperature environment [15,16]. Figure 3 shows the appearance of machined Ti₂AlC ceramics. Ti₂AlC can be machined into complex shapes. With its excellent mechanical properties for use in severe high-temperature environments, self-healing and machinability with commercial carbide tools, Ti₂AlC is expected to be used not only for general structural ceramic parts but also for various parts in a high-temperature environment.

1.6 Circular economy of Ti₂AlC ceramics

Circular economy concept (CE) has been proposed to achieve Sustainable Development Goals (SDGs). Circular economy means an economy that does not produce waste by reusing/reusing resources at each stage of production, consumption

and disposal and create new industries and businesses at each stage [17]. The achievement of CE will improve the sustainability of society. In order to achieve CE, it is necessary to spread materials with high producibility and long lifetime. Conventional engineering ceramics have high production cost because of polishing for long time. They need smooth surface without cracks for removing surface cracks, which reduce in mechanical strength. Ti_2AlC ceramics is one of the MAX phase ceramics, which is the layered ternary transition metal carbides and nitrides. The non-oxide ceramics have received attentions due to their excellent mechanical properties, their good resistance against high-temperature oxidation and machinability via cemented carbide cutting tools. Ti_2AlC ceramics has been studied as a potential candidate expected to be used in various mechanical components. Roughly machined Ti_2AlC ceramics has as high bending strength as polished ones. This means the Ti_2AlC ceramics has excellent capacity for high-speed machining without subsurface damage leading to decrease their mechanical properties. Machining cost of the Ti_2AlC ceramics is much lower than that of grinding of conventional engineering ceramics with diamond grinding wheels. As well Ti_2AlC ceramics has been reported to have self-healing ability via thermal oxidation process [18]. When using self-healing Ti_2AlC ceramics, surface cracks can be recovered by heat treatment in oxidizing atmosphere. Ti_2AlC ceramics are expected for achieving the SDGs by realizing circular economy.

The formation of CE using Ti_2AlC ceramics is shown below. Ti_2AlC ceramics have good machinability, allowing products to be fabricated at low machining costs; Ti_2AlC ceramic products have high mechanical properties and are easy to reuse and recycle due to their self-healing properties. When Ti_2AlC ceramic products are used in high-temperature environments, their self-healing capability automatically repairs

cracks. In application of Ti_2AlC ceramics at room temperature, it can be reused after self-healing by requesting heating from a heating contractor. The product life is longer than other ceramic products, reducing life cycle costs and energy consumption. In addition, we can offer new business opportunities, such as heat treatment services for self-healing Ti_2AlC ceramic products. Ti_2AlC ceramic products that can no longer be reused are recycled whenever possible. Thus, Ti_2AlC ceramics can be recycled at each production stage, consumption, and disposal, making it an ideal structural ceramic for building CE. To form such CE, Ti_2AlC ceramics must be used in many products. We believe it is essential to promote using Ti_2AlC ceramics in screw parts, which are the most basic mechanical parts. In addition, as the concept of CE using Ti_2AlC ceramics spreads throughout the industry, it is expected that various materials other than Ti_2AlC ceramics will be developed that are suitable for CE formation. This will accelerate material-driven innovation.

1.7 Status of social implementation of MAX phase ceramics

Currently, social implementation of MAX phase ceramics products has not progressed. One of the main reasons why MAX phase ceramics have not been implemented in society is that their important properties as high-temperature materials have not yet been fully clarified. The problem of most important properties, such as oxidation resistance, mechanical strength, and machinability, are shown below.

1.7.1 Problem of oxidation resistance

When it comes to structural elements exposed to high-temperatures, one of their most important properties is high-temperature oxidation resistance as well as high-temperature mechanical strength and creep resistance. However, there is no well-

established understanding of the oxidation properties of Ti_2AlC at high-temperatures. Some sources consider Ti_2AlC to have improved resistance to oxidizing conditions [19-21], while others do not [22-24]. Certain results indicate linear oxidation behavior occurred with the formation of a non-protective TiO_2 scale on the surface of Ti_2AlC after long-term oxidation [21]. To promote the applications of Ti_2AlC in high-temperature components, the oxidation process of Ti_2AlC must be stabilized.

1.7.2 Problems of mechanical strength

Mechanical strength is one of the most important properties of heat-resistant components. Table 1-1 shows a table summarizing the reported bending strength and fracture toughness values of Ti_2AlC ceramics [25-32]. The reported values of bending strength of Ti_2AlC ceramics are scattered (127-432 MPa). To use Ti_2AlC ceramics as a structural component, the variation in mechanical strength must be investigated to compensate for the minimum load capacity.

1.7.3 Problems of machinability

Although the machining of MAX phase ceramics has been reported [33–36], the damage mechanism of the cutting surface and the influence of the cutting damage has not been elucidated. Ti_2AlC ceramics has good machinability. However, cutting damage can be introduced to the cutting surface of Ti_2AlC . In particular, microcracks on the surface can reduce the mechanical strength of Ti_2AlC ceramics [37,38]. A systematic evaluation of the influences of cutting damage on mechanical strength a necessary for the application of Ti_2AlC ceramic products.

1.8 TRL of Ti₂AlC ceramics

Increasing the Technology Readiness Level (TRL) are very important for the implementation of Ti₂AlC ceramics in industries. TRLs are a method for estimating the maturity of technologies during the acquisition phase of a program. The use of TRLs enables consistent, uniform discussions of technical maturity across different types of technology [39]. TRLs consists of a scale 1 to scale 9. The current target for Ti₂AlC MAX phase ceramics as CE-friendly materials is regarded as TRL2 (Potential Application Validated). Figure 1-2 shows TRL of Ti₂AlC ceramics. TRL2 can be achieved by comparing the various properties of Ti₂AlC with other materials to clarify the range of applications. The range of application of Ti₂AlC ceramics is high temperature components. To achieve a TRL level of 2 or higher Materials design strategy for properties important for high-temperature components need to be established.

1.9 Materials design strategy for Ti₂AlC ceramics

Material design is described in the Mechanical Engineering Dictionary as follows: A method of predicting specifically the composition, microstructure, manufacturing methods, etc., to obtain a material with desired properties. The materials design of ceramics can be classified into three types [40]. The first stage is the material exploration stage. The first stage is the material structure that satisfies the required use. This stage is called material property optimization design. The second stage is the material practical application stage. The second phase is the synthesis phase, in which the synthesis method to realize the structure indicated in the first phase is shown. This stage is called the synthesis method optimization design. The third stage is the selection of optimal materials from the material bank. The third stage is when the use of each

company's products has been accumulated in the database. There have been many studies on the fundamental properties of Ti_2AlC ceramics. However, there is no systematic discussion of the multiple material properties of Ti_2AlC . The effect of different synthesis conditions on the properties of Ti_2AlC is not clarified in detail. The material design of Ti_2AlC ceramics is currently in the first stage. Optimization of microstructure and synthesis is required to progress to the second and third phases. The second stage of material design may allow us to reach a TRL level of 2 or higher, since Ti_2AlC products can be easily developed. Figure 1-3 show a synergy map of my research on Ti_2AlC ceramics. This research aims to build a circular economy by improving the TRL of Ti_2AlC ceramics and implementing various Ti_2AlC ceramics products in society. The research has also been conducted on applying Ti_2AlC ceramics to kitchen utensils and industrial products used at room temperature. The focus of this thesis is on establishing material design guidelines for high-temperature components, where Ti_2AlC ceramics are particularly expected to be applied.

1.10 Objective and structure of the present thesis

The main objective of this thesis is to establish a materials design strategy for Ti_2AlC MAX phase ceramics and to fabricate products based on the strategy. The influence of microstructure control and composition adjustment on high-temperature oxidation resistance, mechanical strength, and machinability were investigated to establish a materials design strategy for high-temperature components. The materials design strategy was then applied to screw parts and their properties were evaluated. Figure 1-4 shows structure of the present thesis.

In Chapter 1: Introduction, the actual conditions of social implementation of Ti₂AlC ceramic products and concept of materials design strategy are described. Literature survey of Ti₂AlC is also described.

In Chapter 2: Improvement of oxidation resistance of Ti₂AlC, the mechanism of non-protective oxidation of Ti₂AlC ceramics and methods to stabilize oxidation resistance were discussed.

In Chapter 3: Improvement of mechanical strength of Ti₂AlC, the effect of microstructure on mechanical strength of Ti₂AlC ceramics and methods to control mechanical strength were discussed.

In Chapter 4: Influences of the cutting damage on Ti₂AlC, the machinability of Ti₂AlC ceramics and the change in mechanical strength after machining were investigated. Influence of machining damage to mechanical strength are discussed with fracture mechanics.

In Chapter 5: Materials design strategy for Ti₂AlC as a high-temperature component, a material design strategy for high-temperature components was developed based on the results of Chapters 2, 3, and 4. In Chapter 6: The Potential of Ti₂AlC Screw Components, the properties of Ti₂AlC ceramic bolts and nuts fabricated based on the material design strategy were evaluated.

In chapter 7: Summary and conclusions, the conclusions of the present thesis described and future prospects for Ti₂AlC ceramics research are discussed.

References

- [1] C. Barry Carter, M. Grant Norton, *Ceramic Materials Science and Engineering*, Springer,(2013) pp1-775
- [2] S. Malkin, T.W. Hwang, Grinding mechanisms for ceramics, *CIRP Annals* 45 (1996) 569–580.
- [3] R.W. Rice, J.J. Mecholsky, P.F. Becher, The effect of grinding direction on flaw character and strength of single crystal and polycrystalline ceramics, *J. Mater. Sci.* 16 (1981) 853–862.
- [4] M. Gruber, A. Leitner, I. Kraveva, D. Kiener, P. Supancic, R. Bermejo, Understanding the effect of surface flaws on the strength distribution of brittle single crystals, *J. Am. Ceram. Soc.* 101 (2018) 5705–5716.
- [5] K. Kanda, S. Takehana, S. Yoshida, R. Watanabe, S. Takano, H. Ando, F. Shimakura, Application of diamond-coated cutting tools, *Surf. Coat. Technol.* 73 (1995) 115–120.
- [6] V. Bharathi, A.R. Anilchandra, S.S. Sangam, S. Shreyas, S.B. Shankar, A review on the challenges in machining of ceramics, *Mater. Today Proc.*, 46 (2021) 1451–1458.
- [7] J.S. Reed, J.S. Reed, *Principles of ceramics processing*, John Wiley & Sons, New York, 1995.
- [8] J.B. Davis, D.B. Marshall, R.M. Housley, P.E.D. Morgan, Machinable ceramics containing rare-earth phosphates, *J. Am. Ceram. Soc.* 81 (1998) 2169–2175.
- [9] K. Chihiro Y. Akira, Machinability of High-Strength Porous Silicon Nitride Ceramics, *Journal of the Ceramic Society of Japan.* 106 (1998) 1135–1137.

- [10] J. Gonzalez-Julian, Processing of MAX phases: From synthesis to applications, *J. Am. Ceram. Soc.* 104:2 (2021) 659-690.
- [11] M.W. Barsoum, The $M_{N+1}AX_N$ phases: A new class of solids; Thermodynamically Stable Nanolaminates. *Prog. Solid. State Ch.* 28:1-4 (2000) 201-281.
- [12] M. Radovic, M. W. Barsoum, MAX Phases: Bridging the gap between Metals and Ceramics, *Bull. Am. Ceram. Soc.* 92:3 (2013) 20-27.
- [13] X. Wang, Y. Zhou, Layered Machinable and Electrically Conductive Ti_2AlC and Ti_3AlC_2 Ceramics: a Review, *J. Mater. Sci. Technol.* 26:5 (2010) 385-416.
- [14] M.W. Barsoum, MAX phases: properties of machinable ternary carbides and nitrides, Wiley-VCH, Weinheim, 2013.
- [15] T. Osada, A. Watabe, J. Yamamoto, J.C. Brouwer, C. Kwakernaak, S. Ozaki, S. van der Zwaag, W.G. Sloof, Full strength and toughness recovery after repeated cracking and healing in bone-like high temperature ceramics, *Sci. Rep.* 10 (2020) 18990.
- [16] S. Li, G. Song, K. Kwakernaak, S. van der Zwaag, W.G. Sloof, Multiple crack healing of a Ti_2AlC ceramic, *J. Eur. Ceram. Soc.* 32 (2012) 1813–1820.
- [17] A. Murray, K. Skene, K. Haynes, The Circular Economy: An Interdisciplinary Exploration of the Concept and Application in a Global Context, *Journal of Business Ethics.* 140:3 (2017) 369–380.
- [18] S. Li, G. Song, K. Kwakernaak, S. van der Zwaag, W.G. Sloof, Multiple crack healing of a Ti_2AlC ceramic, *J. Eur. Ceram. Soc.* 32 (2012) 1813–1820.

- [19] Haftani M, Saeedi Heydari M, Baharvandi H, et al. Studying the oxidation of Ti_2AlC MAX phase in atmosphere: A review. *Int. J. Refract. Hard. Met.* 61 (2016) 51-60.
- [20] S. Basu, N. Obando, A. Gowdy, et al., Long-Term Oxidation of Ti_2AlC in Air and Water Vapor at 1000-1300°C Temperature Range, *J. Electrochem. Soc.* 159:2 (2012) 90-96.
- [21] D. Tallman, B. Anasori, M. Barsoum, et al., A Critical Review of the Oxidation of Ti_2AlC , Ti_3AlC_2 and Cr_2AlC in Air, *Mater. Res. Lett.* 1:3 (2013) 115-125.
- [22] M.W. Barsoum, N. Tzenov, A. Procopio, et al., Oxidation of $Ti_{n+1}AlX_n$ ($n = 1-3$ and $X = C, N$) II. Experimental Result, *J. Electrochem Soc.* 148:8 (2001) 551-562.
- [23] S. Badie, D. Sebold, R. Vaßen, et al., Mechanism for breakaway oxidation of the Ti_2AlC MAX phase, *Acta Mater.* 215 (2021) 117025.
- [24] Z. Lin, M. Li, J. Wang, et al., Influence of water vapor on the oxidation behavior of Ti_3AlC_2 and Ti_2AlC , *Scr. Mater.* 58:1 (2008) 29-32.
- [25] B. Yao, S. Li, W. Zhang, W. Yu, Y. Zhou, S. Fan, G. Bei, Self-healing behavior of Ti_2AlC at a low oxygen partial pressure, *Journal of Advanced Ceramics* 11:11 (2022) 1687–1695.
- [26] X. Xie, R. Yang, Y. Cui, Q. Jia, C. Bai, Fabrication of textured Ti_2AlC lamellar composites with improved mechanical properties, *J Mater Sci Technol.* 38 (2020) 86–92.
- [27] T. Thomas, C. Zhang, A. Sahu, P. Nautiyal, A. Loganathan, T. Laha, B. Boesl, A. Agarwal, Effect of graphene reinforcement on the mechanical properties of Ti_2AlC ceramic fabricated by spark plasma sintering, *Materials Science and Engineering: A.* 728 (2018) 45–53.

- [28] L. Cai, Z. Huang, W. Hu, S. Hao, H. Zhai, Y. Zhou, Fabrication, mechanical properties, and tribological behaviors of Ti_2AlC and $Ti_2AlSn_{0.2}C$ solid solutions, *Journal of Advanced Ceramics* 2017 6:2 (2017) 90–99.
- [29] Y. Bai, X. He, C. Zhu, G. Chen, Microstructures, Electrical, Thermal, and Mechanical Properties of Bulk Ti_2AlC Synthesized by Self-Propagating High-Temperature Combustion Synthesis with Pseudo Hot Isostatic Pressing, *J. Am. Chem. Soc.* 95:1 (2012) 358-364.
- [30] R. Benitez, W.H. Kan, H. Gao, M. O’Neal, G. Proust, A. Srivastava, M. Radovic, Mechanical properties and microstructure evolution of Ti_2AlC under compression in 25–1100 °C temperature range, *Acta Mater.* 189 (2020) 154–165.
- [31] F.L. Meng, Y.C. Zhou, J.Y. Wang, Strengthening of Ti_2AlC by substituting Ti with V, *Scr Mater.* 53 (2005) 1369–1372.
- [32] X. Wang, Y. Zhou, Solid–liquid reaction synthesis and simultaneous densification of polycrystalline Ti_2AlC , *International Journal of Materials Research.* 93 (2002) 66–71.
- [33] M.W. Barsoum, MAX phases: properties of machinable ternary carbides and nitrides, Wiley-VCH, Weinheim, 2013.
- [34] N. Yamaguchi, M. Okada, K. Yanagisawa, Y.-L. Kuo, M. Nanko, New material for screws –The potential of Ti_2AlC ceramic screw components, *J. Jpn. Soc. Precis. Eng.* 87 (2021) 353–357.
- [35] S.S. Hwang, S.C. Lee, J.H. Han, D. Lee, S.W. Park, Machinability of Ti_3SiC_2 with layered structure synthesized by hot pressing mixture of TiC_x and Si powder, *J. Eur. Ceram. Soc.* 32 (2012) 3493–3500.

- [36] C.F. Hu, Y.C. Zhou, Y.W. Bao, Material removal and surface damage in EDM of Ti_3SiC_2 ceramic, *Ceram. Int.* 34 (2008) 537–541.
- [37] S. Malkin, T.W. Hwang, Grinding mechanisms for ceramics, *CIRP Annals* 45 (1996) 569–580.
- [38] R.W. Rice, J.J. Mecholsky, P.F. Becher, The effect of grinding direction on flaw character and strength of single crystal and polycrystalline ceramics, *J. Mater. Sci.* 16 (1981) 853–862.
- [39] M. Héder, *The Innovation Journal: The Public Sector Innovation*, *Innov. J.* 22:3 (2017) 1-23
- [40] Materials Science Society of Japan, *Around the Relation between Materials and Their Functions*, Shokabo Co., Ltd., 1995.

Table 1-1 Summarizing the reported mechanical strength of Ti₂AlC ceramics

Ref.	Sintering					Grain size			Minor phase	Mechanical strength			Year
	Molar ratio	Method	Temp. /°C	Press. /MPa	Time /h	Long /µm	Short /µm	Aspect ratio		Bending strength /MPa	Flacture toughness /MPa · m ^{1/2}	Vickers Strengths/GPa	
25	Ti : Al : TiC 1 : 1.1 : 0.9	HP	1450	30	1	~45	~6	-	TiC	375	-	-	2022
26	TiAl : TiC 1 : 0.95	HP	1200	30	2	16.0 ± 11.1	6.5 ± 3.6	2.5	TiAlx, Al ₂ O ₃	316±30	6.2±0.4	4.0±0.1	2020
27	Commercial Maxthal 211	SPS	1200	60	7 min	~32	~12	-	Ti ₃ AlC ₂ , TiC	127.67	-	-	2018
28	Ti : Al : TiC 1 : 1.1 : 0.9	HP	1450	28	0.5	20	8	-	Ti ₃ AlC ₂	430 ± 32	-	5.55 ± 0.69	2017
29	Ti : Al : C 2.9 : 2 : 1	Fast	-	420	12s	~5	~3	-	TiAl	432±12	6.5±0.2	5.8±0.5	2012
30	Ti : Al : TiC : C 1.5 : 1 : 0.5 : 0.5	HP	1400	30	1	-	-	-	Ti ₃ AlC ₂	384	7	4.2	2007
31	Ti : Al : C 2 : 1 : 0.9	CP	1450	20	1	41 ± 12	16 ± 4	-	Ti ₃ AlC ₂ , Al ₂ O ₃	261	6	3.5	2005
32	Ti : Al : C 2 : 1 : 1	HP	1400	30	1	50-100	10-20	-	-	275	6.5	2.8	2002

$M_{n+1}AX_n$
(n=1,2,3..)

}

M... Transition metal

A... A-group element

X... Carbon and/or Nitrogen

H																	He
Li	Be											B	C	N	O	F	Ne
Na	Mg											Al	Si	P	S	Cl	Ar
K	Ca	Sc	Ti	V	Cr	Mn	Fe	Co	Ni	Cu	Zn	Ga	Ge	As	Se	Br	Kr
Rb	Sr	Y	Zr	Nb	Mo	Tc	Ru	Rh	Pd	Ag	Cd	In	Sn	Sb	Te	I	Xe
Cs	Ba	La	Hf	Ta	W	Re	Os	Ir	Pt	Au	Hg	Tl	Pb	Bi	Po	At	Rn
Fr	Ra	Ac	Rf	Db	Sg	Bh	Hs	Mt	Ds	Rg	Cn	Nh	Fl	Mc	Lv	Ts	Og

Figure 1-1 Constituent elements of MAX phase ceramics.

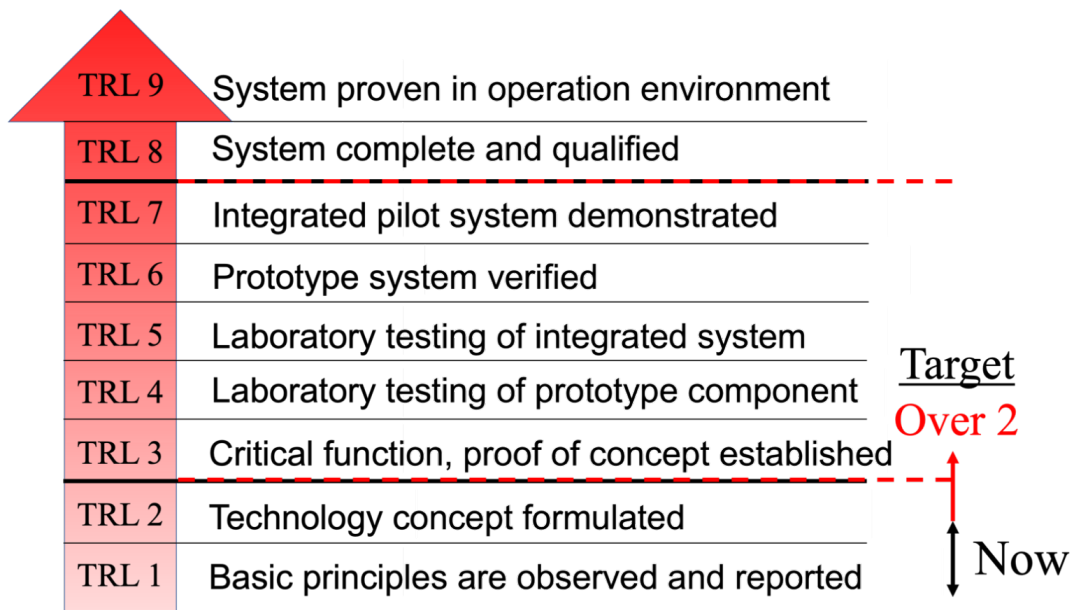


Figure 1-2 TRL of Ti₂AlC ceramics.

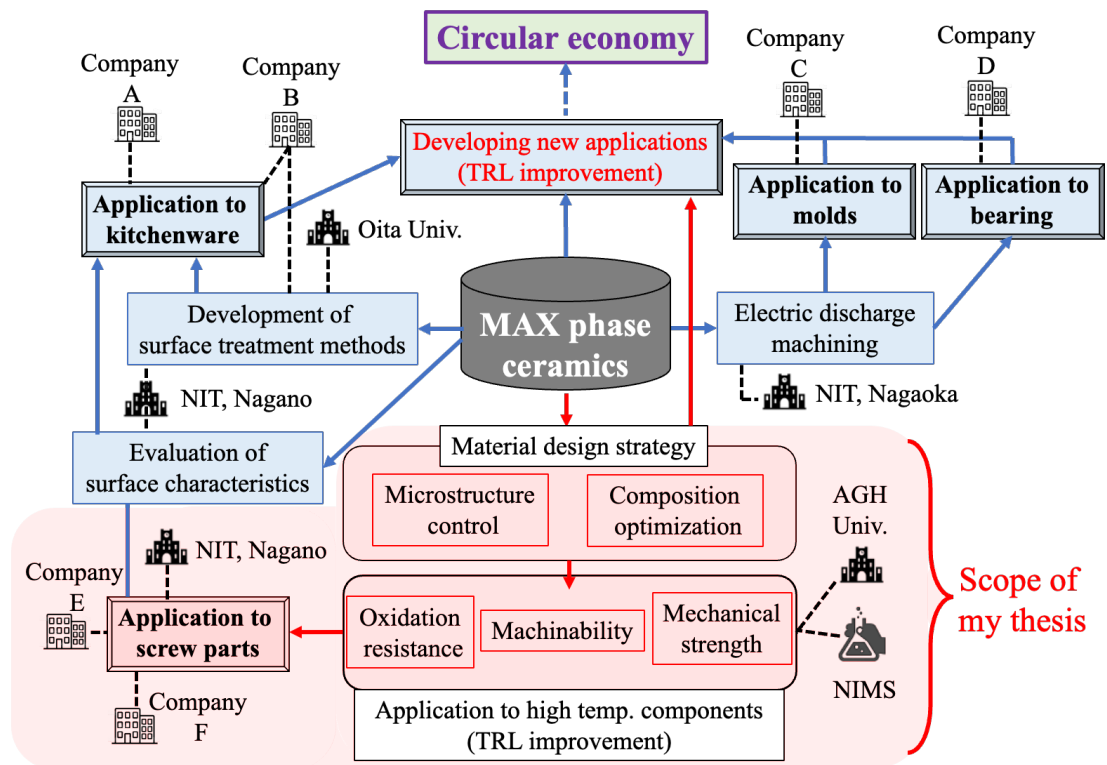


Figure 1-3 Synergy map of my research on Ti₂AlC ceramics.

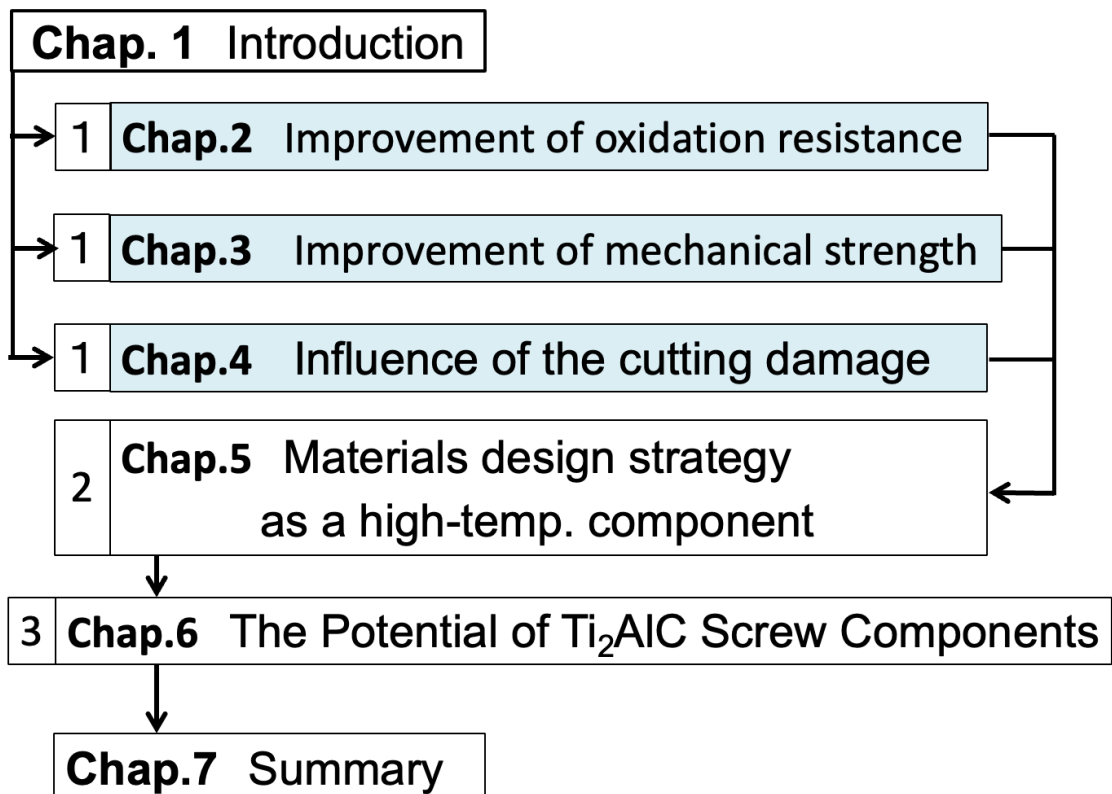


Figure 1-4 Structure of the thesis.

Chapter 2: Improvement of oxidation resistance of Ti₂AlC ceramics

2.1 Introduction

MAX phase ceramics have both metallic and ceramic features because of the presence of both metallic and covalent bonds in the crystal [1-2]. Since Ti₂AlC belongs to this group, it also exhibits both metallic and ceramic properties, including high electrical and thermal conductivity, high thermal shock resistance, lower density than Ni alloys and steels, good high-temperature oxidation resistance and high hardness [3-4]. Ti₂AlC has been studied as a potential candidate for application in various mechanical components used at high temperatures as well as room temperature. The mechanical strength of Ti₂AlC decreases sharply at around 900°C, at this point, Ti₂AlC undergoes the brittle-to-ductile transition (BDT) [5]. The application of Ti₂AlC ceramics would therefore be limited at temperatures higher than the BDT temperature.

When it comes to structural elements exposed to high-temperatures, one of their most important properties is high-temperature oxidation resistance as well as high-temperature mechanical strength and creep resistance. However, there is no well-established understanding of the oxidation properties of Ti₂AlC ceramics at high temperatures. Some sources consider Ti₂AlC to have improved resistance to oxidizing conditions [6-8], while others do not [9-11]. Certain results indicate linear oxidation behavior occurred with the formation of a non-protective TiO₂ scale on the surface of Ti₂AlC after long-term oxidation [8]. To promote the applications of Ti₂AlC in high-temperature components, the oxidation process of Ti₂AlC must be stabilized.

The chemical composition of Ti_2AlC may affect its oxidation behavior. Because Ti_2AlC is a line phase [12], every commercial Ti_2AlC powder contains other phases, such as TiC , Ti_3AlC_2 or $TiAl_3$ [13]. This makes it impossible to study the oxidation behavior of Ti_2AlC using samples with a controlled phase ratio. Because the protective scale that forms on Ti_2AlC is Al_2O_3 , its continued growth requires a sufficient Al supply during high-temperature oxidation. Al-rich phases like $TiAl_3$ may improve the oxidation resistance of Ti_2AlC ceramics.

High-temperature oxidation of $TiAl$ with poor oxidation resistance leads to the formation of oxide scale including the rutile polymorph of TiO_2 and Al_2O_3 [14]. This oxidation behavior is very similar with Ti_2AlC ceramics with poor oxidation resistance. Improvements of oxidation resistance on $TiAl$ have been studied with several techniques. As one of the common methods for improving the oxidation resistance of $TiAl$, addition of Nb is applied [15], which would inhibit the growth of the TiO_2 scale on the surface of $TiAl$ and subsequently facilitates the formation of a continuous Al_2O_3 scale. The oxidation resistance of Ti_2AlC doped with Nb was studied by Donchev et al. [16], and they reported a decreased oxidation rate, indicating the protective action of a Nb addition. However, the mechanism underlying the beneficial effect of Nb on the oxidation properties of Ti_2AlC is unclear in some cases. Adding Nb to Ti_2AlC with low Al content may not necessarily improve its oxidation resistance to a very significant degree, since this compound is in itself highly susceptible to oxidation [17].

In this study, influences of varying the Al content and Nb addition on the oxidation behavior of Ti_2AlC in air at 800 and 1200°C was investigated to establish a material design strategy that would optimize the high-temperature oxidation resistance of Ti_2AlC ceramics.

2.2 Experimental

Commercial Ti, Al, and C powders were mixed in Ti:Al:C molar ratios of 2:1:0.9, 2:1.2:0.9, and 2:1.5:0.9, with the corresponding samples receiving the designations A11, A11.2 and A11.5, respectively. Some A11 and A11.2 samples had 5% of their Ti content replaced with Nb; these samples are referred to as A11Nb and A11.2Nb. The particle size and purity of the raw powders were as follows: 38 μm and 99.9% for Ti, 3 μm and 99.9% for Al, 1-2 μm for C and 45 μm for Nb (Kojundo Chemical Laboratory). The powder mixture was placed in an alumina container and annealed for 16 h in vacuum at 1300°C. The reacted powder underwent phase identification by means of X-ray diffraction (XRD, Rigaku corporation MiniFlex 600, using monochromatic $\text{CuK}\alpha$ radiation). A11 is categorized as Al-poor Ti_2AlC , and A11.2 and A11.5 are categorized as Al-rich Ti_2AlC . Table 2-1 shows the symbol and category of each sample investigated in the present study. The synthesized powder was consolidated over 15 min using a pulsed electric current sintering technique with a graphite die at 1300°C, in vacuum, and under a uniaxial pressure of 30 MPa. The phases present in the sintered samples were also identified with XRD. The relative density of the samples reached at least 98% of the theoretical one. Samples for oxidation experiments were cut into a small quarter-circle shape with a radius of 7.5 mm and a thickness of 3 mm using a diamond saw. All samples for the oxidation tests were ground with SiC abrasive paper with varying grit (up to 3000), and then subsequently polished with 3 and 1 μm diamond slurry to ensure that the surface of each sample had undergone the same preparation. The samples were heated for times ranging from 2 to 14 d in an electric furnace with laboratory air at 800°C and 0.5 to 7 d in an electric furnace with laboratory air at 1200°C. For

thermogravimetric analyses (TGA), the samples were cut into small rectangles with dimensions of $10 \times 5 \times 1 \text{ mm}^3$ using a diamond saw. The oxidation kinetics were evaluated at 800°C in ambient air, over a period of 150 h using a thermogravimetric apparatus which enabled the continuous monitoring of the weight with an accuracy of to 10^{-6} g (MK2 Vacuum Head Microbalance, CI Electronics Ltd, UK). The phase compositions of the samples were analyzed by means of XRD. The samples were mounted in resin and cut with a diamond cutting wheel for cross-sectional observations by means of scanning electron microscopy (SEM), performed using a FEI Nova NanoSEM 200 microscope coupled with an EDAX Genesis XM2 system required for the analysis of chemical composition via energy-dispersive X-ray spectroscopy (EDS).

2.3 Results

Figure 2-1 shows the XRD patterns of the sintered samples. The XRD graphs with the bottom portion enlarged were smoothed to remove noise. The main peaks in these XRD patterns were identified as originating from Ti_2AlC . In the case of Al-poor Ti_2AlC , peaks attributed to Ti_3AlC_2 , TiAl_3 and TiC were also observed. The patterns recorded for the remaining samples had minor peaks originating from Ti_3AlC_2 and TiAl_3 . The surface images of Ti_2AlC samples with different Al molar ratios after oxidation at 800°C for up to 14 d in air are shown in Figure 2-2. Yellowish scales had formed on the surface of Al-poor Ti_2AlC . After the oxidation test, the surface of the AlNb sample differed in color from that of its counterpart without Nb addition.

Figure 2-3 shows the XRD patterns obtained for sintered samples from all groups after 14 d of oxidation. The main peaks in XRD patterns of Al-rich and Nb-doped oxide samples were identified as originating from Ti_2AlC . The minor peaks were attributed to

TiO₂ and different polymorphs of Al₂O₃. Because peaks observed for α -Al₂O₃, θ -Al₂O₃, and γ -Al₂O₃ are similar and they all have low intensity, it was impossible to precisely determine the type of Al₂O₃. Figure 2-4 shows SEM and EDS images of the cross-sections of samples Al1.2, Al1Nb and Al1.2Nb after 14 d of isothermal oxidation in laboratory air at 800°C. The EDX element mapping of the surface of Al-rich and Nb-doped samples after 14 d of oxidation clearly shows aluminum and oxygen. The conducted XRD, SEM, and EDX observations indicate that an Al₂O₃ scale with a thickness of less than 1 μ m was formed on these samples. The predominant phase in the oxide scales formed in the case of all Al-rich and Nb-doped samples was Al₂O₃. Figure 2-2 shows the Nb-doped Ti₂AlC after the oxidation test. The surface of the Al1Nb sample differed in color from its counterpart without Nb addition. Oxidation time did not affect the appearance of any of the Al-rich and Nb-doped samples to a significant degree. Figure 2-5 shows SEM and EDS images of the surface of Al1.2Nb after 150 h of isothermal oxidation in laboratory air at 800°C. Needle-like growth of Al₂O₃ was clearly observable only on the surface of Al1.2Nb. Figure 2-6 shows the cross-sectional SEM and EDX images of the Al-poor sample after 14 d of oxidation. The results of XRD, SEM, and EDX investigations indicate that rutile had formed on the scale's surface, while Al₂O₃ and TiO₂ had formed underneath it. For this sample, thickness increased linearly with oxidation time, reaching approximately 120 μ m after 14 d (Figure 2-7). The oxide scale formed on all Al-poor samples was determined to consist of rutile with poor oxidation resistance.

Figure 2-8 shows the kinetics of isothermal oxidation for all of the sintered samples in a linear plot representing mass gain per unit area in a function of time. The data show that the oxidation kinetics of the samples approximately obeys the parabolic

rate law. The slowest constituent process that determines the oxidation rate is therefore the diffusion of reagents in the oxidation product. The largest increase in the mass of the corrosion product was observed for the A11 sample, while the A11.2Nb sample was characterized by the smallest increase. The parabolic oxidation rate constants, k_p of the samples determined using the Pilling-Bedworth equation are listed in Table 2-2 [18]. As can be seen, the parabolic rate constant of oxidation decreases with increasing aluminum content. The oxidation rate constants of the A11 and A11.5 samples are different by as much as one order of magnitude. On the other hand, the addition of niobium reduced the k_p values by another order of magnitude, further improving the oxidation resistance of the A11Nb and A11.2Nb samples.

Figure 2-9 shows the surface images of Ti_2AlC samples with different Al molar ratios after oxidation at $1200^\circ C$ for up to 2 d in air are shown in Figure 2-2. Yellowish scales had formed on the surface of all samples oxidized for 2 d. Figure 2-10 shows the surface images of A11.2Nb after oxidation at $1200^\circ C$ for up to 7 d in air. After the oxidation test, the surface of the A11.2Nb sample differed in color from that of its counterpart without Nb addition. Figure 2-11 shows the XRD pattern obtained for A11.2Nb after 14 d of oxidation at $1200^\circ C$. The main peaks in XRD patterns Nb-doped oxide samples were identified as originating from Ti_2AlC and $\alpha-Al_2O_3$. The minor peaks were attributed to TiO_2 . Figure 2-12 shows SEM and EDS images of the cross-sections of A11.2Nb after 7 d of isothermal oxidation in laboratory air at $1200^\circ C$. The EDX element mapping of the surface of A11.2Nb after 7 d of oxidation at $1200^\circ C$ clearly shows aluminum and oxygen. The conducted XRD, SEM, and EDX observations indicate that an Al_2O_3 scale with a thickness of less than $9 \mu m$ was formed on A11.2Nb. Figure 2-13 shows the kinetics of isothermal oxidation for A11.2Nb in a linear plot

representing mass gain per unit area in a function of time. The data show that the oxidation kinetics of Al_{1.2}Nb at 1200°C approximately obeys the parabolic rate law.

2.4 Discussion

The Al₂O₃ oxide scale formed on the surface of Al-rich Ti₂AlC such as Al 1.2 and Al 1.5 and Nb-doped one can be considered a protective layer, even though its thickness was below 1 μm even after 14 d of oxidation. This is demonstrated by the lower oxidation resistance of Al-poor Ti₂AlC, which had a main TiO₂ scale on its surface and a non-continuous Al₂O₃ scale beneath it. It is evident that the dispersion of an Al-rich phase and doping with Nb are effective at improving the oxidation resistance of Ti₂AlC ceramics.

Brumm and Grabke stated that the oxidation rate depends on the oxide phase formed on the alloy; γ -Al₂O₃, θ -Al₂O₃, and α -Al₂O₃ have been observed, and the growth of each of these phases was associated with different k_p values [19].

Figure 2-14 shows the k_p values of Ti₂AlC determined in the present study compared with those of NiAl reported by Brumm and Grabke [19]. The k_p value for Al₂O₃ growth on Ti₂AlC ceramics at 800°C in the cited study is similar to those for γ -Al₂O₃ or θ -Al₂O₃. The k_p of Al_{1.2} was slightly higher than that of other Al-rich and Nb-doped samples because of partial non-protective oxidation of the Al_{1.2} sample's corners. Non-protective oxidation tends to occur at the corners of Ti₂AlC samples [10]. The supply of Al is limited at this location because of the small area of the lower part. When a continuous Al₂O₃ scale is formed on a protruding part such as a corner, the Al₂O₃ scale may crack due to growth stress [13]. Needle-like Al₂O₃ was observed on the surface of Al_{1.2}Nb oxidized at 800°C for 150 hours. The needle-like Al₂O₃ were

sparsely present in some places and did not form dense colonies. Mechanism of the formation of needle-like shape is explained by the stress generated by the transformation from γ to θ - Al_2O_3 . When γ - Al_2O_3 transforms into θ - Al_2O_3 , the sample volume decreases by 1.7% [20]. The reduced volume causes tensile stress in the θ - Al_2O_3 layer and compressive stress in the γ - Al_2O_3 layer formed on top. Ando et al. reported that a possible mechanism is that the $\langle 111 \rangle$ plane shifts in the $\langle 112 \rangle$ direction to form twins that relieve compressive stress generated in the γ - Al_2O_3 grain near the transition interface from γ to θ - Al_2O_3 [20]. The twin boundary serves as a preferential diffusion path for Al, and the twinned part preferentially grows outward, resulting in a needle shape.

Needle-like crystals of γ - Al_2O_3 or θ - Al_2O_3 may form on the surface when Al_2O_3 -forming materials are oxidized at low temperatures of 500-800°C as well [21-23]. The shape of the Al_2O_3 grains and the comparison of k_p indicates that the Al_2O_3 scale formed on Ti_2AlC at 800°C should be considered to be γ - Al_2O_3 or θ - Al_2O_3 .

When γ - Al_2O_3 transforms into θ - Al_2O_3 , the sample volume decreases by 1.7%; the transformation from θ - Al_2O_3 to α - Al_2O_3 is associated with a decrease of 12.3% [20]. The volume reduction caused by the change of the Al_2O_3 phase causes tensile stress and leads to the cracking of the scale. This phenomenon may cause decrease in the oxidation resistance of Ti_2AlC . The formation mechanism of Al_2O_3 should therefore be considered when designing Ti_2AlC with excellent oxidation resistance in mind. The k_p value for Al_2O_3 growth on $\text{Al}_{1.2}\text{Nb}$ at 1200°C in the cited study is similar to those for α - Al_2O_3 . The α - Al_2O_3 scale can be formed by heating at approximately 1200°C. When manufacturing Ti_2AlC ceramic products in high-temperature environments, it is

recommended that high-temperature heat treatment be used to heal cracks by self-healing and form α -Al₂O₃ scale.

The following tendencies can be observed during the oxidation of Al-rich Ti₂AlC. A continuous Al₂O₃ scale forms under a non-continuous TiO₂ scale as the material starts to oxidize. Since the diffusion coefficient of Al in Ti₂AlC is much faster than that of Ti, the Al₂O₃ scale on top of Ti₂AlC becomes thin and non-continuous [24]. When continuous Al₂O₃ does not form in the initial oxidation stage, its subsequent formation is accompanied by the formation of TiO₂ [25]. The rate at which this non-continuous TiO₂ scale grows is faster than the growth rate of Al₂O₃ [26], and its underlying mechanism is the outward diffusion of Ti through the grain boundaries of the discontinuous Al₂O₃ scale, made possible because the diffusion coefficient of O in the TiO₂ particles is smaller than that of Ti [27]. TiO₂ forms on the surface, and Al₂O₃ forms underneath it. In order for the Al₂O₃ scale to be continuous, the supply of Al from Ti₂AlC needs to be sufficient. The formation of a continuous Al₂O₃ scale suppresses the formation of the TiO₂ scale.

The oxidation of Al-poor Ti₂AlC takes a different course, similar to that observed for Al-poor TiAl. The oxide scale that forms in this case consists mostly of rutile and Al₂O₃ located underneath it, and it does not provide significant protection against oxidation [14]. The supply of Al to the surface is insufficient to allow the formation of the Al₂O₃ scale. Ti is oxidized into TiO₂ and its volume increases, which destroys the Al₂O₃ scale. In order for the oxidation resistance of Ti₂AlC to be improved, it is therefore necessary to ensure that the supply of Al is sufficient and that the growth of the TiO₂ layer is inhibited.

Al-rich Ti_2AlC had high oxidation resistance owing to the development of an Al_2O_3 scale. The Al-rich phase ($TiAl_3$) supplied the needed Al, allowing the continuous Al_2O_3 scale to form and improve the material's resistance to oxidation. In addition to increasing the amount of Al, the supply of Al for Ti_2AlC can also be improved by shortening the Al supply path. Al atoms in Ti_2AlC can migrate more easily in the outward direction along grain boundaries and the base planes than other atoms during high-temperature oxidation [24]. Yu et al. reported that obtaining finer Ti_2AlC grains facilitates Al diffusion and thus the development of the Al_2O_3 scale, which is yet another way in which the oxidation resistance of Ti_2AlC can be improved [28]. There are various ways to reduce grain size in Ti_2AlC , including the use of a finer starting powder or pinning with fine impurity particles. In addition to using a finer starting powder, the preparation process can also be optimized by applying a lower sintering temperature, which yields Ti_2AlC with a high concentration of Al.

Some results concerning the oxidation of Ti_2AlC show that linear kinetics lead to poor oxidation resistance after long-term oxidation [8]. In such conditions, Al-depletion zones in Ti_2AlC develop as the Al is drained by the formation of the continuous Al_2O_3 scale, and after a sufficiently long time of oxidation or if cycles are involved Al-rich Ti_2AlC may be affected in much the same way as the material with low Al content. An additional method to prevent non-protective oxidation of Ti_2AlC is required for long-term use.

This was precisely the rationale for the addition of Nb. When Nb^{5+} , which has a higher valence than Ti^{4+} , is added to TiO_2 , the number of oxygen vacancies in TiO_2 decreases [29], and the growth of TiO_2 is suppressed. The defect reaction equation is expressed, as follows:



The concentration of Nb dissolution in TiO_2 to decrease oxygen vacancies at which the oxygen ion vacancies in TiO_2 disappear is estimated to be $\text{Ti:Nb} = 1:0.04$ [15]. Addition of 5 mol% Nb into Ti in Ti_2AlC ceramics would be sufficient to fill the oxygen ion vacancies in TiO_2 . The cause of non-protective oxidation was the destruction of the Al_2O_3 scale because of the growth of TiO_2 . Inhibition of TiO_2 growth by adding Nb is one of the factors that improve oxidation resistance.

Adding more Nb (10 mol%) to TiAl than the solid solution limit in TiO_2 may further improve oxidation resistance [15,30]. However, when Nb is added to TiAl in large amounts (15 mol% or more), Nb_2O_5 and TiNb_2O_7 scales are formed, and oxidation resistance is reduced [15,30]. The oxidation resistance of Ti_2AlC may also be further improved by increasing the amount of Nb added; the optimal amount of Nb is yet to be determined. In the present study, Nb_2O_5 and TiNb_2O_7 were not observed in the samples after oxidation experiments.

The higher Al concentration and the addition of Nb have a remarkable effect to increase the oxidation resistance of the Ti_2AlC ceramics, which is a property of fundamental importance from the perspective of its eventual applications. Non-protective oxidation did not occur in $\text{Al}_{1.2}\text{Nb}$ after oxidation at 1200°C for 7 d. Such modifications are therefore necessary for the stable operation of components manufactured from this material in conditions that involve high temperatures.

2.5 Conclusions

The oxidation behavior of Ti_2AlC with various Al concentrations and with or without Nb addition was investigated in air at 800 and 1200°C for periods ranging from 0.5 to 14 d. Ti_2AlC powder samples were synthesized for different molar ratios of Al and amounts of added Nb. Al-poor Ti_2AlC was characterized by low oxidation resistance due to the formation of a TiO_2 scale that did not reduce the oxidation rate. Nb-doped Ti_2AlC and samples with higher Al contents exhibited far superior resistance to oxidation owing to the formation of a protective Al_2O_3 scale. The addition of Nb improved oxidation resistance even in the case of the Ti_2AlC sample with the lowest Al content. Non-protective oxidation did not occur in Al-rich and Nb doped Ti_2AlC ceramics after oxidation at 1200°C for 7 d.

References

- [1] J. Gonzalez-Julian, Processing of MAX phases: From synthesis to applications, *J. Am. Ceram. Soc.* 104:2 (2021) 659-690.
- [2] M. W. Barsoum, The $M_{N+1}AX_N$ phases: A new class of solids; Thermodynamically Stable Nanolaminates, *Prog. Solid. State Ch.* 28:1-4 (2000) 201-281.
- [3] M. Radovic, M.W. Barsoum, MAX Phases: Bridging the gap between Metals and Ceramics, *Bull. Am. Ceram. Soc.* 92:3 (2013) 20-27.
- [4] X. Wang, Y. Zhou, Layered Machinable and Electrically Conductive Ti_2AlC and Ti_3AlC_2 Ceramics: a Review. *J. Mater. Sci. Technol.* 26:5 (2010) 385-416.
- [5] Y. Bai, X. He, R. Wang, et al., High temperature physical and mechanical properties of large-scale Ti_2AlC bulk synthesized by self-propagating high temperature

combustion synthesis with pseudo hot isostatic pressing, *J. Eur. Ceram. Soc.* 33:13-14 (2013) 2435-2445.

[6] M. Haftani, M. Saeedi Heydari, H. Baharvandi, et al., Studying the oxidation of Ti_2AlC MAX phase in atmosphere: A review, *Int. J. Refract. Hard. Met.* 61(2016) 51-60.

[7] S. Basu, N. Obando, A. Gowdy, et al., Long-Term Oxidation of Ti_2AlC in Air and Water Vapor at 1000-1300°C Temperature Range, *J. Electrochem. Soc.* 159:2 (2012) 90-96.

[8] D. Tallman, B. Anasori, M. Barsoum, et al., A Critical Review of the Oxidation of Ti_2AlC , Ti_3AlC_2 and Cr_2AlC in Air, *Mater. Res. Lett.* 1:3 (2013) 115-125.

[9] M.W. Barsoum, N. Tzenov, A. Procopio, et al., Oxidation of $Ti_{n+1}AlX_n$ ($n = 1-3$ and $X = C, N$) II. Experimental Results, *J. ElectrochemSoc.* 148:8 (2001) 551-562.

[10] S. Badie, D. Sebold, R. Vaßen, et al., Mechanism for breakaway oxidation of the Ti_2AlC MAX phase, *Acta Mater.* 215 (2021) 117025.

[11] Z. Lin, M. Li, J. Wang, et al., Influence of water vapor on the oxidation behavior of Ti_3AlC_2 and Ti_2AlC , *Scr. Mater.* 58:1 (2008) 29-32.

[12] V. Witusiewicz, B. Hallstedt, A. Bondar, et al., Thermodynamic description of the Al-C-Ti system, *J. Alloys Compd.* 623 (2015) 480-496.

[13] S. Badie, A. Dash, Y. Sohn, et al., Synthesis, sintering, and effect of surface roughness on oxidation of submicron Ti_2AlC ceramics, *J. Am. Ceram. Soc.* 104:4 (2021) 1669-1688.

[14] R. Reddy, X. Wen, M. Divakar, Isothermal oxidation of TiAl alloy, *Metall. Mater. Trans. A.* 32 (2001) 2357-2361.

- [15] M. Yoshihara, K. Miura, Effects of Nb addition on oxidation behavior of TiAl. *Intermetallics*, 3:5 (1995) 357-363.
- [16] A. Donchev, M. Schütze, E. Ström, et al., Oxidation behaviour of the MAX-phases Ti_2AlC and $(Ti, Nb)_2AlC$ at elevated temperatures with and without fluorine treatment, *J. Eur. Ceram. Soc.* 39:15 (2019) 4595-4601.
- [17] X. Li, X. Xie, J. Gonzalez-Julian, et al., Mechanical and oxidation behavior of textured Ti_2AlC and Ti_3AlC_2 MAX phase materials, *J. Eur. Ceram. Soc.* 40:15 (2020) 5258-5271.
- [18] S. Mrowec, T. Werber, *Modern scaling-resistant materials*. Washington DC: National of Standards and National Science Foundation; 1982.
- [19] M. Brumm, H. Grabke, The oxidation behaviour of NiAl-I. Phase transformations in the alumina scale during oxidation of NiAl and NiAl-Cr alloys, *Corros. Sci.* 33:11 (1992) 1677-1690.
- [20] A. Andoh, S. Taniguchi, T. Shibata, TEM Observation of Al_2O_3 Scales Formed on Al-deposited Fe-Cr-Al Alloy Foil, *Tetsu-to-Hagane*. 84 (1998) 43-48.
- [21] N. Yamaguchi, T. Kakeyama, T. Yoshioka, et al., Effect of the Third Elements on High Temperature Oxidation Resistance of $TiAl_3$ Intermetallic Compounds, *Mater. Trans.* 43:12 (2002) 3211-3216.
- [22] A. Eliassi, M. Ranjbar, Application of Novel Gamma Alumina Nano Structure for Preparation of Dimethyl ether from Methanol, *Int. J. Nanosci. Nanotechnol.* 10:1 (2014) 13-26.
- [23] M. Abdollahifar, M. Zamani, E. Beiygie, et al., Synthesis of micro-mesopores flowerlike $\gamma-Al_2O_3$ nano-architectures, *J. Serbian Chem. Soc.* 79:8 (2014) 1007-1017.

- [24] J. Wang, Y. Zhou, T. Liao, et al., A first-principles investigation of the phase stability of Ti_2AlC with Al vacancies, *Scr. Mater.* 58:3 (2008) 227-230.
- [25] X. Wang, Y. Zhou. High-Temperature Oxidation Behavior of Ti_2AlC in Air. *Oxid. Met.* 59:3-4 (2003) 303-320.
- [26] J. Smialek J. Kinetic aspects of Ti_2AlC MAX phase oxidation. *Oxid. Met.* 83:3-4 (2015) 351-366.
- [27] H. Yang, Y. Pei, J. Rao, et al., High temperature healing of Ti_2AlC : On the origin of inhomogeneous oxide scale, *Scr. Mater.* 65:2 (2011) 135-138.
- [28] W. Yu, M. Vallet, B. Levraut, et al., Oxidation mechanisms in bulk Ti_2AlC : Influence of the grain size, *J. Eur. Ceram. Soc.* 40:5 (2020) 1820-1828.
- [29] J. Lin, L. Zhao, G. Li, et al., Effect of Nb on oxidation behavior of high Nb containing TiAl alloys, *Intermetallics.* 19:2 (2011) 131-136.
- [30] M. Yoshihara, N. Imamura, E. Kobayashi, et al., Oxidation resistance and effects of the heat treatment under low partial pressure oxygen atmosphere in intermetallic compound TiAl containing Nb, *J. Japan Inst. Metals.* 57:5 (1993) 574-581.

Table 2-1 Sample symbols and categories.

Ti : Al : C : Nb	Symbols	Category name
2 : 1 : 0.9 : 0	Al1	Al-poor
2 : 1.2 : 0.9 : 0	Al1.2	Al-rich
2 : 1.5 : 0.9 : 0	Al1.5	
1.9 : 1 : 0.9 : 0.1	Al1Nb	Nb-doped
1.9 : 1.2 : 0.9 : 0.1	Al1Nb	

Table 2-2 Parabolic rate constants of oxidation (k_p) of all samples determined after 150 h of isothermal oxidation in laboratory air at 800°C.

Samples	$k_p / \text{g}^2 \text{cm}^{-4} \text{s}^{-1}$	Category name
Al1	1.6×10^{-12}	Al-poor
Al1.2	3.1×10^{-13}	Al-rich
Al1.5	1.0×10^{-13}	
Al1Nb	6.4×10^{-14}	Nb-doped
Al1.2Nb	2.7×10^{-14}	

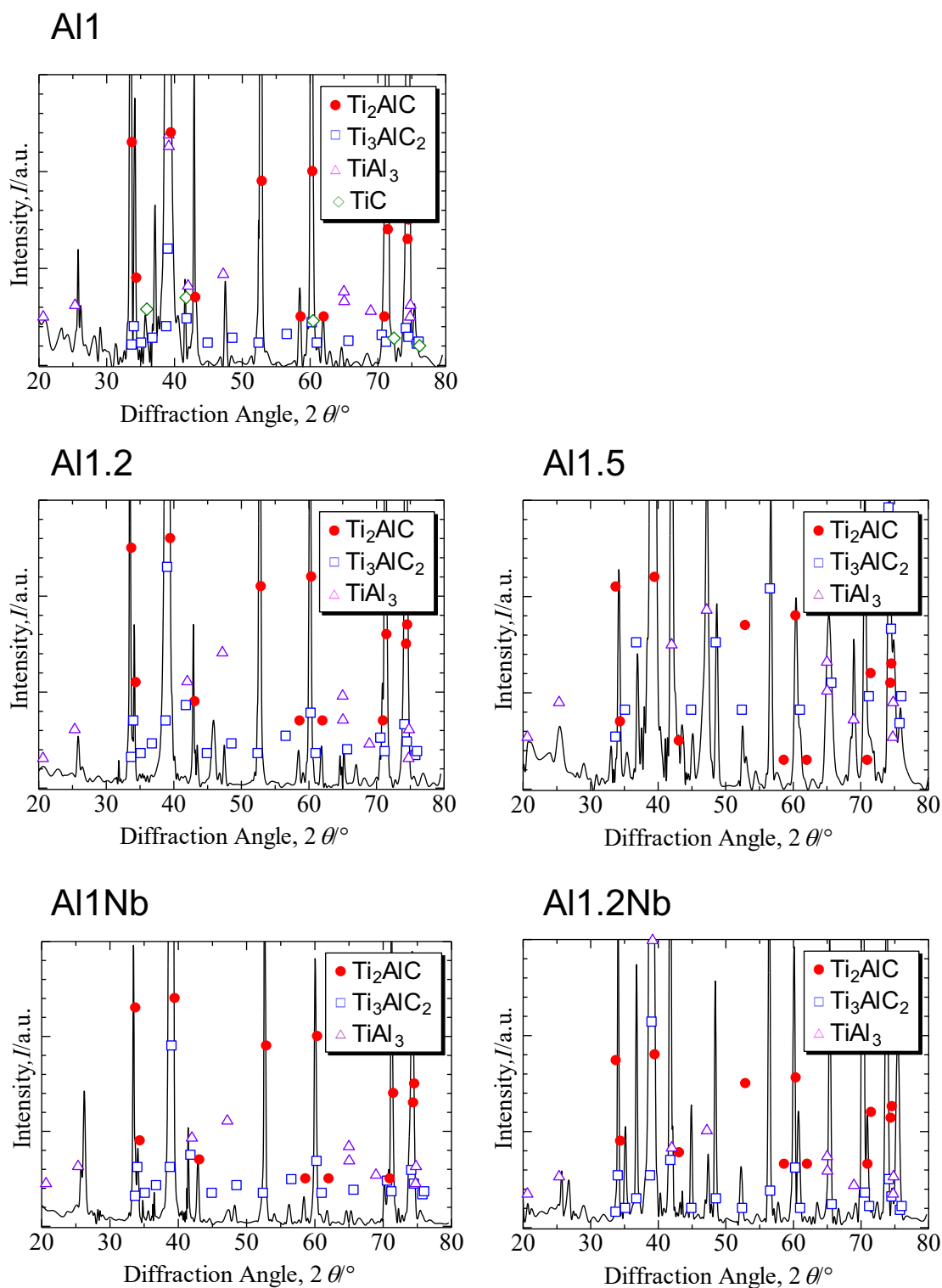


Figure 2-1 X-ray diffraction patterns recorded for bulk samples: Al1, Al1.2, Al1.5, Al1Nb and Al1.2Nb.




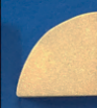

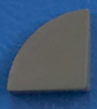














Ti:Al:C +Nb	2 d	4 d	7 d	14 d
A11				
A11.2				
A11.5				
A11Nb				
A11.2Nb				

Figure 2-2 Magnified images of Ti_2AlC and Nb-doped Ti_2AlC samples with various Al molar ratios after 2-14 d of isothermal oxidation in laboratory air at $800^\circ C$.

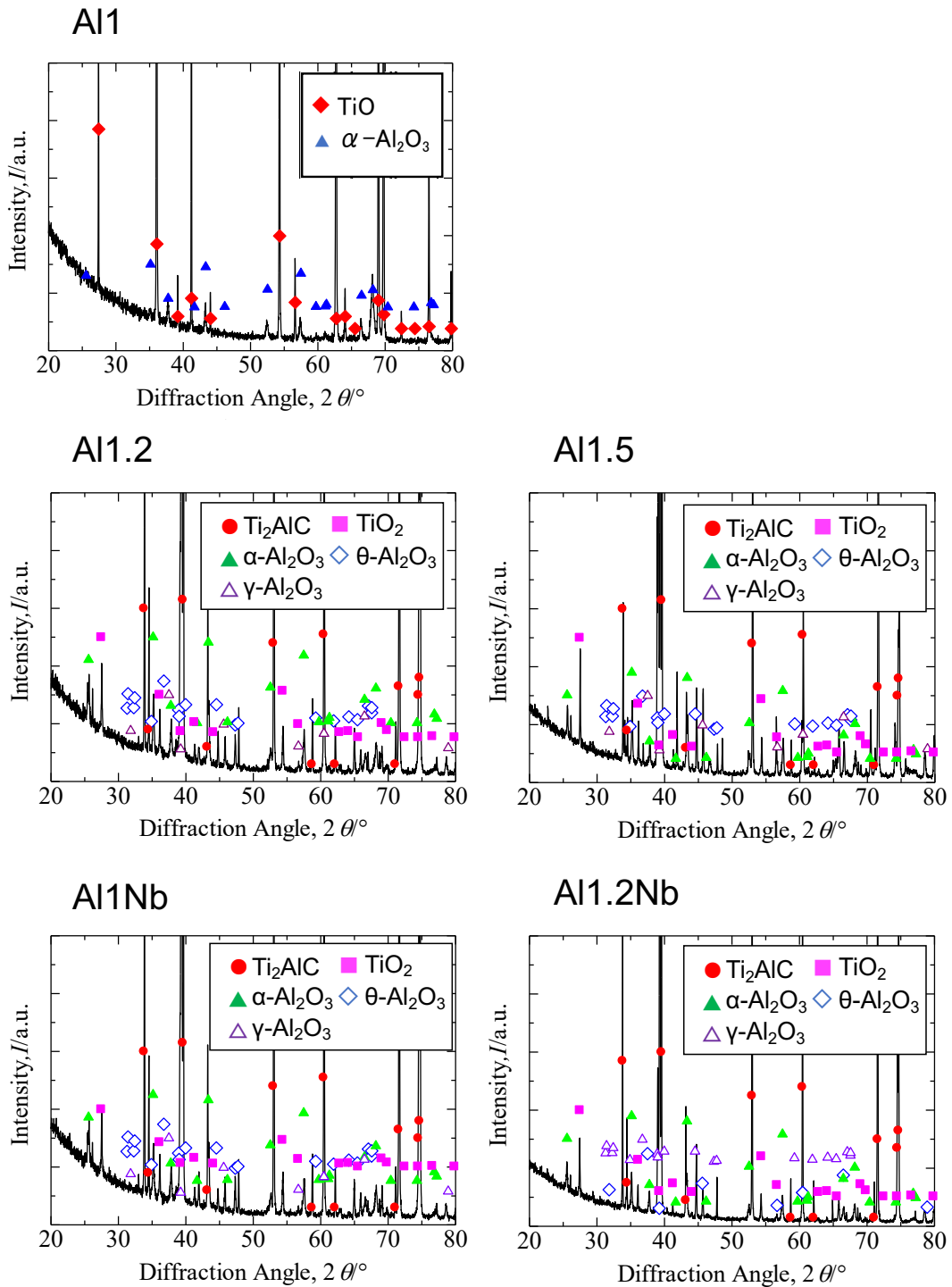


Figure 2-3 X-ray diffraction patterns recorded for samples Al1, Al1.2, Al1.5, Al1Nb and Al1.2Nb after 14 d of isothermal oxidation in laboratory air at 800°C.

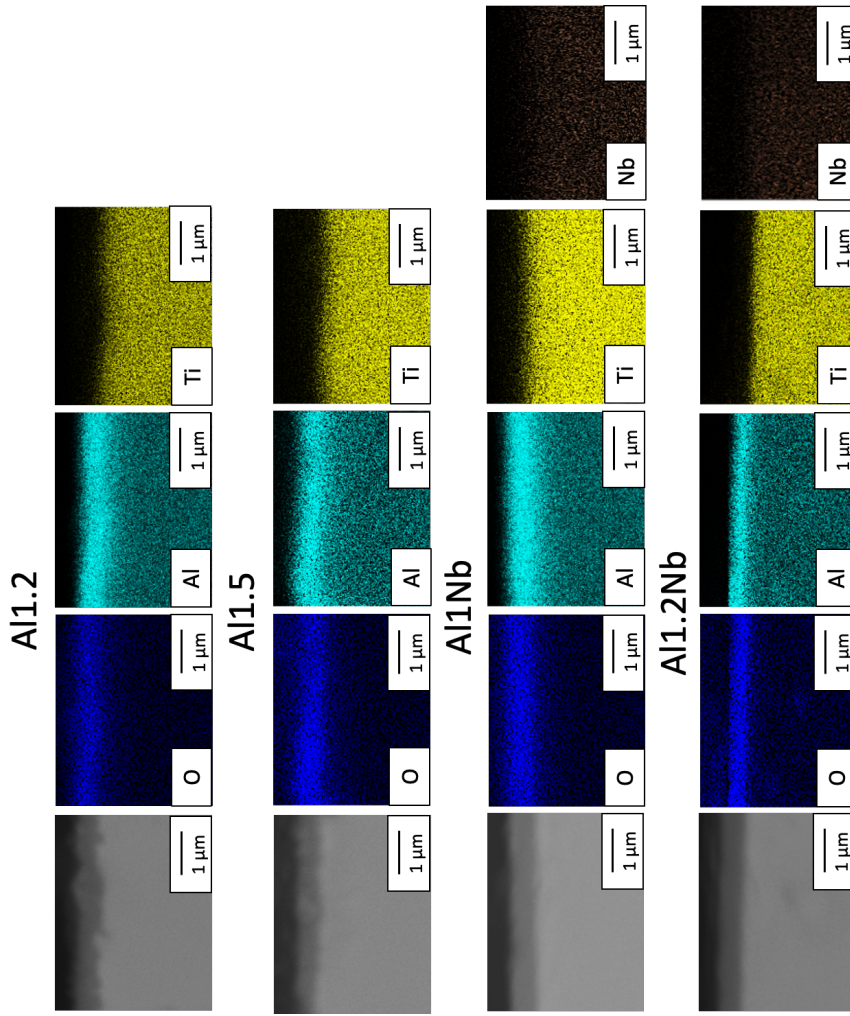


Figure 2-4 SEM and EDS images of the cross-sections of samples Al1.2, Al1Nb and Al1.2Nb after 14 d of isothermal oxidation in laboratory air at 800°C.

Al1.2Nb Surface

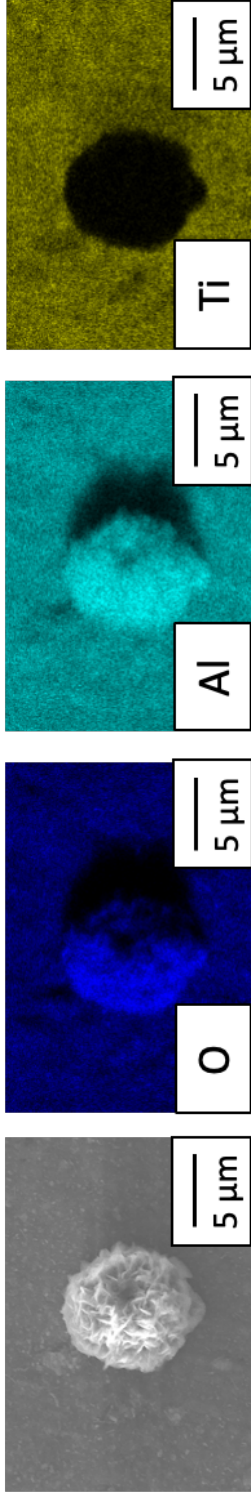


Figure 2-5 SEM and EDS images of the surface of Al1.2Nb after 14 d of isothermal oxidation in laboratory air at 800°C.

Al1

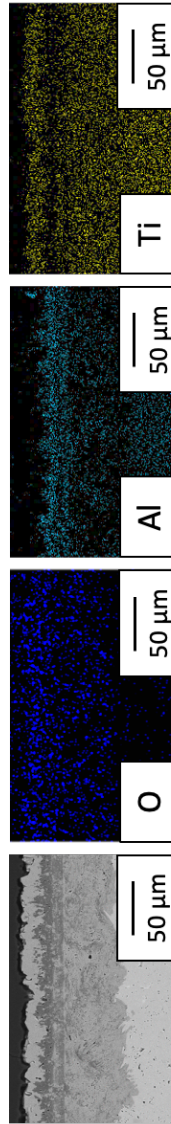


Figure 2-6 SEM and EDS images of the cross-sections of Al1 after 14 d of isothermal oxidation in laboratory air at 800°C.

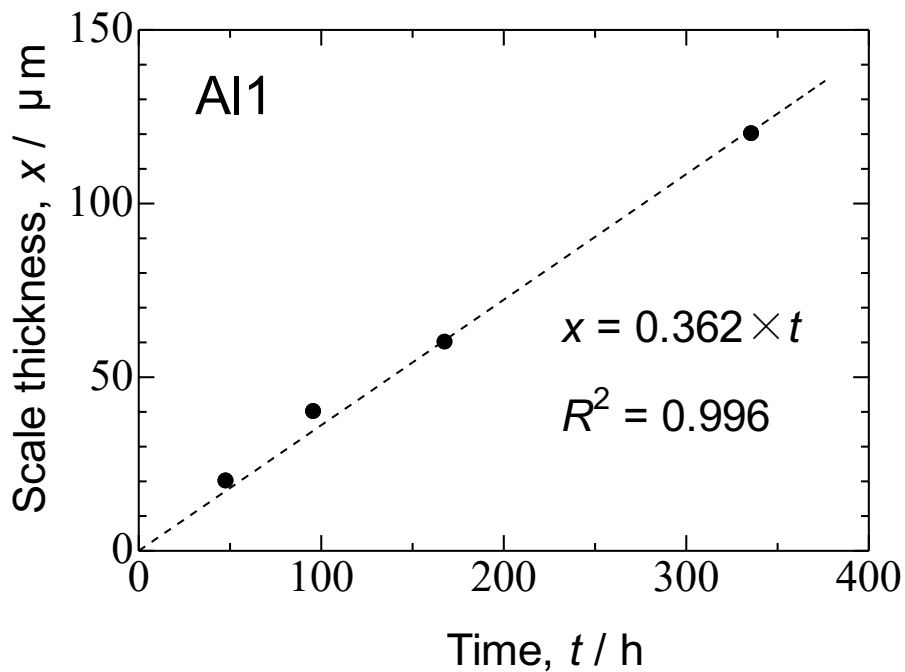


Figure 2-7 Oxide scale thickness (x) versus time (t) for Al1 oxidized at 800°C for over 14 d.

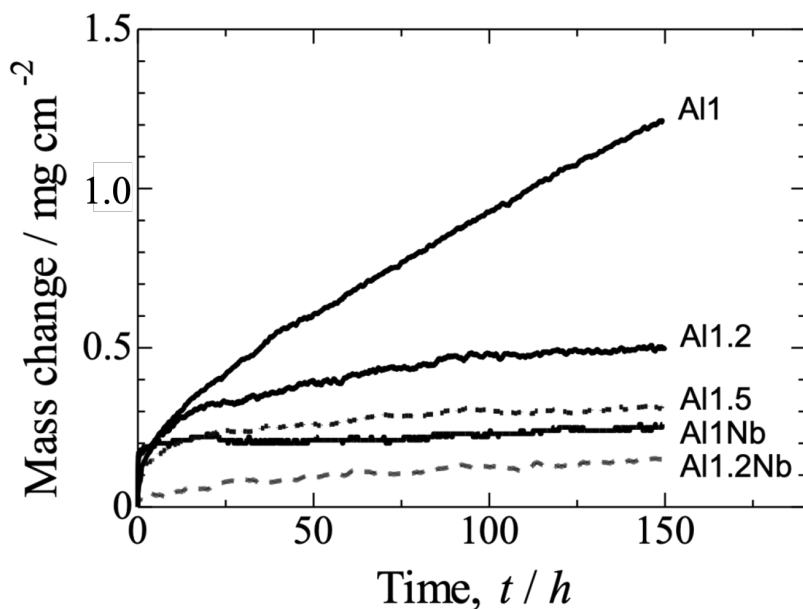


Figure 2-8 Oxidation kinetics for all investigated samples over 150 h of isothermal oxidation in laboratory air at 800°C , presented in a linear plot.










Ti:Al:C	0.5 d	1 d	2 d
Al1			
Al1.2			
Al1.5			

Figure 2-9 Magnified images of Ti_2AlC samples with various Al molar ratios after 0.5-2 d of isothermal oxidation in laboratory air at $1200^{\circ}C$.

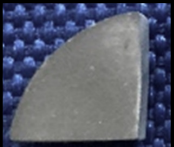


Ti:Al:C:Nb	1 d	4 d	7 d
Al1.2Nb			

Figure 2-10 Magnified images of $Al_{1.2}Nb$ with various Al molar ratios after 1-7 d of isothermal oxidation in laboratory air at $1200^{\circ}C$.

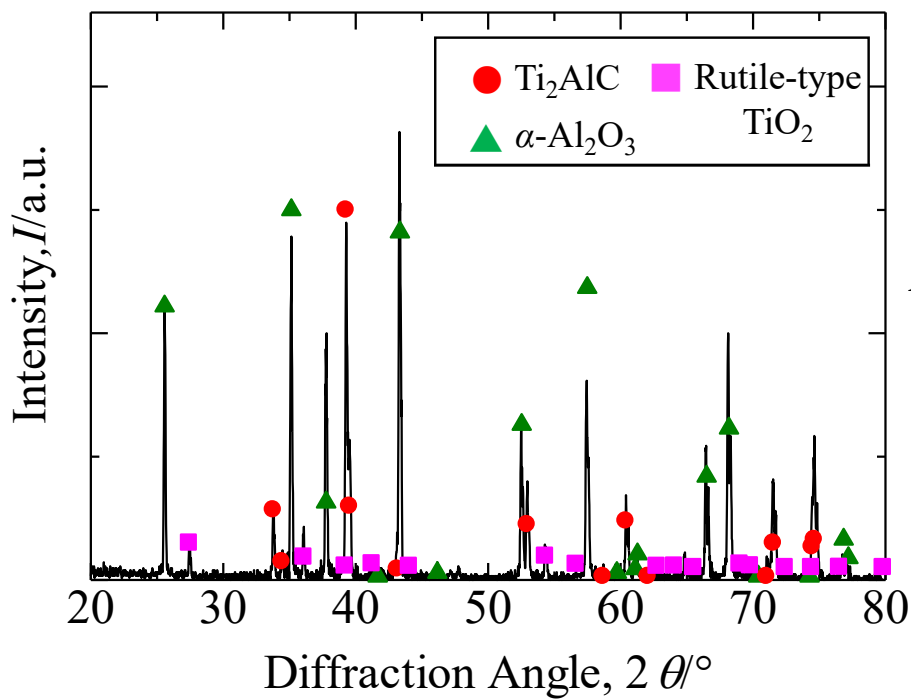


Figure 2-11 X-ray diffraction patterns recorded for A11.2Nb after 7 d of isothermal oxidation in laboratory air at 1200°C.

A11.2Nb

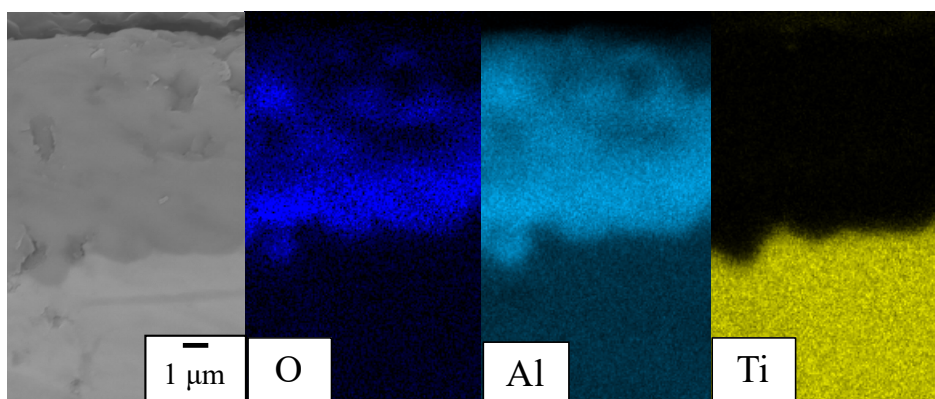


Figure 2-12 SEM and EDS images of the cross-sections of A11.2Nb after 7 d of isothermal oxidation in laboratory air at 1200°C.

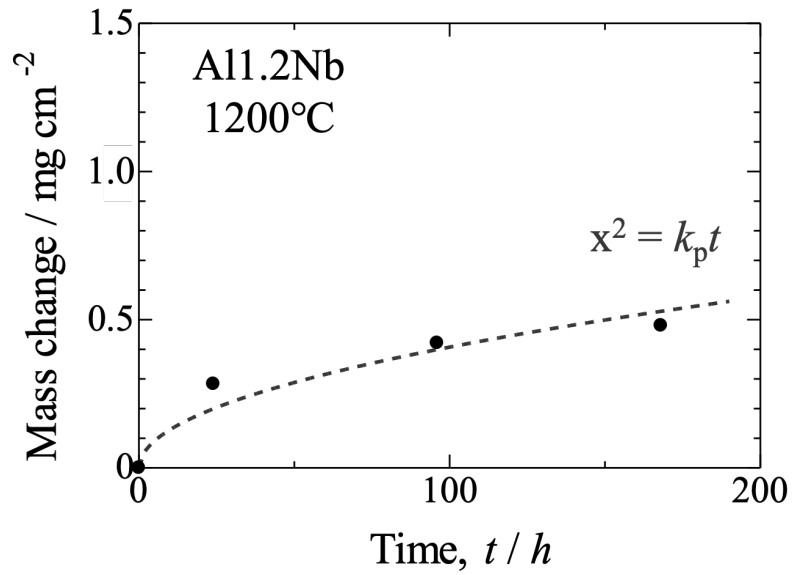


Figure 2-13 Oxidation kinetics for Al1.2Nb over 168 h of isothermal oxidation in laboratory air at 1200°C, presented in a linear plot.

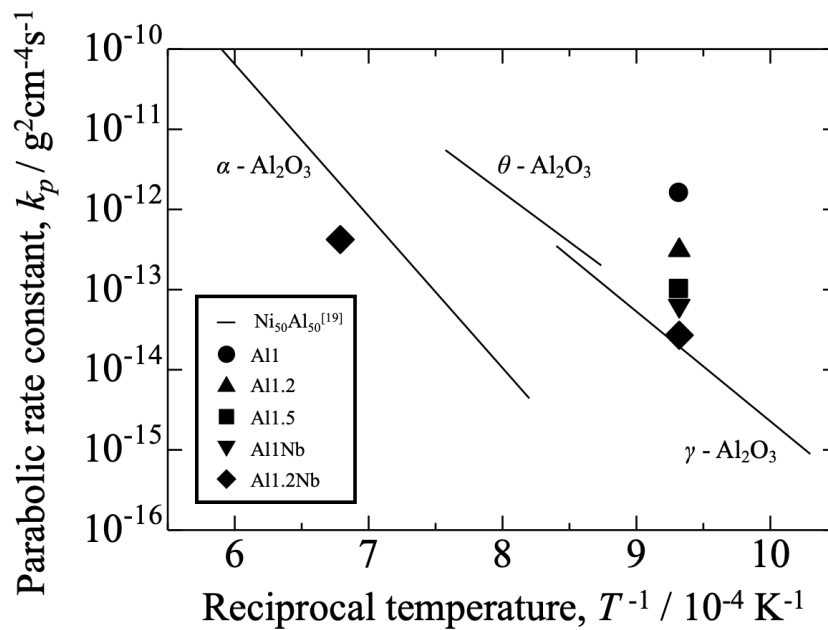


Figure 2-14 Arrhenius plot showing the parabolic rate constants determined for the oxidation of $Ni_{50}Al_{50}$ [19] and the k_p values determined in the present experiment (Table 2-2).

Chapter 3: Improvement of mechanical strength of Ti₂AlC ceramics

3.1 Introduction

Ti₂AlC MAX phase ceramics have been reported to have high mechanical strength and oxidation resistance. Therefore, Ti₂AlC ceramics is expected to be applied to high-temperature components. In Chapter 2, methods to improve the oxidation resistance of Ti₂AlC ceramics were discussed. However, the TRL and materials design stage of Ti₂AlC ceramic products cannot be raised without several properties other than oxidation resistance [1]. Mechanical strength is one of the most important properties of high-temperature heat-resistant components. Ti₂AlC ceramics exhibits a bending strength of 127–430 MPa [2-4] and a fracture toughness of 6.5–7.0 MPam^{1/2} [4-5]; these values are respectively comparable to or higher than those of commercial Al₂O₃, one of the typical ceramics [6]. The reported values are scattered (Table 1-1). When Ti₂AlC ceramics is used as a structural component, it is necessary to identify the cause of the mechanical strength variation and stabilize it. The bending strength of MAX phase ceramics increased when the grain size was reduced [5]. The mechanical strength of Ti₂AlC ceramics may vary with grain size. The reason for the variation in grain size may be due to the effect of dissimilar phases, as in the case of oxidation resistance. The chemical composition of Ti₂AlC may affect its oxidation behavior. Because Ti₂AlC is a line phase [7], commercial Ti₂AlC ceramic powder contains other phases such as TiC, Ti₃AlC₂ or TiAl₃ [8]. The minor phases, such as TiAl₃ significantly affect the oxidation resistance of Ti₂AlC. The other phases may affect grain size, mechanical strength, and

oxidation resistance. The ability to control mechanical strength by controlling dissimilar phases and grain size will raise stage in TRL and material design. In order to promote the social implementation of Ti_2AlC ceramics, it is necessary to use strengthening methods that general companies can implement. Texturing method is a commonly used strengthening method for MAX phase ceramics [9]. The bending strength and fracture toughness values of Ti_2AlC ceramics can be significantly improved by orienting the crystal grains in a certain direction. This strengthening method requires the use of a unique magnetic field generator and is not easily implemented by general companies. The mechanical strength strengthening by controlling dissimilar phases may be less expensive than other strengthening methods. Other methods of increasing mechanical strength are dispersion strengthening. The addition of Nb significantly affects oxidation resistance and may have a substantial effect on mechanical strength. There is a possibility of dispersion strengthening by Nb and other phases. However, there are few reports on the materials design with dispersing dissimilar phases and adding alloying elements for improving mechanical properties.

In this study, effects of varying the Al content and Nb addition on the mechanical strength of Ti_2AlC ceramics was investigated to establish a material design strategy. Additionally, influences of grain size on the mechanical strength of Ti_2AlC ceramics is discussed by comparing the samples with different milling processing.

3.2 Experimental

3.2.1 Materials

Commercial Ti, Al, and C powders were mixed in Ti:Al:C molar ratios of 2:1:0.9, 2:1.2:0.9, and 2:1.5:0.9, with the corresponding samples receiving the

designations A11 and A11.2, respectively. Some A11.2 samples had 5% of their Ti content replaced with Nb; these samples are referred to as A11.2Nb. The particle size and purity of the raw powders were as follows: 38 μm and 99.9% for Ti, 3 μm and 99.9% for Al, 1-2 μm for C and 45 μm for Nb (Kojundo Chemical Laboratory). The powder mixture was placed in an alumina container and treated in a vacuum at 1300°C for 16 h before being dry-milled using a mortar. The A11.2 powder was ground by ball milling. The ball mill was conducted with a zirconia pot of 430 ml capacity and three types of zirconia balls of 3, 6, and 10 mm in diameter. The medium for the ball mill was 150 ml ethanol, and 30 g of powder was added. The ball space filling ratio was one-third, the vessel rotation speed was constant at 220 rpm, and the processing time was 24 hours. The synthesized powder was consolidated for 15 min via a pulsed electric current sintering technique (LABOX-1550i75S, SinterLand Inc.) using a graphite die and punch at 1300°C in a vacuum under a 30 MPa uniaxial pressure. The density was measured via the Archimedes method with toluene as the immersion medium to confirm that the sintered sample had a relative density of over 99% of the theoretical value. Phase identification was conducted via X-ray diffraction (XRD, Rigaku Corporation MiniFlex 600) using monochromatic Cu $K\alpha$ radiation.

3.2.2 Mechanical tests

The fracture strength was evaluated via three-point bending tests with a span length of 16 mm. The bending tests were conducted in air at room temperature with a crosshead speed of 0.5 mm/min. The sintered samples were cut into 3 \times 4 \times 20 mm rectangular bar specimens. The specimens were ground with SiC abrasive papers of different grits (up to 3000 grit) and consequently polished with 3 and 1 μm diamond slurries until mirror-like surfaces with R_a values below 0.05 μm were achieved,

according to the JIS R 1601 standard. The edges of the specimens were beveled to 45° to prevent fractures due to edge cracks. In this paper, the specimens without machining cracks are referred to as polished specimens.

The fracture toughness of the Ti₂AlC ceramics was evaluated using the single edge notch beam (SENB) method. The sintered samples were cut into 6 × 4 × 20 mm rectangular bar specimens. A straight notch with a depth of 1.0 mm and tip radius of 0.125 mm was introduced into the bar specimens using a diamond saw, according to the JIS R 1607 standard. The fracture toughness (K_{IC}) was calculated using the peak stress of the bending test according to Bakker's equation [10]:

$$K_{IC} = F\sigma_b\sqrt{\pi a} = \sigma_b \frac{F_k(\alpha)^{\frac{3}{2}}}{(1-\alpha)^2} \sqrt{\pi a} \quad (3-1)$$

where σ_b is the maximum stress at failure, F is the geometric factor, a is the notch depth, W is the specimen height, α is a divided by W , and $F_k(\alpha)$ can be calculated using the values of α as per the following equation:

$$F_k(\alpha) = \frac{1.0731 - \alpha(1-\alpha) \left(1.1980 - 5.1240\alpha + 7.3327\alpha^{\frac{3}{2}} - 3.1403\alpha^2 \right)}{1 + 1.8706\alpha} \quad (3-2)$$

The initial microstructure and fractures surfaces of the Ti₂AlC ceramics were observed via scanning electron microscopy (SEM, ZEISS Gemini SEM) coupled with backscattered electron diffraction (EBSD) and energy dispersive X-ray spectrometry (EDX). Backscattered electron (BSE) images, elemental maps, inverse pole figure (IPF) maps, phase maps, and kernel average misorientation (KAM) maps were obtained. A

KAM value is the average of the crystallographic misorientation differences between a measurement point and its neighbors; areas with high KAM values are likely to have accumulated strain. Specimens for the initial microstructure and workpiece surface observation were obtained by cutting a bent specimen in half in the longitudinal direction using a refining saw, resin mounting it with the cut surface down, and buffing with a diamond slurry until a mirror-like surface was obtained. The grain size distribution was analyzed using the OIM-Analysis software to measure the crystal orientation and the lengths of the long and short sides of the crystal grains in the observation area ($400 \times 200 \mu\text{m}$).

3.3. Results

3.3.1 Initial microstructural features

Figure 3-1 shows the XRD patterns of the sintered samples in all the groups. The main peaks in these XRD patterns were identified as originating from Ti_2AlC . In the case of A11, peaks attributed to TiAl_3 and TiC were also observed. The patterns recorded for the remaining samples had minor peaks originating from TiAl_3 . Figure 3-2 shows SEM images of the hand milled and ball milled powder. The particle size of the ball milled powder was finer than that of the powder that was not ball milled.

Figure 3-3(a) shows an overall view of the EBSD analysis range of A11. Figure 3-3(b) shows the pole figure of the observed area; the points are dispersed, and not concentrated in one area. The A11 crystal planes were randomly distributed without a preferential orientation, although the A11 samples was sintered 30 MPa. Figure 3-3(c) shows the length distributions of the short and long sides of the Ti_2AlC crystals obtained via EBSD image analysis. The modes of the grain lengths were 3 and 6 μm for the long and short sides, respectively, and the longest grain had a long side of 42 μm .

Figure 3-3(d) shows the distribution of the aspect ratio of the grains. This is referred to as a_g/c_g , where a_g (grain size of the major axis) and c_g , (grain size of the minor axis) are the lengths of the long and short sides, respectively. The mode value of the aspect ratio was approximately 1.7, respectively, which indicates a power law distribution. Figure 3-4 shows EBSD analysis results of Al1.2. Figure 3-3(b) shows the pole figure of the observed area; the points are dispersed, and not concentrated in one area. The Al1.2 crystal planes were randomly distributed without a preferential orientation. Figure 3-4(c) shows the length distributions of the short and long sides of the Al1.2 crystals. The modes of the grain lengths were 24 and 6 μm for the long and short sides, respectively, and the longest grain had a long side of 78 μm . Figure 3-4(d) shows the distribution of the aspect ratio of the grains. The mode value of the aspect ratio was approximately 1.7, respectively, which indicates a power law distribution. Figure 3-5 (a) shows EBSD analysis results of Al1.2Nb. Figure 3-5(b) shows the pole figure of the observed area; the points are dispersed, and not concentrated in one area. The Al1.2Nb crystal planes were randomly distributed without a preferential orientation. Figure 3-5(c) shows the length distributions of the short and long sides of the Ti_2AlC crystals. The modes of the grain lengths were 24 and 3 μm for the long and short sides, respectively, and the longest grain had a long side of 42 μm . Figure 3-5(d) shows the distribution of the aspect ratio of the grains. The mode value of the aspect ratio was approximately 1.7, respectively, which indicates a power law distribution. Figure 3-6 (a) shows EBSD analysis results of ball milled Al1.2. Figure 3-6(b) shows the pole figure of the observed area; the points are dispersed, and not concentrated in one area. The ball milled Al1.2 crystal planes were randomly distributed without a preferential orientation. Figure 3-6(c) shows the length distributions of the short and long sides of the Ti_2AlC crystals

obtained. The modes of the grain lengths were 1 and 0.5 μm for the long and short sides, respectively, and the longest grain had a long side of 21 μm . Figure 3-6(d) shows the distribution of the aspect ratio of the grains. The mode value of the aspect ratio was approximately 1.7, respectively, which indicates a power law distribution.

3.3.2 Fracture strength and behavior

As shown in Figure 7(a), ball milled A11.2 and A11 had higher bending strength than A112 and A112Nb. The bending strengths for ball milled A11.2, A11, A112 and A112Nb specimens were 643 ± 114 , 504 ± 25 MPa, 376 ± 19 MPa and 331 ± 5 MPa respectively. The values of K_{IC} of the ball milled A11.2, A11, A11.2 and A11.2Nb specimens evaluated via the SENB method are equal to 6.6, 6.6, 6.9 and 6.8 $\text{MPa}\cdot\text{m}^{1/2}$. These are respectively at least 1.5 times higher than alumina ceramics [6]. In particular the value of ball milled A11.2 is comparable with zirconia ceramics and silicon nitride ceramics. SEM images of the fracture surface of the machined specimen with the lowest strength show that fracture initiation sites attributed to cutting-induced cracks were not observed (Figures 3-4). Numerous cracks related to kink deformation were observed around the fracture initiation sites.

3.4. Discussion

3.4.1 Microstructural features of Ti_2AlC ceramics

The grain size of ball milled A11.2 was smaller than other samples. This grain size reduction is caused by the effect of ball milling on the fineness of the sintered powder. The grain size of A11 (3 μm) was smaller than that of A11.2 (24 μm) and A11.2Nb (24 μm). This difference in grain size may be a pinning effect caused by the influence of different phases [11]. Dispersion of second-phase particles in the

polycrystalline structure suppresses grain growth by pinning grain boundaries. The precipitation of a different phase, such as TiC pinned grain growth of Al1. The small amount of heterophase in the sintered Ti₂AlC matrix inhibits grain growth, and some Ti₂AlC grains are pinned at the grain boundary. Further grain size coarsening can be prevented by increasing the amount of TiC. The addition of Nb did not cause significant changes in grain shape or mechanical strength because the crystal structure had not changed then Nb was replaced by Ti. The values of K_{IC} of Ti₂AlC ceramics are higher than that of Al₂O₃[6]. This improvement is caused by the layered structure with randomly distributed unoriented grains of the Ti₂AlC ceramic, which causes pseudo-plastic deformation by kink formation and plastic deformation [12]. Ball milled Al1.2 had higher fracture toughness values than the other samples. Because it has a layered structure and short grain length that may act as a fracture origin, suppressing initial crack initiation until higher stress concentrations than the other samples. The fracture toughness values of Al1 with TiC dispersion were almost the same for Al1.2 and Al1.2Nb. The pinning effect can increase the fracture toughness and bending strength of ceramics [13-14]. However, there are problems with TiC pinning on ceramic materials. In the case of dispersion strengthening with oxides, the crack-suppressing effect of the dispersed particles works effectively, whereas, in the case of dispersion strengthening with TiC, the cracks propagate through the TiC particles and the crack-suppressing effect of TiC does not work effectively [14]. The increased fracture toughness caused by TiC dispersion is not a crack-pinning effect of the dispersed particles but a grain atomization effect [14]. The fracture toughness values of Al1 did not significantly increase because the crack growth arresting effect of the dispersed TiC was weak and the layered structure characteristic of the MAX phase had a more dominant effect.

There were no significant difference in the fracture toughness values of Nb doped sample. This is caused by the layered structure of Ti₂AlC ceramics did not change even with changes in composition caused by Nb addition.

3.4.2 Fracture mechanics analysis

The effects of the grain sizes in bulk samples on the bending strength were evaluated. The relationship between mechanical strength and grain size of ceramic materials is generally studied based on Hall–Petch relation, as follows:

$$\sigma_y = \sigma_0 + kd^{-\frac{1}{2}} \quad (3-3)$$

where σ_y is the yield strength, d is the grain size, σ_0 is the internal strength, and k is the constant [15].

Figure 3-10 shows the relationship between mechanical strength and grain size. A Hall-Petch relationship between bending strength and grain size of Ti₂AlC ceramics is established. The bending strength of Ti₂AlC ceramics can be improved by reducing the grain size. The relationship between grain size and initial defects is important when ceramic materials exhibit a Hall-Petch relationship. The bending strength of Al₂O₃ which is one of typical ceramic shows a Hall-Petch relationship [16-18]. The Hall-Petch relationship of Al₂O₃ is not influenced by the grain size itself but by the initial defect size, which is proportional to the grain size [18]. Similar to Al₂O₃, the bending strength of Ti₂AlC ceramics increases with decreasing grain size because the long grains are the initial defects. Figure 3-10 shows the relationship between grain size and fracture toughness values. There was no strong correlation between grain size and fracture

toughness values. As discussed in section 3.4.1, the unique layered structure of MAX phase ceramics has a more significant influence on the fracture toughness values of Ti_2AlC ceramics than grain size. The mechanical properties of Ti_2AlC ceramics are expected to be further improved by reducing the grain size while maintaining the microstructure unique to MAX phase ceramics.

3.5 Conclusions

The influence of ball mill and minor phase on the mechanical strength of Ti_2AlC ceramics was investigated via microstructural observation and fracture mechanics. The crystal planes of the as-sintered Ti_2AlC ceramics were found to be randomly distributed without preferential orientation. The grain size of ball milled A11.2 was smaller than other samples. This is due to the effect of ball milling on the fineness of the sintered powder. The grain size of A11 is smaller than A11.2 and A11.2Nb. This is thought to be due to the pinning effect of the precipitation of different phases such as TiC, which inhibited grain growth. The addition of Nb did not change the bending strength or fracture toughness values. This is because Nb only replaced Ti and did not change the crystal structure. The bending strengths for ball milled A1.2, A11, A11.2 and A11.2Nb specimens were 643 ± 114 , 504 ± 25 MPa, 376 ± 19 MPa and 331 ± 5 MPa respectively. A11 and ball milled A11.2 had higher bending strength than A11.2 and A11.2Nb. A Hall-Petch relationship between bending strength and grain size of Ti_2AlC ceramics is established. The mechanical properties of Ti_2AlC ceramics are expected to be further improved by reducing the grain size while maintaining the microstructure unique to MAX phase ceramics.

References

- [1] M. Héder, From NASA to EU: the evolution of the TRL scale in public sector innovation, *The Innovation Journal: The Public Sector Innovation Journal*, 22:3 (2017) 1-23.
- [2] M.W. Barsoum, M. Radovic, Elastic and mechanical properties of the MAX phases, *Annu. Rev. Mater. Res.* 41 (2011) 195–227.
- [3] L. Cai, Z. Huang, W. Hu, S. Hao, H. Zhai, Y. Zhou, Fabrication, mechanical properties, and tribological behaviors of Ti_2AlC and $Ti_2AlSn_{0.2}C$ solid solutions, *J. Adv. Ceram.* 6 (2017) 90–99.
- [4] P. Wang, B.-C. Mei, X.-L. Hong, W.B. Zhou, Synthesis of Ti_2AlC by hot pressing and its mechanical and electrical properties, *Trans. Nonferr. Met. Soc.* 17 (2007) 1001–1004.
- [5] M.W. Barsoum, MAX phases: properties of machinable ternary carbides and nitrides, Wiley-VCH, Weinheim, 2013.
- [6] G.A. Gogotsi, Fracture toughness of ceramics and ceramic composites, *Ceram. Int.* 29 (2003) 777–784.
- [7] V. Witusiewicz, B. Hallstedt, A. Bondar, et al., Thermodynamic description of the Al-C-Ti system. *J. Alloys Compd.* 623 (2015) 480-496.
- [8] S. Badie, A. Dash, Y. Sohn, et al., Synthesis, sintering, and effect of surface roughness on oxidation of submicron Ti_2AlC ceramics. *J. Am. Ceram. Soc.* 104:4 (2021) 1669-1688.
- [9] X. Li, X. Xie, J. Gonzalez-Julian, J. Malzbender, R. Yang, Mechanical and oxidation behavior of textured Ti_2AlC and Ti_3AlC_2 MAX phase materials, *J Eur Ceram Soc.* 40 (2020) 5258–5271.

- [10] A.D. Bakker, Evaluation of elastic fracture mechanics parameters for bend specimens, *Int. J. Fract.* 71 (1995) 323–343.
- [11] T. Masayuki, M. Hideki, M. Yoshihiro, M. Tetsushi, Inhibition Effect of Ti(C,N) Particle Dispersion on Grain Growth of WC-Co Cemented Carbide, *Mater. Trans.* 60:5 (2019) 785-792.
- [12] M.W. Barsoum, MAX phases: properties of machinable ternary carbides and nitrides, Wiley-VCH, Weinheim, 2013.
- [13] H. Awaji, S. Choi, T. Ebisudani, D. Jayaseelan, Toughening Mechanisms of Structural Ceramics, *JCS-Japan.* 108:6 (2000) 611-613.
- [14] Y. Ozaki, Bulk and Surface Modifications of Ceramics, *J-JSMS.* 40:457 (1991) 1253-1263.
- [15] S.N. Naik, S.M. Walley, The Hall–Petch and inverse Hall–Petch relations and the hardness of nanocrystalline metals, *J Mater Sci.* 55 (2020) 2661–2681.
- [16] F. F. Lange, Transformation toughening Part 4 Fabrication, fracture toughness and strength of Al₂O₃-ZrO₂ composites, *J. Mater. Sci.* 17 (1982) 247-254.
- [17] D. Casellas, M.M. Nagl, L. Llanes, M. Anglada, Fracture toughness of alumina and ZTA ceramics: microstructural coarsening effects, *J Mater Process Technol.* 143-144 (2003) 148-152.
- [18] N. Miyahara, K. Yamaishi, Y. Mutoh, K. Uematsu, M Inoue, Effect of grain size on strength and fracture toughness in alumina, *Transactions of the Japan Society of Mechanical Engineers Series A.* 58:556 (1992) 67-74.

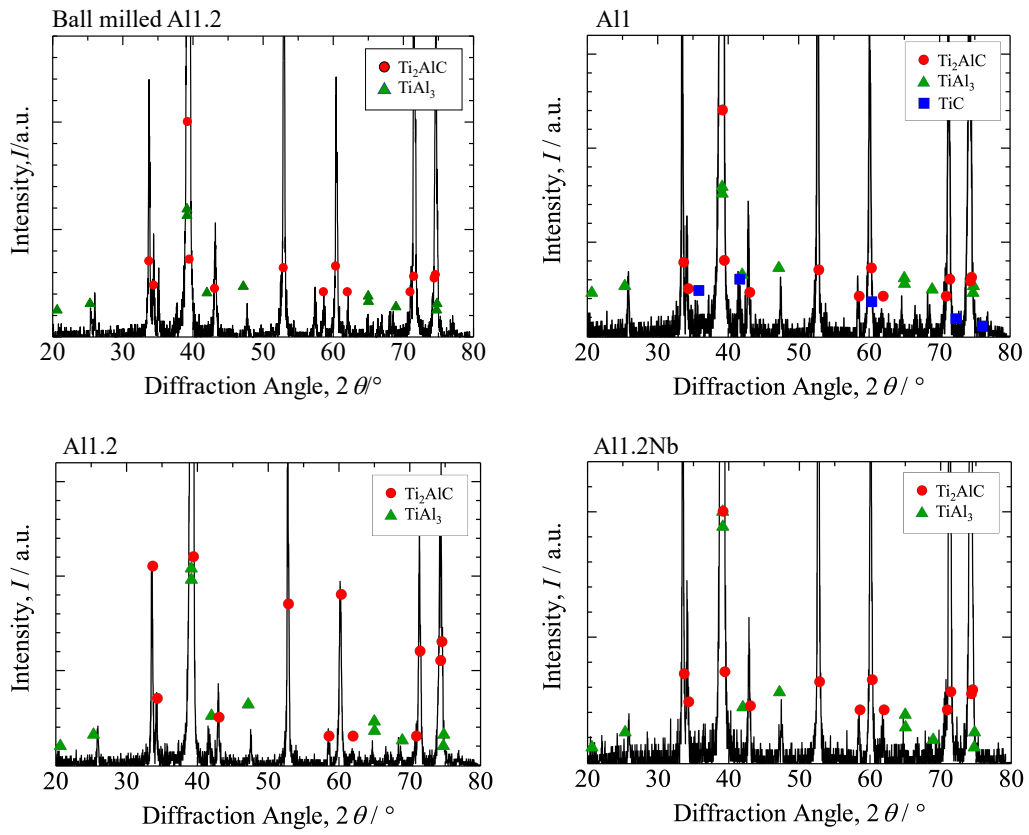


Figure 3-1 X-ray diffraction patterns on the bulk samples: ball milled A11.2, A11, A11.2 and A11.2Nb.

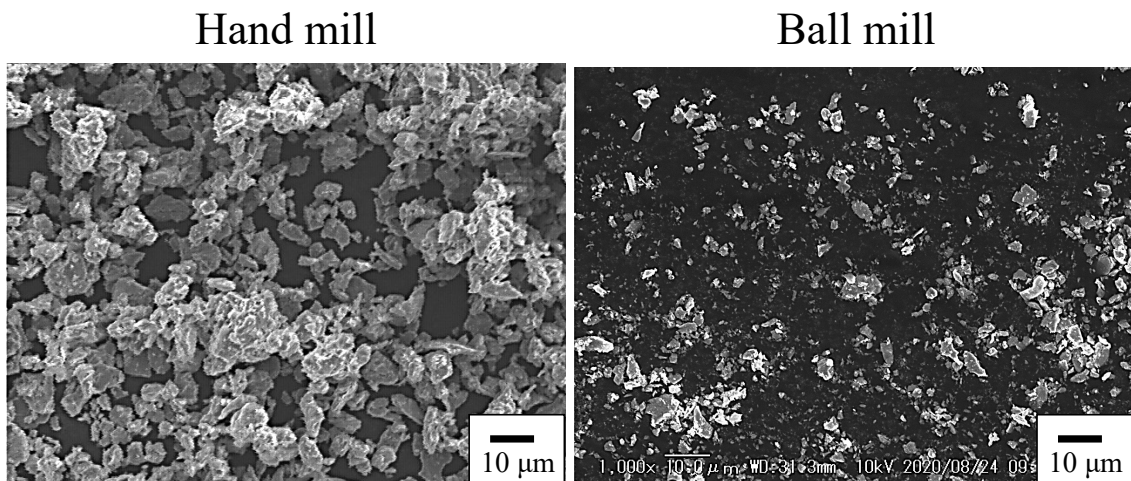


Figure 3-2 SEM images of the hand milled powder and ball milled one.

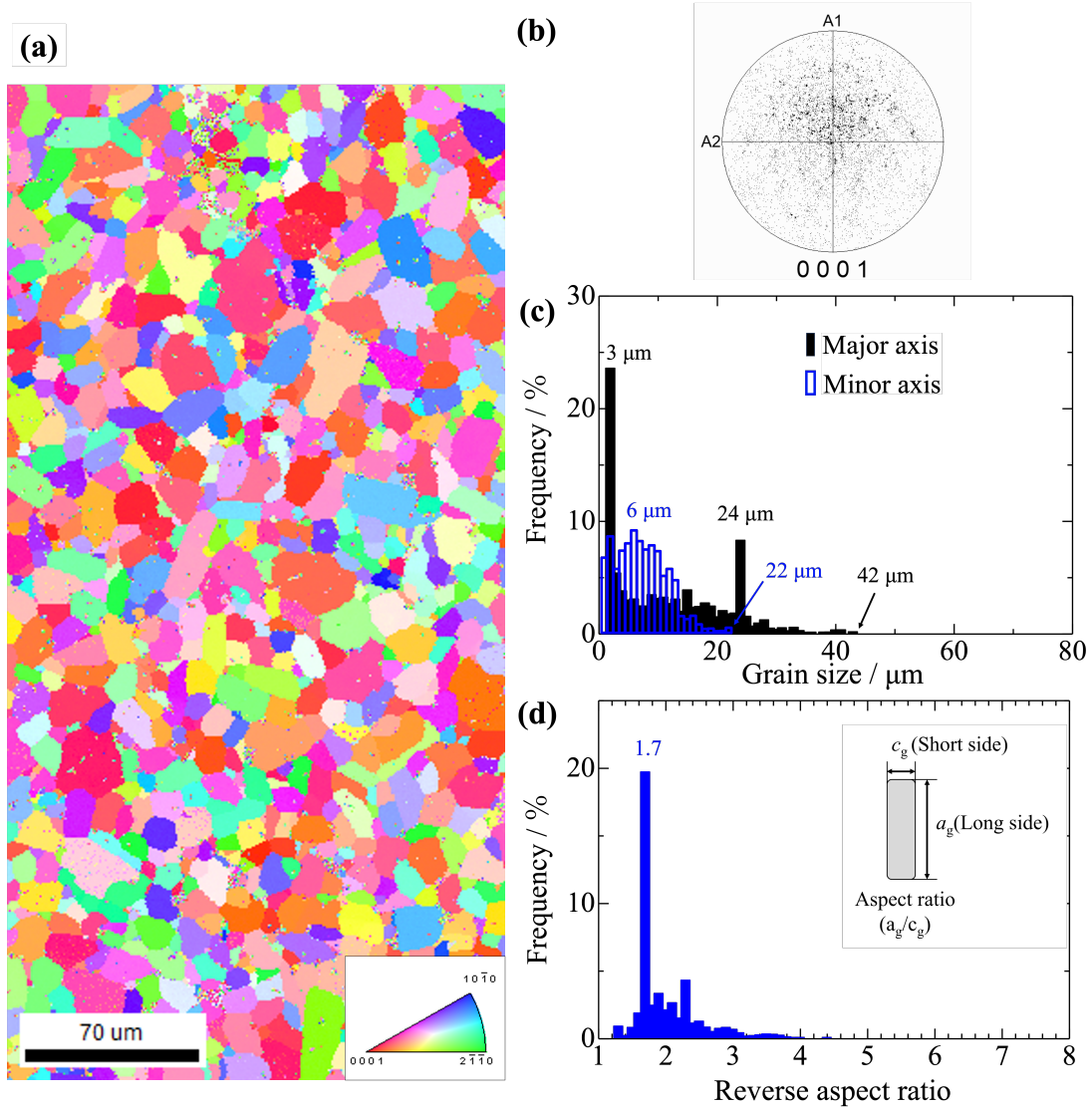


Figure 3-3 Grain analysis of Al1 via scanning electron microscopy and backscattered electron diffraction. (a) Inverse pole figure map of the observed section; (b) pole figure of the observed section; (c) grain size distributions along the major and minor axis; (d) aspect ratio distribution (c_g/a_g).

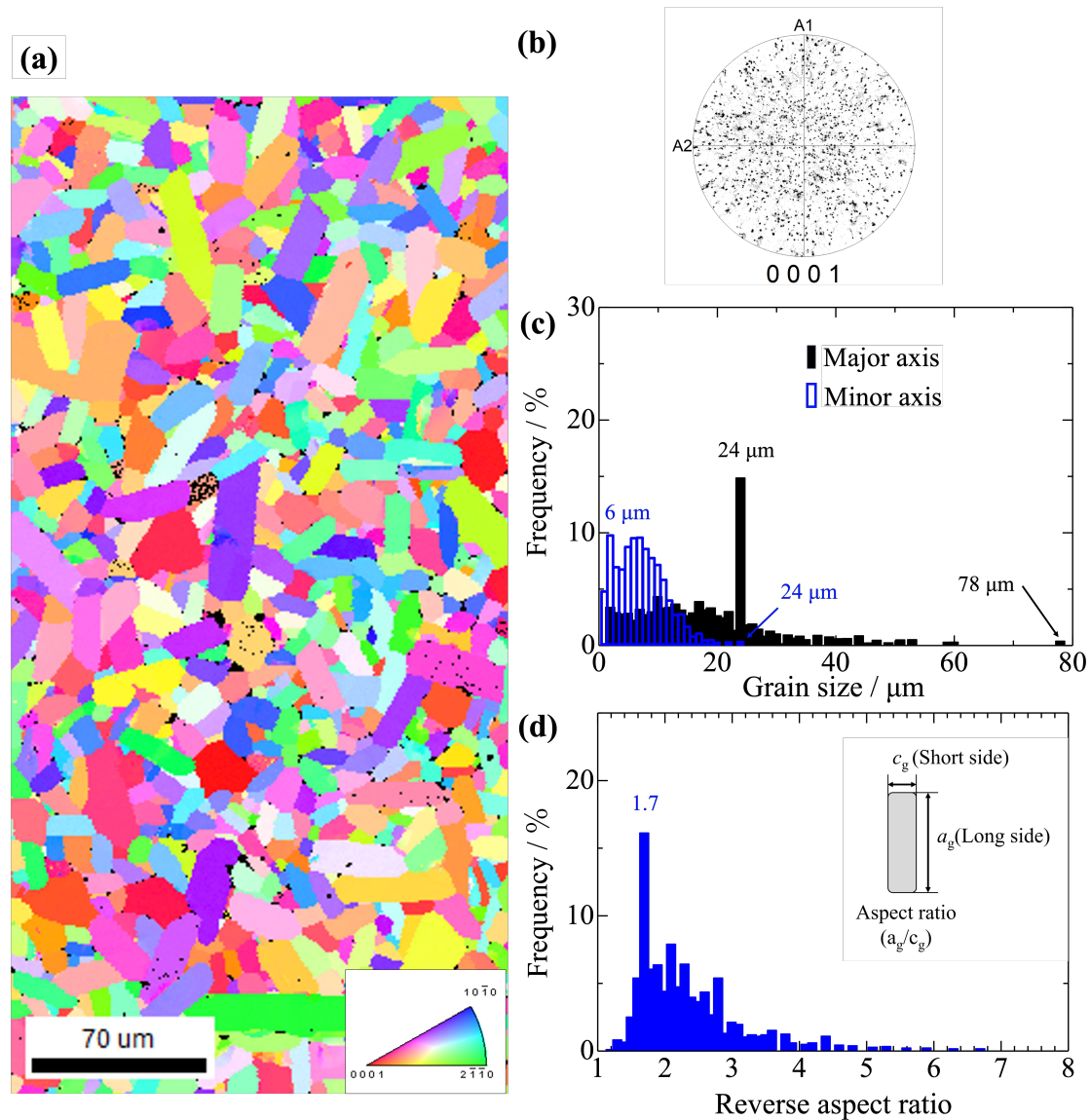


Figure 3-4 Grain analysis of Al1.2 via scanning electron microscopy and backscattered electron diffraction. (a) Inverse pole figure map of the observed section; (b) pole figure of the observed section; (c) grain size distributions along the major and minor axis; (d) aspect ratio distribution (c_g/a_g).

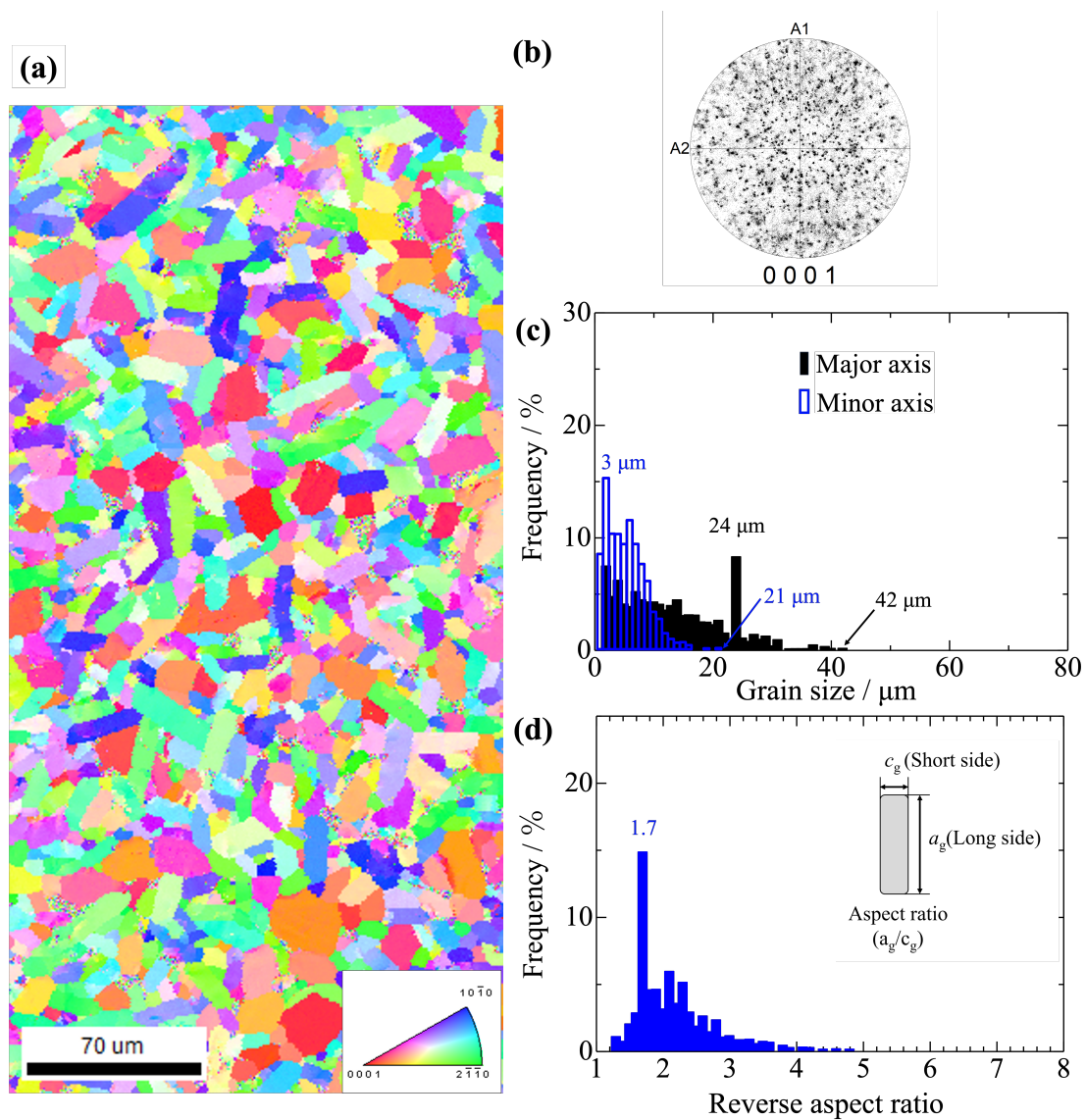


Figure 3-5 Grain analysis of Al_{1.2}Nb via scanning electron microscopy and backscattered electron diffraction. (a) Inverse pole figure map of the observed section; (b) pole figure of the observed section; (c) grain size distributions along the major and minor axis; (d) aspect ratio distribution (c_g/a_g).

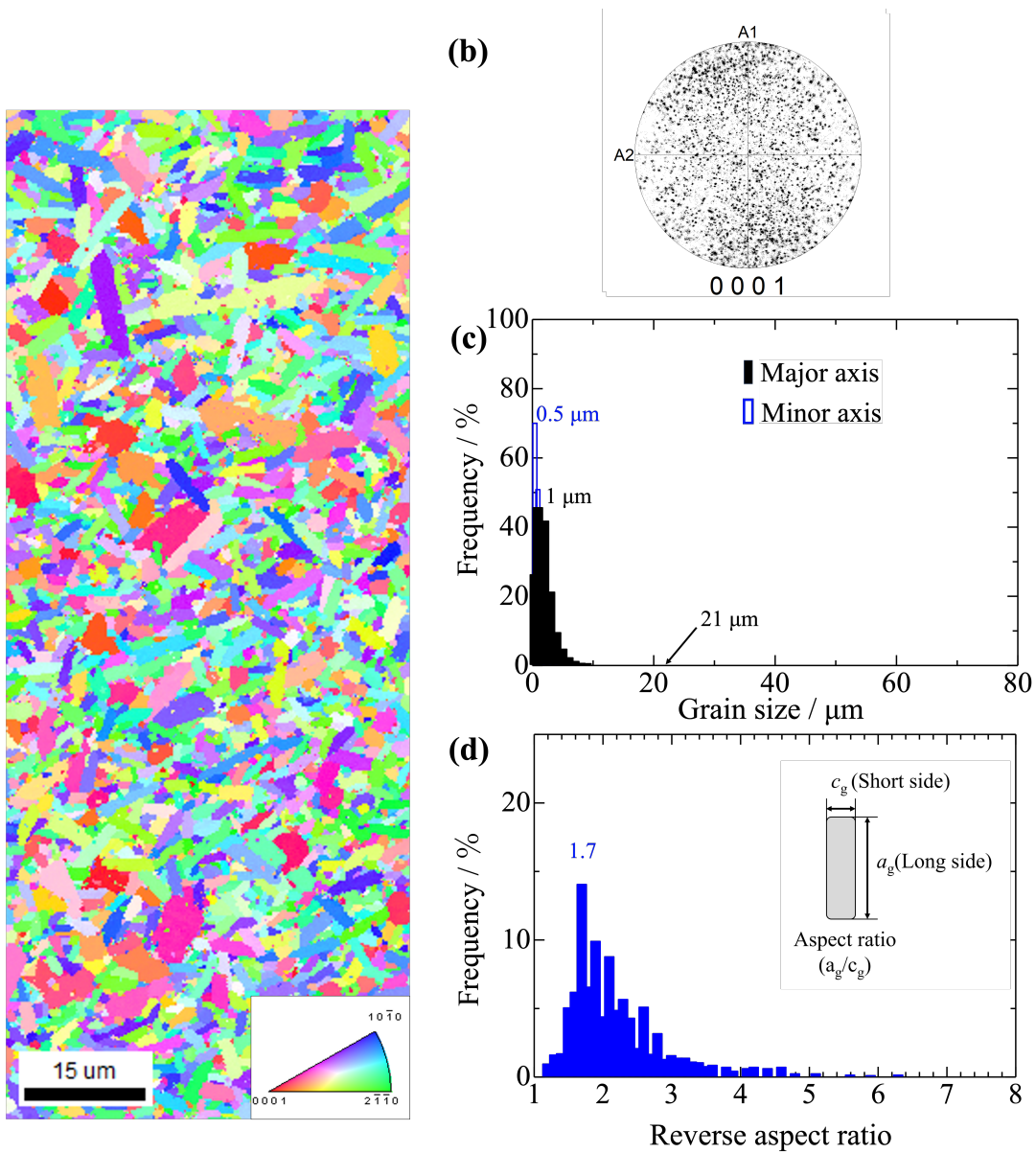


Figure 3-6 Grain analysis of ball milled Al_{1.2} via scanning electron microscopy and backscattered electron diffraction. (a) Inverse pole figure map of the observed section; (b) pole figure of the observed section; (c) grain size distributions along the major and minor axis; (d) aspect ratio distribution (c_g/a_g).

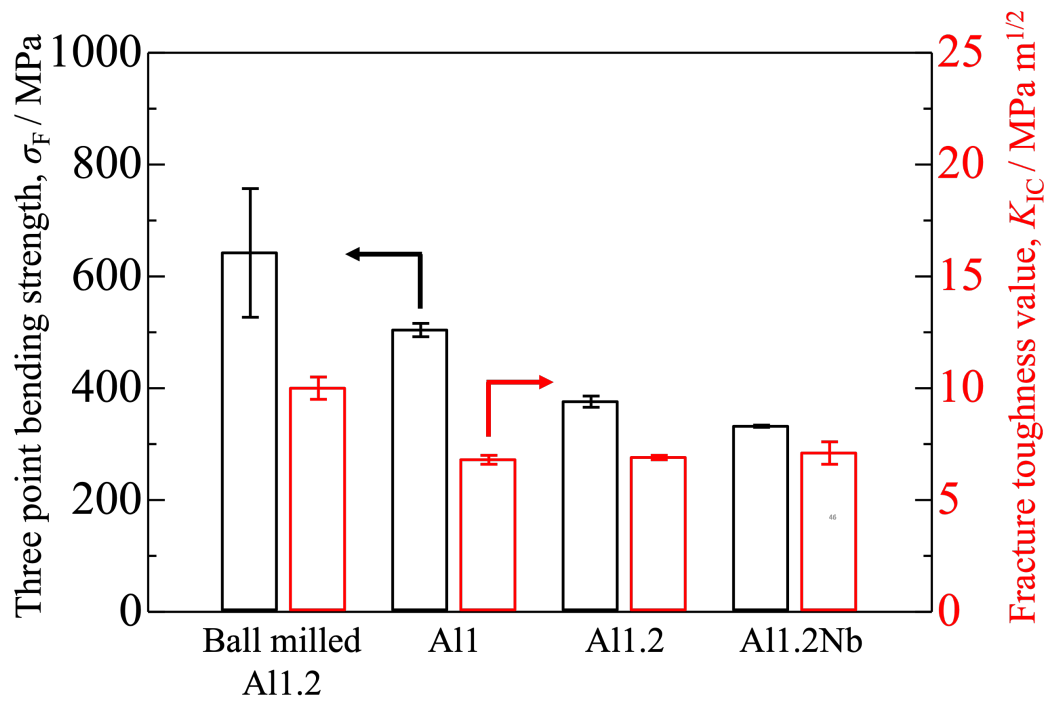


Figure 3-7 Bending strength and fracture toughness value of ball milled Al1.2, Al1, Al1.2 and Al1.2Nb; the error bars represent standard deviation values.

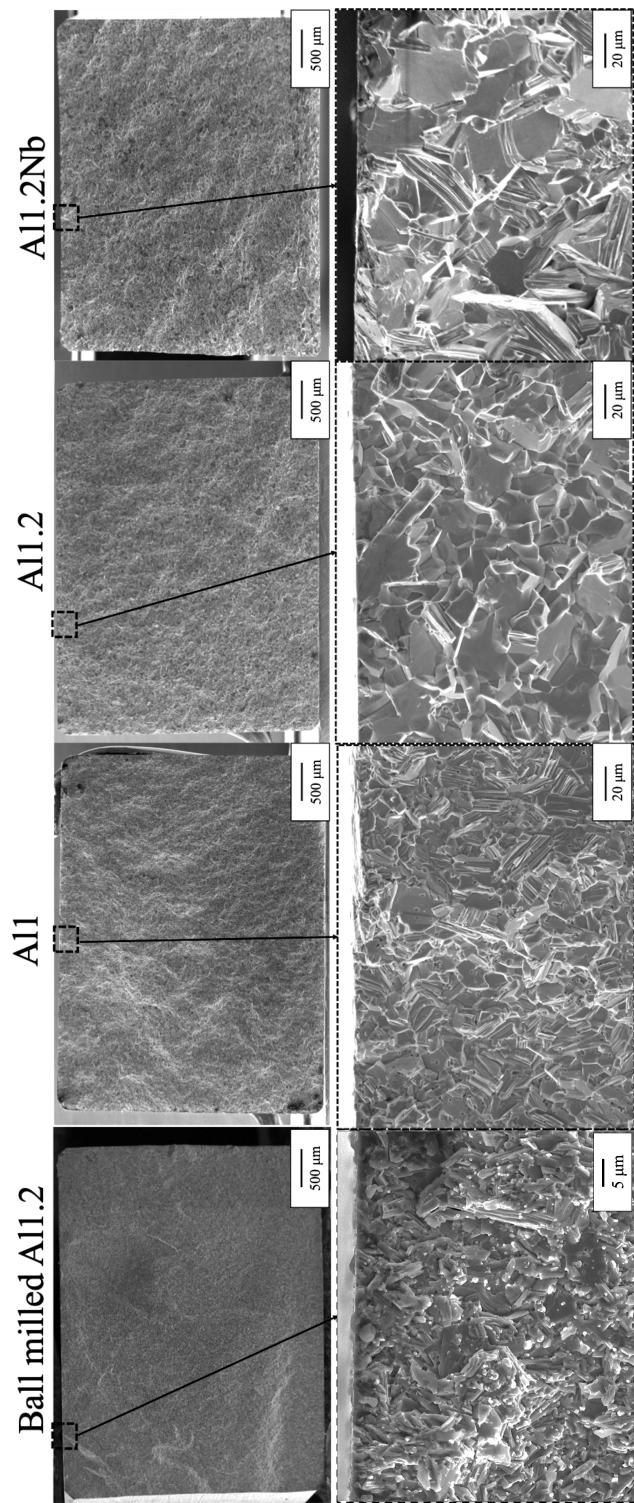


Figure 3-8 SEM image of the fracture surface of ball milled Al1.2, Al1, Al1.2 and Al1.2Nb and fracture surface around the fracture origin.

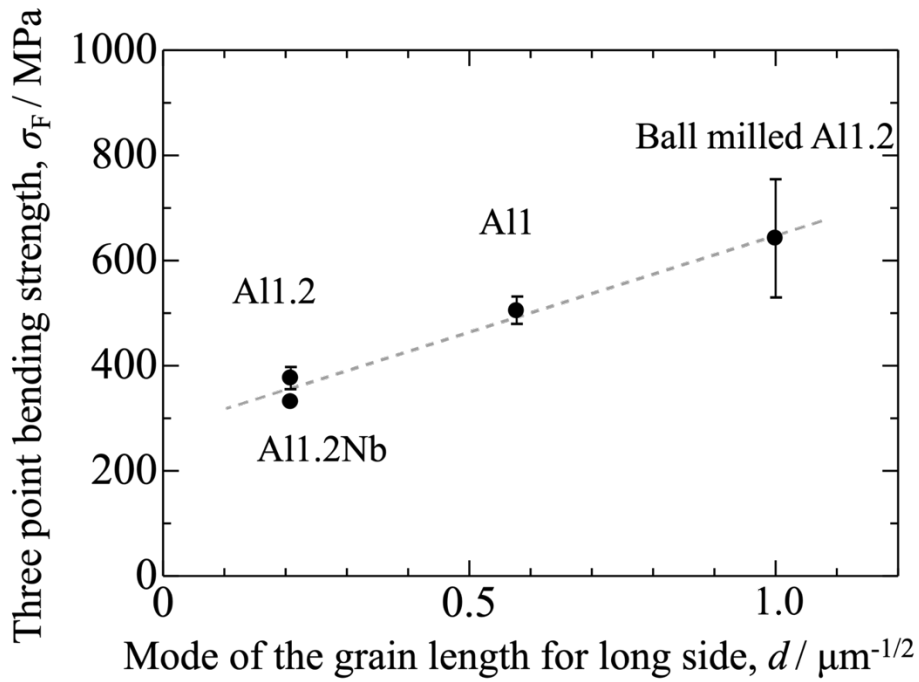


Figure 3-9 Bending strength versus grain length for Ti_2AlC ceramics.

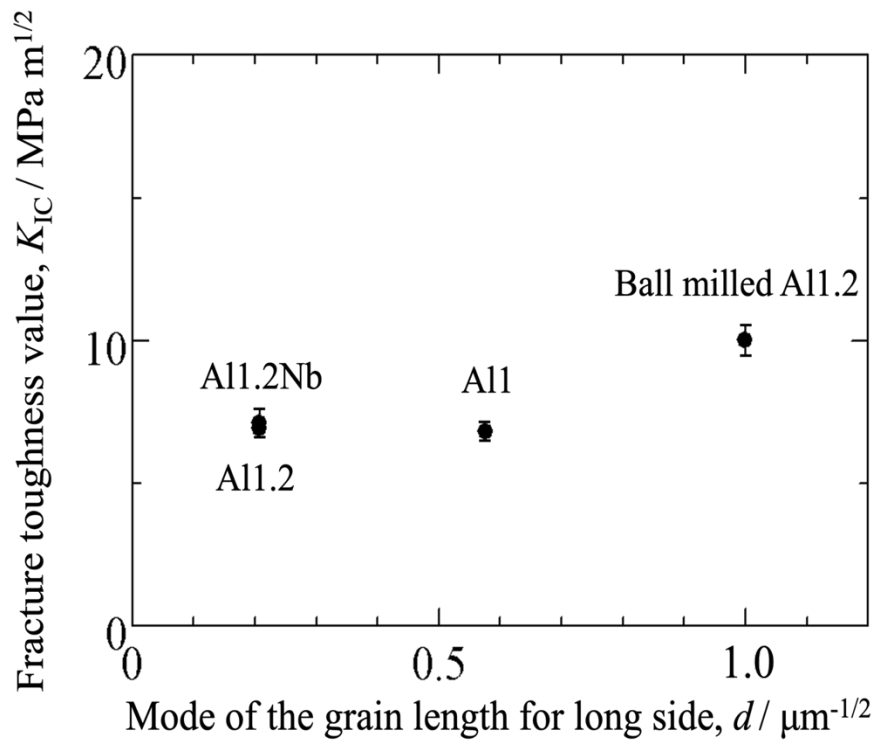


Figure 3-10 Fracture toughness versus grain length for Ti_2AlC ceramics.

Chapter 4: Influences of the cutting damage on Ti_2AlC ceramics

4.1 Introduction

The manufacture of structural ceramic components incurs high machining costs that limit the application of these materials [1]. The hard and brittle nature of ceramic materials makes the cutting of complex shapes very difficult. The mechanical damage introduced during cutting significantly reduces the mechanical strength and reliability of ceramic materials [2,3], necessitating the use of expensive diamond cutting tools [4]. Other issues include severe wear, extremely short tool life, and the need for highly rigid cutting machines [5]. Ceramics are typically machined by grinding with diamond wheels rather than cutting [6]; however, the fabrication of pieces with complex shapes by grinding is difficult and time-consuming. Cutting damage is introduced to the cutting surface of the ceramic material without exception. The resulting subsurface damage must be removed by a costly finishing process, i.e., grinding or lapping, to ensure the strength and reliability of the ceramic components. The development of machinable ceramics which do not require the finishing process and the understanding of the cutting damage mechanism are the key to improving the performance/cost of ceramic parts [1].

MAX phase ceramics are layered ternary compounds with the general formula $\text{M}_{n+1}\text{AX}_n$, where M is a transition metal, A is an A-group element, and X is C or N. These materials exhibit good machinability [7] and are expected to overcome the cutting limitations of ceramics [7–10]. MAX phase ceramics are unique materials with both metallic and ceramic properties owing to the existence of M-A metallic bonds and M-X

covalent bonds within a single crystal [11]. The microstructure of these ceramics consists of a mille-feuille-like layered structure with high toughness and a lower susceptibility to work damage than that of typical ceramics [12]. In addition to their superior high-temperature oxidation resistance, low density, and hardness [7,13–16], their crystal structural characteristics give MAX phase ceramics an electrical conductivity, thermal conductivity, and thermal shock resistance comparable to those of metallic materials. The properties of MAX phase ceramics are influenced through the proportions of the M, A, and X elements in their structure; thus, these ceramics are expected to constitute next-generation structural materials [7]. Ti_2AlC is a MAX phase ceramic with great potential as a high-temperature heat resistant material owing to its excellent oxidation resistance [17,18] and self-crack-healing ability [15,16]. Ti_2AlC exhibits a bending strength of 275–430 MPa [12,19,20] and a fracture toughness of 6.5–7.0 $\text{MPam}^{1/2}$ [7,20]; these values are respectively comparable to and higher than those of Al_2O_3 , a typical commercial ceramic [21]. Furthermore, Ti-Al-C MAX phase ceramics are expected to further improve mechanical strength and oxidation resistance through composition optimization using machine learning [22–24]. The self-crack-healing abilities of Ti_2AlC ceramics exhibit are achieved by filling and bonding surface cracks with the Al_2O_3 formed in a high-temperature oxidizing atmosphere [15,16]. These properties improve the reliability of Ti_2AlC machined parts, while any remaining cutting-induced cracks can be repaired by heat treatment [25]. Ti_2AlC ceramics are expected to be useful in high-temperature applications and the fabrication of ceramic components with complex shapes.

Although the machining of MAX phase ceramics has been reported [7–10], the damage mechanism of the cutting surface and the influence of the cutting damage on

mechanical strength from the viewpoint of fracture mechanics has not been elucidated. Despite its good machinability, cutting damage can be introduced to the cutting surface of Ti_2AlC . In particular, microcracks on the surface can reduce the mechanical strength of these ceramics [2,3]. Electrical discharge machining (EDM) of Ti_3SiC_2 MAX phase ceramics is known to reduce their bending strength by 25% owing to EDM-related subsurface damage [9]. A systematic evaluation of the effect of cutting damage on mechanical strength is necessary for the application of Ti_2AlC ceramic products.

In this study, cutting tests were performed using a commercial cemented carbide end mill under severe conditions corresponding tool steels on Ti_2AlC ceramics and other materials for comparison. The subsurface damage was evaluated by measuring the surface roughness and microstructural observations of the cut surfaces. Bending tests were also conducted on the machined Ti_2AlC ceramic samples. Additionally, the influence of cutting damage on the mechanical strength of the Ti_2AlC ceramics is discussed in terms of nonlinear fracture mechanics.

4.2 Experimental

4.2.1 Materials

Commercial Ti (Kojundo Chemical Laboratory Co., Ltd.), Al (Kojundo Chemical Laboratory Co., Ltd.), and C (Aldrich Chemical Company), powders were mixed in a Ti:Al:C molar ratio of 1:1:2. The particle sizes of the Ti, Al, and C powders were 38 μm , 3 μm , and 1–2 μm , respectively, and the purity of each of the three powders was 99.9%. The powder mixture was treated in a vacuum at 1300 $^{\circ}C$ for 16 h in an alumina container before being dry-milled using a mortar. The obtained powder was consolidated for 15 min via a pulsed electric current sintering technique (LABOX-

1550i75S, SinterLand Inc.) using a graphite die and punch at 1300°C in a vacuum under 30 MPa uniaxial pressure. The density was measured via the Archimedes method using toluene as the immersion medium to confirm the relative density and porosity of the sintered sample. Nearly fully densified Ti₂AlC ceramics with a porosity of less than 0.5% were used to suppress the effects of density and porosity on mechanical properties. Phase identification was conducted via X-ray diffraction (XRD, Rigaku Corporation MiniFlex 600) using monochromatic Cu K α radiation.

4.2.2 Machining conditions

Cutting tests were conducted under the same conditions on graphite (High-strength graphite punch, Tanaka Co., Ltd.), a machinable brittle material [26], and heat-treated tool steel (JIS-SKD61, Fe-0.35C-5Cr-1.5Mo-1V-1Si-0.35Mn) with a Vickers hardness (4.5 GPa) similar to that of Ti₂AlC (5.5 GPa) [27]. Ten cutting tests were conducted on the Ti₂AlC using the same end mill.

Cutting tests were performed on a sample surface with a 15 mm diameter using a commercially available cemented carbide end mill mounted on a plane milling machine using a six-flute square end mill for hardened steel (UMHHDH645, NS TOOL CO.) with a diameter, cutting edge, and overall length of 6 mm, 12 mm, and 60 mm, respectively. The cutting tool used cemented carbide tools that are generally used for cutting JIS-SKD61 in the actual manufacturing process. The cutting feed was maintained at a constant speed in one direction, up to a constant depth. Dry cutting was performed with a spindle speed, cutting speed, feed rate, and cut depth of 1500 rpm, 28.3 m/min, 100 mm/min, and 100 μ m. The cutting condition was based on the recommended cutting conditions of the end-mill supplier.

The surface roughness of each sample was measured in triplicate using a surface texture measuring instrument (Mitutoyo Form Tracer SV-C3100) using a standard stylus with a tip radius of 2 μm . The measurement was performed at the center of the cutting trace in the same direction as the cutting, under the conditions described in the JIS B 0651 and JIS B 0633 standards. For the cut surface, the cutoff value was 0.25 mm, the maximum sampling interval was 0.5 mm, and the evaluation length of the roughness curve was 4 mm because the arithmetic mean roughness (R_a) was in the range of 0.02 μm to 0.1 μm . The R_a of the polished surface was in the same range; thus, the cutoff value was 0.8 mm, the maximum sampling interval was 0.5 mm, and the evaluation length of the roughness curve was 1.25 mm. The evaluation lengths of the roughness curves of the cut and polished surfaces (4000 and 1250 μm , respectively) were sufficiently long considering the crystal structure and subsurface damage. The surface roughness was evaluated in terms of R_a , the ten-point average roughness (R_z), and the skewness (R_{sk}), from which the symmetry of the peaks and valleys of the roughness profile can be determined with respect to the mean line [28]. R_{sk} is given by equation (4-1):

$$R_{sk} = \frac{1}{NR_q^3} \left(\sum_{i=1}^N Y_i^3 \right) \quad (4-1)$$

where R_q is the root mean square roughness parameter and Y_i is the height of the profile at point i . A symmetrical height distribution, that is, a profile with as many peaks as valleys, has a skewness of zero. Profiles with removed peaks or deep scratches have negative skewness, while those with filled-in valleys or high peaks have positive skewness [28]. The cutting mode influences the value of R_{sk} , which tends to be negative

when cutting in brittle mode owing to a crack generation. Cutting in ductile mode has a lower cracking tendency than cutting in brittle mode [28,29]; thus R_{sk} is likely to have less negative value when cutting in ductile mode[28–31].

4.2.3 Mechanical tests

The fracture strength was evaluated via three-point bending tests with a span length of 16 mm. The bending tests were conducted in air at room temperature with a crosshead speed of 0.5 mm/min. Three bending tests were conducted for each specimen condition. The sintered samples were cut into rectangular specimens with dimensions of $3 \times 4 \times 20$ mm, which were ground with SiC abrasive papers of various grits (up to 3000 grit) and subsequently polished with 3 and 1 μm diamond slurries in accordance with the JIS R 1601 standard until mirror-like surfaces with R_a values below 0.05 μm were achieved. The edges of the specimens were beveled to 45° to prevent fractures resulting from edge cracks. Specimens without machining cracks are hereinafter referred to as polished specimens. The machined specimens were prepared using the end mill cutting conditions described in section 4.2.2. The cutting direction was parallel to the long sides of the specimens to ensure that large cutting cracks were introduced perpendicular to the tensile direction of the bending tests.

The fracture toughness of the Ti_2AlC ceramics was evaluated using the single edge notch beam (SENB) method. The specimen geometry was selected such that the fracture toughness values could be calculated by the evaluation equation. The sintered samples were cut into rectangular bar specimens measuring $6 \times 4 \times 20$ mm. A straight notch with a depth of 1.0 mm and tip radius of 0.125 mm was introduced into the bar specimens using a diamond saw in accordance with the JIS R 1607 standard. The

fracture toughness (K_{IC}) was calculated from the peak stress measured by the bending test according to Bakker's equation [32]:

$$K_{IC} = F\sigma_b\sqrt{\pi a} = \sigma_b \frac{F_k(\alpha)}{(1-\alpha)^2} \sqrt{\pi a} \quad (4-2),$$

where σ_b is the maximum stress at failure, F is the geometric factor, a is the notch depth, W is the specimen height, and α is a divided by W . $F_k(\alpha)$ can be calculated from the values of α according to equation (4-3):

$$F_k(\alpha) = \frac{1.0731 - \alpha(1-\alpha) \left(1.1980 - 5.1240\alpha + 7.3327\alpha^2 - 3.1403\alpha^3 \right)}{1 + 1.8706\alpha} \quad (4-3)$$

The initial microstructure and fractures surfaces of the Ti_2AlC ceramics were observed via scanning electron microscopy (SEM, ZEISS Gemini SEM) coupled with electron backscatter diffraction (EBSD) and energy dispersive X-ray spectroscopy (EDX). Backscattered electron (BSE) images, elemental maps, inverse pole figure (IPF) maps, phase maps, and kernel average misorientation (KAM) maps were obtained. KAM is defined as the average of the crystallographic misorientation differences between a measurement point and its neighbors; areas with high KAM values are likely to have accumulated strain. Observations of the initial microstructure and workpiece surface were made using samples obtained by cutting a bent specimen in half in the longitudinal direction using a refining saw. The cut specimen was then resin mounted with the cut surface facing down and buffed with a diamond slurry until a mirror-like surface was obtained. The grain size distribution was analyzed using OIM-Analysis software to

measure the crystal orientation and the lengths of the long and short sides of the crystal grains in the observation area ($450 \times 200 \mu\text{m}$).

4.3 Results

4.3.1 Initial microstructural features

The main peaks in the XRD pattern of the as-sintered Ti_2AlC ceramic correspond to Ti_2AlC (Figure 4-1(a-b)), with minor peaks corresponding to TiAl_3 also being observed. Figures 4-1(c-f) show EBSD and EDX patterns of the Ti_2AlC ceramic surface. These data confirm that the main structure consisted of a Ti_2AlC single phase, with smaller TiAl_3 phases. High concentrations of Al were observed in the areas where TiAl_3 was identified. The TiAl_3 existed as small grains in between the Ti_2AlC grains. Figure 4-2(a) shows an overall view of the EBSD pattern. The Phase analysis by EBSD showed that Ti_2AlC was 98.5% and TiAl_3 was 1.5%. The points in the pole figure of the observed area dispersed rather than concentrated in one area (Figure 4-2(b)), demonstrating that the Ti_2AlC crystal planes were randomly distributed without a preferred orientation, despite the fact that the Ti_2AlC ceramic was sintered at 30 MPa. The length distributions of the short and long sides of the Ti_2AlC crystals obtained via analysis of the EBSD reveals that the modes of the long and short sides of the grains were 24 and 6 μm , respectively, while the longest grain had a long side of 78 μm (Figure 4-2(c)). The distribution of the aspect ratio of the grains (Figure 4-2(d) is referred to as a_g/c_g , where a_g (grain size of the major axis) and c_g (grain size of the minor axis) are the lengths of the long and short sides, respectively. The mode and maximum values of the aspect ratio were approximately 2 and 10, respectively, which indicates a power law distribution.

4.3.2 Roughness and cutting mode

An SEM image of the Ti₂AlC ceramic cutting surface reveals a series of cutting marks in concentric circles in the cutting direction (Figure 4-3(a)). The cutting chips of the Ti₂AlC ceramic (Figure 4-3(b)) were not streamlined but granular, with a grain size of approximately 2 μm, which shows the unique layered structure of MAX phase ceramics.

Figure 4-4(c-d) shows scanning electron microscopy images of an end-mill tip before and after the cutting test. No extreme wear was observed on the end-mill inserts after ten cuts on Ti₂AlC. The average R_a and R_z of the Ti₂AlC cutting surface were 0.7 and 5.4 μm, respectively (Figure 4-5); deep spikes were observed in some places. No significant reduction in R_a nor any macroscopic tool failure was observed after ten cuts with the same tool (Figure 4-5(b)), which indicates that Ti₂AlC causes minimal damage to the cutting tool. The roughness profile of the graphite surface showed several deep spikes similar to those observed in that of Ti₂AlC, while the average R_a and R_z of the graphite cutting surface were 0.4 and 2.5 μm, respectively. The tool steel cutting surface exhibited average R_a and R_z of 0.3 and 1.8 μm, respectively, with no large spikes being observed. The surface roughness parameters (including R_a and R_z) of all the cutting test samples were in the range of the second of the four grades defined in the JIS B 0601:1994 standard; accordingly, Ti₂AlC is classified in the same category as tool steel in terms of surface roughness.

Figure 4-6 shows the amplitude distributions of the surface roughness profiles shown in Figures 4-5(a), (c), and (d). The amplitude distribution of the Ti₂AlC ceramic shows an upward shift in the vertex position with respect to a normal distribution, while the negative side of the distribution has a wider base than those of graphite and tool

steel. The R_{sk} values for the amplitude distributions of the Ti_2AlC , graphite, and tool steel were -1.1, -0.7, and -0.004, respectively, indicating that the graphite and Ti_2AlC samples had deeper spikes on the surface than the tool steel sample. The Ti_2AlC and graphite were cut in brittle mode, resulting in significant cracking from the surface toward the interior. The R_{sk} of the tool steel was close to zero. The peaks and valleys of the tool steel cutting traces formed symmetrically, suggesting that it was cut in ductile mode; however, the surface roughness of the Ti_2AlC ceramics was in the same category as that of the tool steel, despite being cut in brittle mode.

4.3.3 Bending strength and behavior

The average bending strength of the machined Ti_2AlC specimens was equal to or slightly lower than that of the polished specimens with R_a values below $0.05\ \mu m$ (Figure 4-7(a)). The bending strengths of the machined and polished Ti_2AlC specimens were $353 \pm 27\ MPa$ and $376 \pm 19\ MPa$, respectively. Only a 6% reduction in the bending strength of the machined specimens was observed, even as the R_a value increased by a factor of ten or more owing to the cutting process. The value of K_{IC} of the Ti_2AlC ceramic evaluated via the SENB method was $6.9 \pm 0.1\ MPam^{1/2}$, approximately 1.5 times higher than that of alumina [21]. SEM images of the fracture surface of the machined specimen with the lowest strength show that the specimen eventually fractured across the entire machined surface, and several fracture initiation sites attributed to cutting-induced cracks were observed (Figures 4-7(b)–(d)). Numerous cracks related to kink deformation were observed around the fracture initiation sites.

4.3.4 Cutting-induced damages

The machined Ti₂AlC specimens exhibited grain detachment and kink deformation on the cutting surface caused by the cutting stress (Figure 4-8(g)). Grooves with a depth of approximately 10 μm formed on the machined surface owing to grain loss (Figure 4-8(h)). SEM and EBSD analyses showed that the cracks introduced by cutting stopped after growing to the size of approximately one grain and did not extend across the grains (Figure 4-8 (h) and (i)). The KAM values of the cutting surfaces were higher than those of the polished surfaces; the areas with increased KAM values were limited by the depth of one grain. The basal slip of MAX phase ceramics occurs preferentially along the $\langle 11\bar{2}0 \rangle$ direction at room temperature and other slip systems are less active [7,31]. The damage introduced by cutting is most likely cracks along the $\langle 11\bar{2}0 \rangle$ direction within the single grain. These cracks may affect the mechanical strength of machined Ti₂AlC ceramics.

4.4 Discussion

4.4.1 Cutting-induced damage mechanism in the MAX phase

Figure 4-9 shows schematic of the cutting damage during end-mill cutting of the Ti₂AlC ceramics. The cutting damage on the surface of the machined specimens consists of intergranular fracture, intragranular fracture with kink formation, and plastic deformation as shown in Figure 4-9. The Ti₂AlC ceramic chips generated by cutting in brittle mode were smaller than the surface grooves and crystal grains. The Ti₂AlC cutting mechanism is considered to be cutting while breaking the layered structures of the grains owing to the end-mill cutting edge, rather than the grain shedding observed in

other machinable ceramics [33]. Grain dropping because of intergranular fracture near the cutting edge was studied by measuring the surface roughness. Other types of subsurface damage such as intragranular cracks or strain due to plastic deformation cannot be precisely evaluated using the 2 μm stylus tip, and thus, cannot be evaluated by measuring the surface roughness. The cutting-induced cracks strongly influence the bending strength [2,3]. The intragranular cracks and strain introduced in the machined specimens stopped at approximately the size of one grain, as shown by SEM and EBSD shown in figure 4-8. Accordingly, the surface roughness does not affect the mechanical strength because the intragranular cracks are much deeper than the valleys in the machined surface. The compressive strain generated on the machined surface had no significant influence on the mechanical strength because the residual strain was only applied to the outermost layer of the machined surface. The damage is limited to nearly one grain without the formation of large cracks because of the layered structure of randomly distributed unoriented grains in the Ti_2AlC ceramics, which causes plastic deformation and pseudo-plastic deformation by kink formation. The high K_{IC} values of Ti_2AlC ceramics can be explained in the same way.

4.4.2 Fracture mechanics analysis

To possess higher strength after cutting without final polishing is advantageous in real applications of machinable ceramics. The fracture strength of the machined specimens was slightly lower than that of the polished specimens. The fracture initiation sites are thought to be through-cracks formed via the connection of multiple surface machining cracks with high aspect ratios corresponding to the grain aspect ratio. The

effects of the observed machining cracks on the bending strength of the ceramics were evaluated in terms of nonlinear elastic fracture mechanics (NLEFM) [34-38].

The fracture of brittle materials is typically described by linear elastic fracture mechanics (LEFM), as follows:

$$\sigma_F = \frac{K_{IC}}{\sqrt{\pi a_e}} = \frac{K_{IC}}{F\sqrt{\pi c}} \quad (4-4)$$

where σ_F is the fracture strength, a_e is the equivalent crack size, and c is the crack size.

In this study, the cutting-induced cracks were comparable in size to the grains (see Section 4.1). The fracture strength is nonlinear in such submicron-scale defect regions because the small-scale yield condition is not satisfied [34–36]. The fracture strength within the microcrack region can be predicted from the process zone size at the crack tip according to equation (4-5)[35]:

$$\sigma_F = A \cos \left\{ \frac{8a_e \sigma_o^2}{\pi K_{IC}^2 + 8a_e \sigma_o^2} \right\} \frac{2\sigma_o}{\pi} = A \cos \left\{ \frac{8cF^2 \sigma_o^2}{\pi K_{IC}^2 + 8cF^2 \sigma_o^2} \right\} \frac{2\sigma_o}{\pi} \quad (4-5)$$

where σ_o is the strength of the specimen without surface cracks. In this study, the maximum σ_F value of the polished specimen was assumed to be equal to σ_o [37,38], and the K_{IC} value of 6.9 MPam^{1/2} was used in Eq. (4-5).

To evaluate the fracture initiated from a through-crack formed by multiple connecting surface machining cracks with high aspect ratios corresponding to the grain aspect ratio, we considered fractures from semi-elliptical surface cracks and through surface cracks. The Newman–Raju equation [39] was employed to calculate the

geometric factor F of each type of crack. Figure 10 shows the relationship between the aspect ratio and F value of the semi-elliptical surface crack as a function of depth. The value of F of the crack front at the surface (point A) and the deepest point (point B) were evaluated as shown in Figure 10. The F value was plotted from the aspect ratio $a/c = 0.04$, where a is the thickness of the bending specimen and c is the maximum grain size. The F value at point A increases significantly with an increase in the crack aspect ratio and becomes essentially constant as the crack aspect ratio approaches 1. Thus, aspect ratios greater than 1 are expected to exhibit similar F values to that of an aspect ratio of 1. The intersection of F at points A and B appears at $a/c \sim 0.8$. The machining crack propagation behavior can be discussed in terms of the cracks that begin to propagate at the point with the highest F value. In the Ti_2AlC MAX phase ceramic, the observed surface machining cracks with $a/c > 4$ (corresponding to $a_g/c_g > 2$) are expected to propagate from the surface (point A) and until the aspect ratio reaches the intersection.

Based on the evaluation of F , the bending strengths of the through-crack ($a/c = 0$), semi-elliptical ($a/c = 1.0$), and semi-elliptical cracks (at the intersection) were calculated. Figure 11 shows the influence of the crack depth a on the calculated bending strength σ_F . Assuming that the maximum machining crack depth corresponds to the maximum grain size (a_g) of $78 \mu\text{m}$, the minimum strength of semi-elliptical and through-cracks was estimated to be approximately 332 and 287 MPa, respectively. A comparison of the calculated and measured bending strengths showed that the σ_F values of the machined specimens fell within the range of the estimated minimum σ_F values of the through-crack, but not within that of a single semi-elliptical crack. We therefore concluded that the strength of machined Ti_2AlC ceramics can be conservatively

predicted by assuming the cutting crack shape to be a through-crack with the same depth as the maximum grain size. This assumption is reasonable because the cutting-induced cracks are confined to approximately the size of a single grain.

The microstructure of the Ti_2AlC ceramics determines their machinability and mechanical strength. The bending strength of the machined specimens can be increased by reducing the grain size. Further improvements in the mechanical properties of Ti_2AlC ceramics are expected by reducing the grain size while maintaining the unique microstructure of MAX phase ceramics. However, when the crystal structure of Ti_2AlC and cutting conditions are changed, the machinability and mechanical strength after cutting may change. Further research on machinability and fracture mechanisms is needed to implement Ti_2AlC as an industrial product. Detailed Machinability study of materials involves various parameters like cutting at a different speed, feed, depth of cut, etc. The machinability of Ti_2AlC is more clearly revealed by conducting cutting tests under other cutting conditions. Furthermore, Weibull statistics analysis can be useful for detailed discussion for reliability of machined components. We have proposed a computational framework that can predict the Weibull distribution of bending strength from the microstructural features, pore size distribution in brittle ceramics, and surface defect size introduced by machining process [33]. In future work, we will evaluate and discuss the fracture statistics and reliability of machinable Ti_2AlC cooperating with these computational techniques.

4.5 Conclusions

The influence of cutting damage on the bending strength of Ti_2AlC ceramics was investigated via microstructural observation and fracture mechanics. The crystal

planes of the as-sintered Ti_2AlC ceramics were found to be randomly distributed without preferential orientation. The grains were elongated and had an aspect ratio of approximately 2; the longest grain had a length of 78 μm . The roughness profile of the cutting surface after 100- μm cutting with a cemented carbide end mill showed that the R_{sk} of the Ti_2AlC ceramics was -1.1, which indicated that the cutting was in brittle mode, similar to that of graphite. However, the roughness classification of the Ti_2AlC was comparable to that of tool steel, which corresponds to ductile mode cutting. SEM and EBSD observations of the Ti_2AlC cutting surfaces showed that the cutting damage stopped at approximately one grain size. The bending strength of the machined Ti_2AlC specimens was 353 ± 27 MPa, which is nearly as high as that of the polished specimens (376 ± 19 MPa). The decrease in bending strength owing to the machining was of only 6%. The minimum strength was calculated via NLEFM, assuming that multiple semicircular cracks with a height equal to the length of the longest grain behaved as a through-crack. The minimum strength was 287 MPa, and the bending strength of the machined specimens was within the range of the minimum strength. These results suggest that no significant reduction in bending strength occurs when cutting in brittle mode because the damage is confined to the size of a single grain. The bending strength of machined Ti_2AlC can be estimated via nonlinear fracture mechanics using subsurface damage values corresponding to the microstructure sizes. Ti_2AlC ceramics were shown to be highly practical structural machinable ceramics that do not suffer significant reductions in bending strength upon machining, and thus, may not require subsequent polishing.

References

- [1] S. Malkin, T.W. Hwang, Grinding mechanisms for ceramics, *CIRP Annals* 45 (1996) 569–580.
- [2] R.W. Rice, J.J. Mecholsky, P.F. Becher, The effect of grinding direction on flaw character and strength of single crystal and polycrystalline ceramics, *J. Mater. Sci.* 16 (1981) 853–862.
- [3] M. Gruber, A. Leitner, I. Kraveva, D. Kiener, P. Supancic, R. Bermejo, Understanding the effect of surface flaws on the strength distribution of brittle single crystals, *J. Am. Ceram. Soc.* 101 (2018) 5705–5716.
- [4] K. Kanda, S. Takehana, S. Yoshida, R. Watanabe, S. Takano, H. Ando, F. Shimakura, Application of diamond-coated cutting tools, *Surf. Coat. Technol.* 73 (1995) 115–120.
- [5] V. Bharathi, A.R. Anilchandra, S.S. Sangam, S. Shreyas, S.B. Shankar, A review on the challenges in machining of ceramics, *Mater. Today Proc.*, 46 (2021) 1451–1458.
- [6] J.S. Reed, J.S. Reed, *Principles of ceramics processing*, John Wiley & Sons, New York, 1995.
- [7] M.W. Barsoum, *MAX phases: properties of machinable ternary carbides and nitrides*, Wiley-VCH, Weinheim, 2013.
- [8] N. Yamaguchi, M. Okada, K. Yanagisawa, Y.-L. Kuo, M. Nanko, New material for screws –The potential of Ti₂AlC ceramic screw components, *J. Jpn. Soc. Precis. Eng.* 87 (2021) 353–357.

- [9] S.S. Hwang, S.C. Lee, J.H. Han, D. Lee, S.W. Park, Machinability of Ti_3SiC_2 with layered structure synthesized by hot pressing mixture of TiC_x and Si powder, *J. Eur. Ceram. Soc.* 32 (2012) 3493–3500.
- [10] C.F. Hu, Y.C. Zhou, Y.W. Bao, Material removal and surface damage in EDM of Ti_3SiC_2 ceramic, *Ceram. Int.* 34 (2008) 537–541.
- [11] M.W. Barsoum, The $\text{M}_{N+1}\text{AX}_N$ phases: A new class of solids: thermodynamically stable nanolaminates, *Prog. Solid State Chem.* 28 (2000) 201–281.
- [12] M.W. Barsoum, M. Radovic, Elastic and mechanical properties of the MAX phases, *Annu. Rev. Mater. Res.* 41 (2011) 195–227.
- [13] M. Radovic, M.W. Barsoum, MAX phases: Bridging the gap between metals and ceramics, *American Ceramic Society Bulletin.* 92 (2013) 20–27.
- [14] M. Haftani, M. Saeedi Heydari, H.R. Baharvandi, N. Ehsani, Studying the oxidation of Ti_2AlC MAX phase in atmosphere: A review, *Int. J. Refract. Metals Hard Mater.* 61 (2016) 51–60.
- [15] T. Osada, A. Watabe, J. Yamamoto, J.C. Brouwer, C. Kwakernaak, S. Ozaki, S. van der Zwaag, W.G. Sloof, Full strength and toughness recovery after repeated cracking and healing in bone-like high temperature ceramics, *Sci. Rep.* 10 (2020) 18990.
- [16] S. Li, G. Song, K. Kwakernaak, S. van der Zwaag, W.G. Sloof, Multiple crack healing of a Ti_2AlC ceramic, *J. Eur. Ceram. Soc.* 32 (2012) 1813–1820.
- [17] G.M. Song, V. Schnabel, C. Kwakernaak, S. van der Zwaag, J.M. Schneider, W.G. Sloof, High temperature oxidation behavior of Ti_2AlC ceramic at 1200°C , *Mater. High Temp.* 29 (2012) 205–209.

- [18] D.J. Tallman, B. Anasori, M.W. Barsoum, A critical review of the oxidation of Ti_2AlC , Ti_3AlC_2 and Cr_2AlC in Air, *Mater. Res. Lett.* 1 (2013) 115–125.
- [19] L. Cai, Z. Huang, W. Hu, S. Hao, H. Zhai, Y. Zhou, Fabrication, mechanical properties, and tribological behaviors of Ti_2AlC and $\text{Ti}_2\text{AlSn}_{0.2}\text{C}$ solid solutions, *J. Adv. Ceram.* 6 (2017) 90–99.
- [20] P. Wang, B.-C. Mei, X.-L. Hong, W.B. Zhou, Synthesis of Ti_2AlC by hot pressing and its mechanical and electrical properties, *Trans. Nonferr. Met. Soc.* 17 (2007) 1001–1004.
- [21] G.A. Gogotsi, Fracture toughness of ceramics and ceramic composites, *Ceram. Int.* 29 (2003) 777–784.
- [22] C. Guo, E. Wang, Y. Liu, Y. Zheng, T. Yang, X. Hou, Effect of Sn doping concentration on the oxidation of Al-containing MAX phase (Ti_3AlC_2) combining simulation with experiment, *Fundamental Research.* 2 (2022) 114–122.
- [23] C. Guo, X. Duan, Z. Fang, Y. Zhao, T. Yang, E. Wang, X. Hou, A new strategy for long-term complex oxidation of MAX phases: Database generation and oxidation kinetic model establishment with aid of machine learning, *Acta Mater.* 241 (2022) 118378.
- [24] X. Duan, Z. Fang, T. Yang, C. Guo, Z. Han, D. Sarker, X. Hou, E. Wang, Maximizing the mechanical performance of Ti_3AlC_2 -based MAX phases with aid of machine learning, *Journal of Advanced Ceramics* 2022 11:8. 11 (2022) 1307–1318.
- [25] T. Osada, W. Nakao, K. Takahashi, K. Ando, S. Saito, Strength recovery behavior of machined $\text{Al}_2\text{O}_3/\text{SiC}$ nano-composite ceramics by crack-healing, *J. Eur. Ceram. Soc.* 27 (2007) 3261–3267.
- [26] D.D.L. Chung, Exfoliation of graphite, *J. Mater. Sci.* 22 (1987) 4190–4198.

- [27] S. Luthfiyah, A. Faridh, B. Soegijono, The effect of vacuum quenching on corrosion and hardness of the surface of SKD61 steel, *IOP Conf Ser Mater Sci Eng.* 694 (2019) 1-9.
- [28] E.S. Gadelmawla, M.M. Koura, T.M.A. Maksoud, I.M. Elewa, H.H. Soliman, Roughness parameters, *J. Mater. Process. Technol.* 123 (2002) 133–145
- [29] E.K. Antwi, K. Liu, H. Wang, A review on ductile mode cutting of brittle materials, *Front. Mech. Eng.* 13 (2018) 251–263.
- [30] H. Huang, X. Li, D. Mu, B.R. Lawn, Science and art of ductile grinding of brittle solids, *Int. J. Mach. Tools Manuf.* 161 (2021) 103675.
- [31] N.F. Strey, C. Scandian, Abrasive polishing load effect on surface roughness and material removal rate of Al₂O₃, ZTA and SiC, *Wear*, 477 (2021) 203787.
- [32] A.D. Bakker, Evaluation of elastic fracture mechanics parameters for bend specimens, *Int. J. Fract.* 71 (1995) 323–343.
- [33] J.B. Davis, D.B. Marshall, R.M. Housley, P.E.D. Morgan, Machinable ceramics containing rare-earth phosphates, *J. Am. Ceram. Soc.* 81 (1998) 2169–2175.
- [34] S. Usami, H. Kimoto, I. Takahashi, S. Shida, Strength of ceramic materials containing small flaws, *Eng Fract Mech.* 23 (1986) 745–761.
- [35] K. Ando, B.A. Kim, M. Iwasa, N. Ogura, PROCESS ZONE SIZE FAILURE CRITERION AND PROBABILISTIC FRACTURE ASSESSMENT CURVES FOR CERAMICS, *Fatigue Fract Eng Mater Struct.* 15 (1992) 139–149.
- [36] C. Ito, T. Osada, S. Ozaki, Finite element analysis of fracture behavior in ceramics: Competition between artificial notch and internal defects under three-point bending, *Ceram. Int.* 48 (2022) 36460-36468.

- [37] N. Sato, K. Takahashi, Evaluation of fracture strength of ceramics containing small surface defects introduced by focused ion beam, *Materials*. 11:3 (2018) 457.
- [38] T. Osada, T. Hara, M. Mitome, S. Ozaki, T. Abe, K. Kamoda, T. Ohmura, Self-healing by design: universal kinetic model of strength recovery in self-healing ceramics, *Sci Technol Adv Mater*. (2020) 593–608.
- [39] J.C. Newman, I.S. Raju, An empirical stress-intensity factor equation for the surface crack, *Eng. Fract. Mech.* 15 (1981) 185–192.

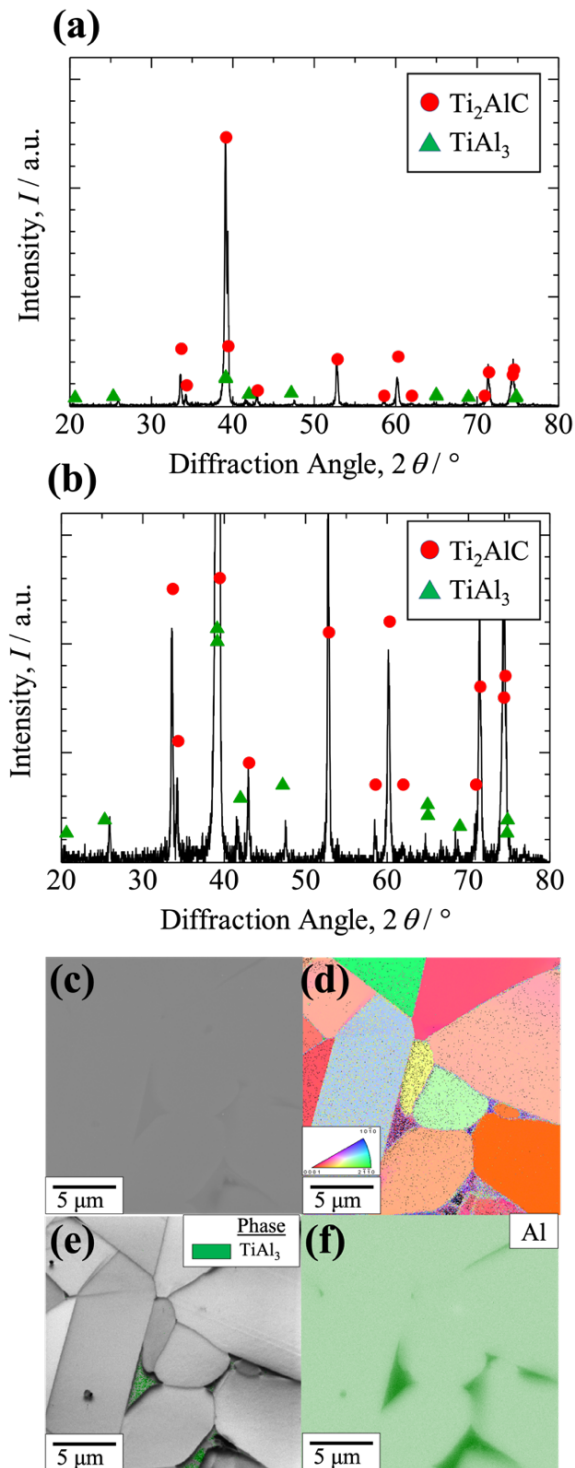


Figure 4-1 Composition of the sintered Ti_2AlC ceramic. (a) X-ray diffraction profiles; (b) X-ray diffraction profiles with the bottom portion enlarged; (c) backscattered electron image of the observed section; (d) inverse pole figure map of the observed section; (e) phase map of TiAl_3 ; (f) elemental map of Al in the observed section.

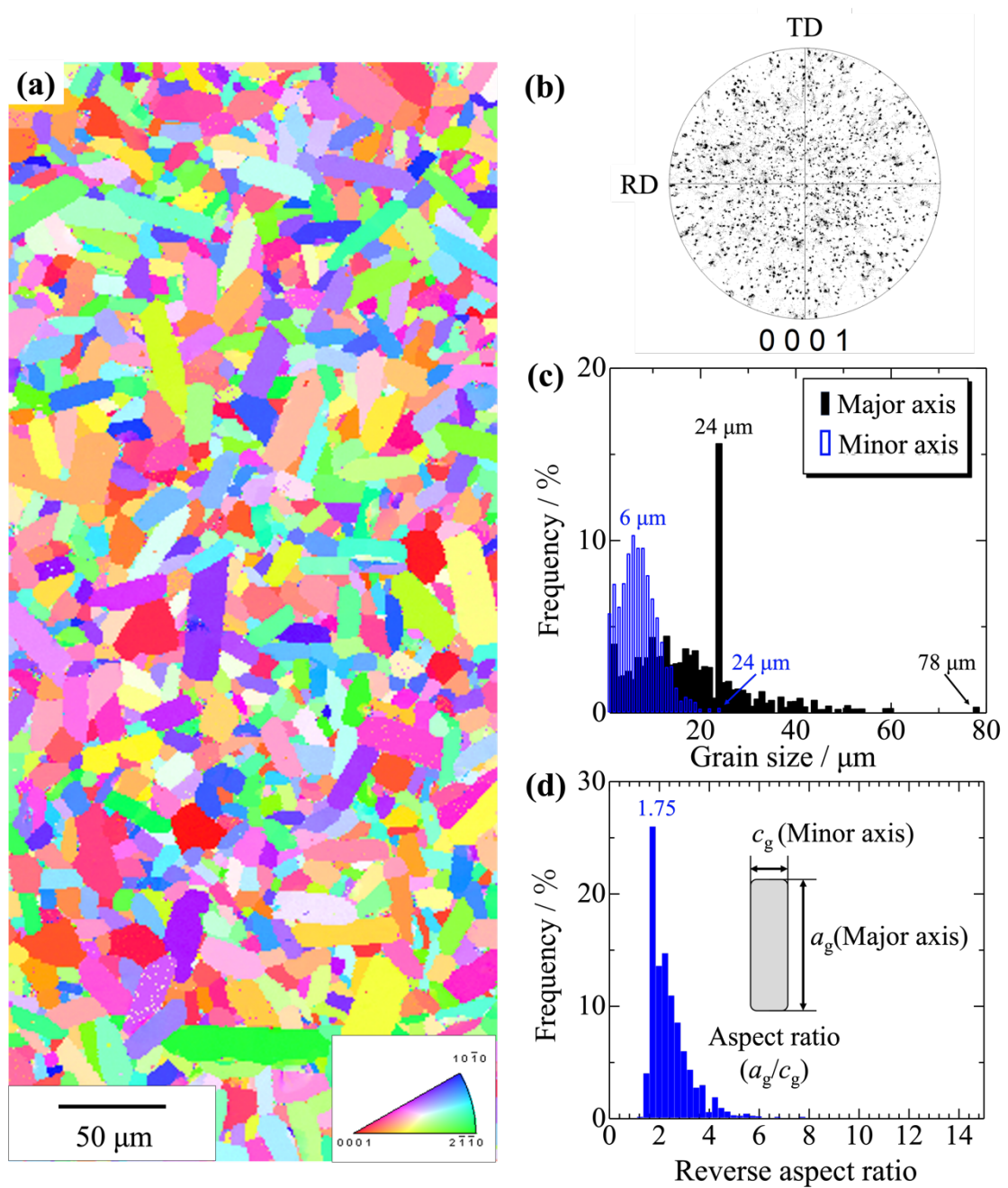


Figure 4-2 Grain analysis of Ti_2AlC ceramics via scanning electron microscopy and backscattered electron diffraction. (a) Inverse pole figure map of the observed section; (b) pole figure of the observed section; (c) grain size distributions along the major and minor axis; (d) aspect ratio distribution (c_g/a_g).

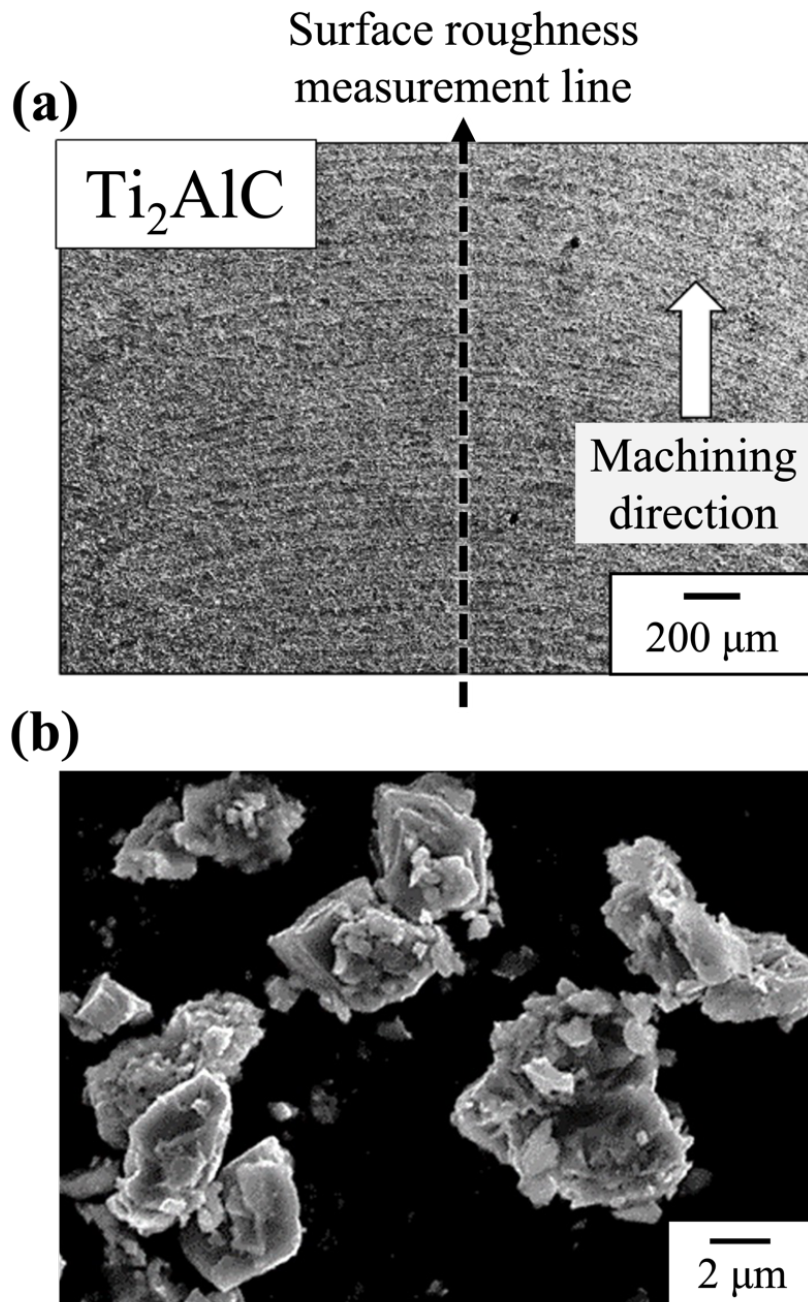
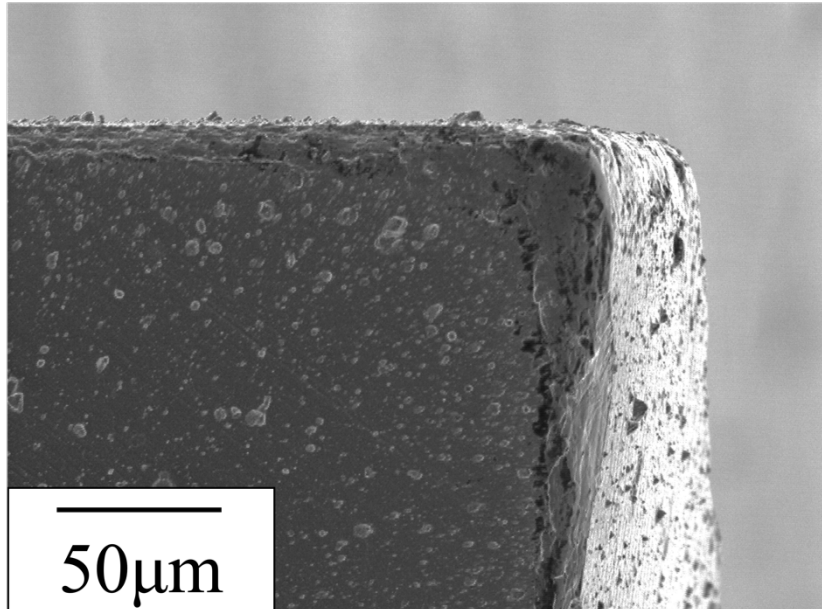


Figure 4-3 Scanning electron microscopy images of the machined Ti_2AlC ceramics. (a) Image of the cutting surface showing the surface roughness measurement along the machining direction; (b) image of the cutting chips.

(a)



(b)

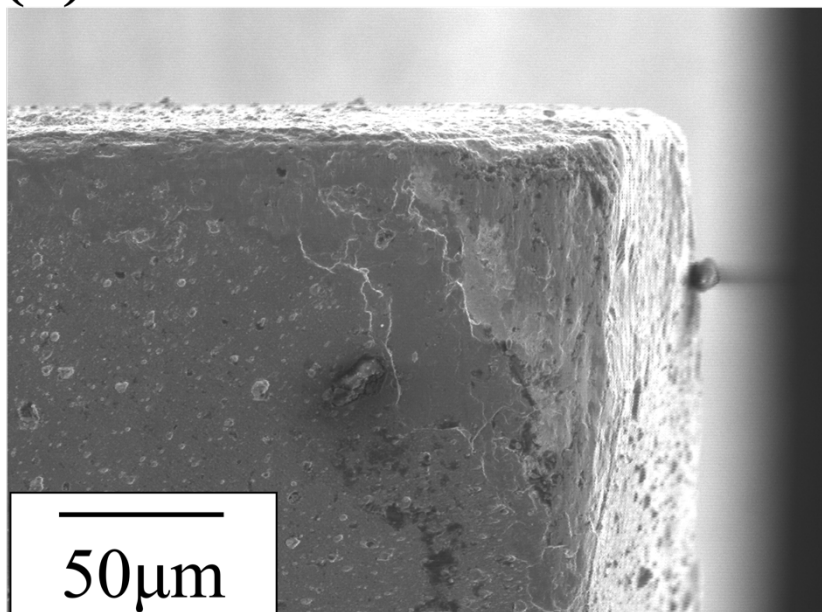


Figure 4-4 Scanning electron microscopy images of end-mill cutting edge. (a) Image of end-mill cutting edge before cutting; (b) Image of end-mill cutting edge after 10 cuts.

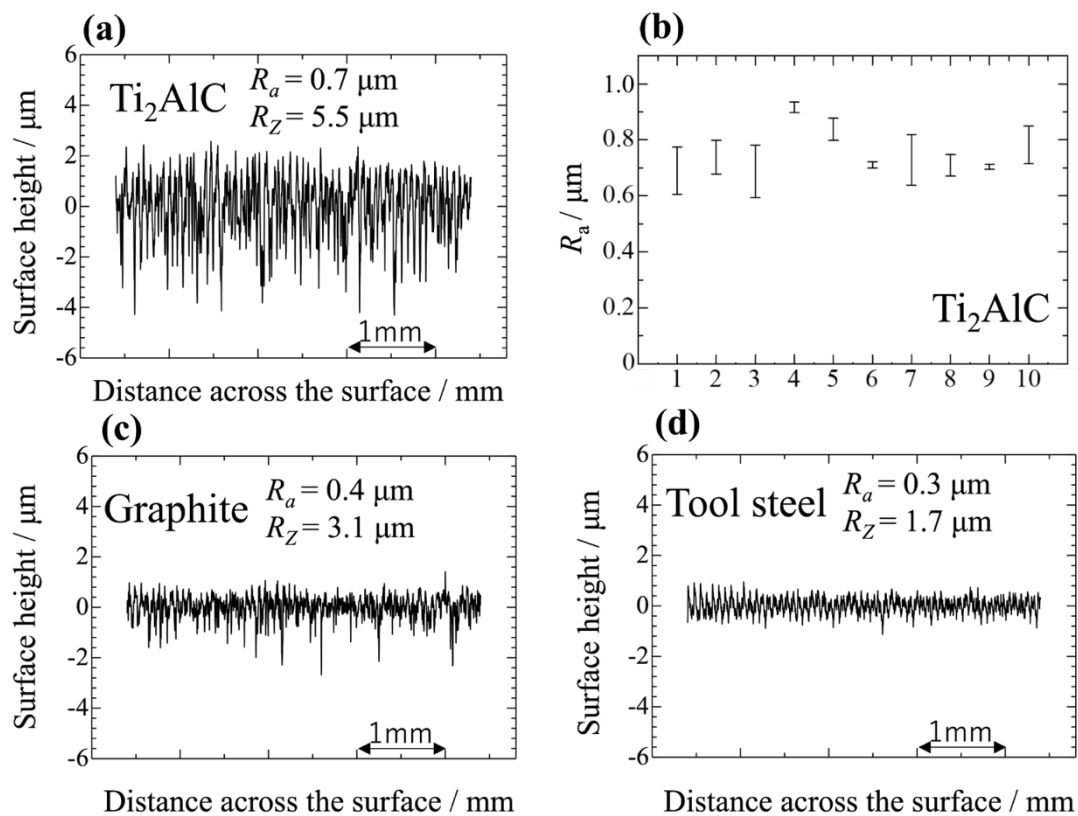


Figure 4-5 Surface roughness measurement of the milled samples. (a) Surface profile of the machined Ti₂AlC ceramics; (b) arithmetic mean roughness (R_a) of the Ti₂AlC ceramics ($N=10$); (c) surface profile of the machined graphite; (d) surface profile of the machined tool steel.

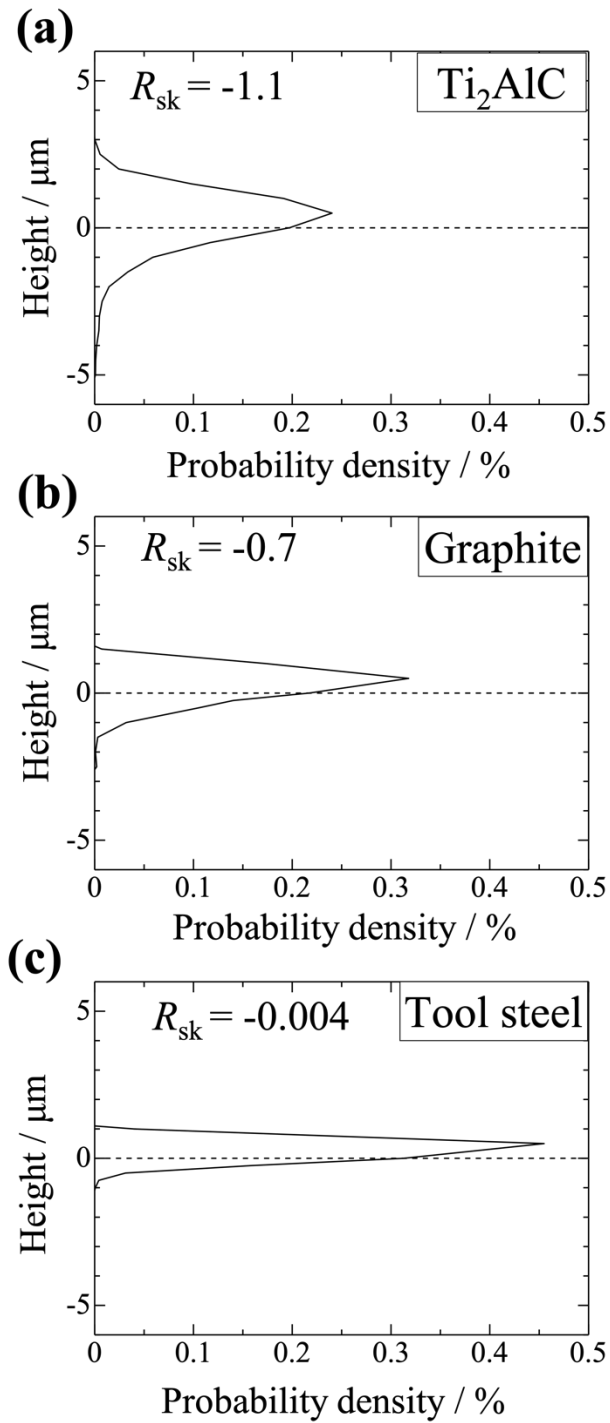


Figure 4-6 Amplitude distributions of the surface profiles of the milled samples: (a)Ti₂AlC, (b) graphite, and (c) tool steel.

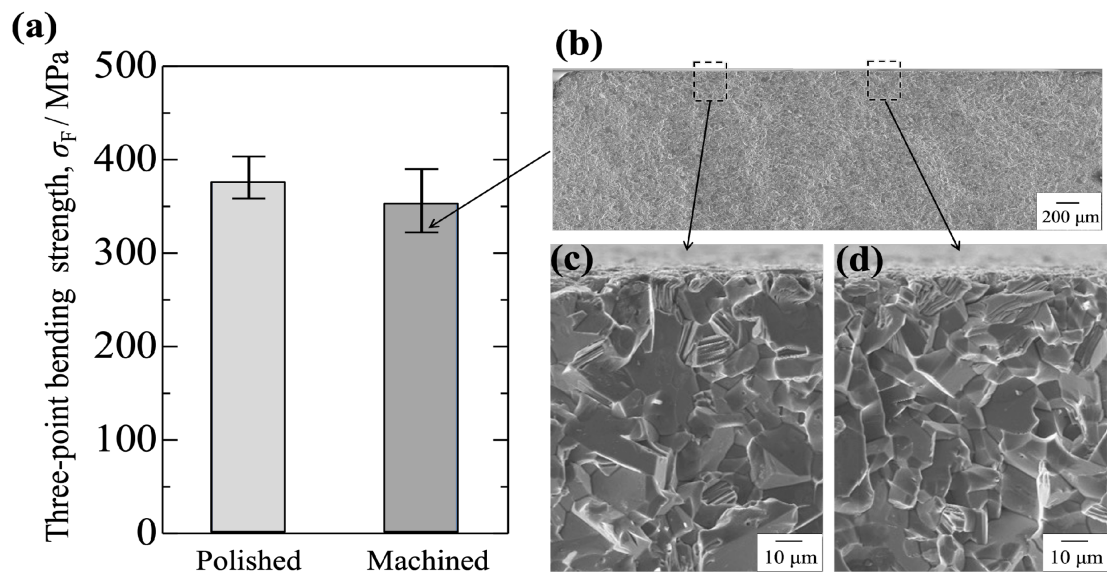


Figure 4-7 Bending tests and fracture surface microstructure. (a) Bar graph of the bending strength of the polished and machined Ti₂AlC ceramic samples; the error bars represent the maximum and minimum values. (b) Scanning electron microscopy (SEM) image of the fracture surface of the machined Ti₂AlC ceramic specimen with the lowest bending strength. (c-d) SEM images of the fracture surface around the fracture origin.

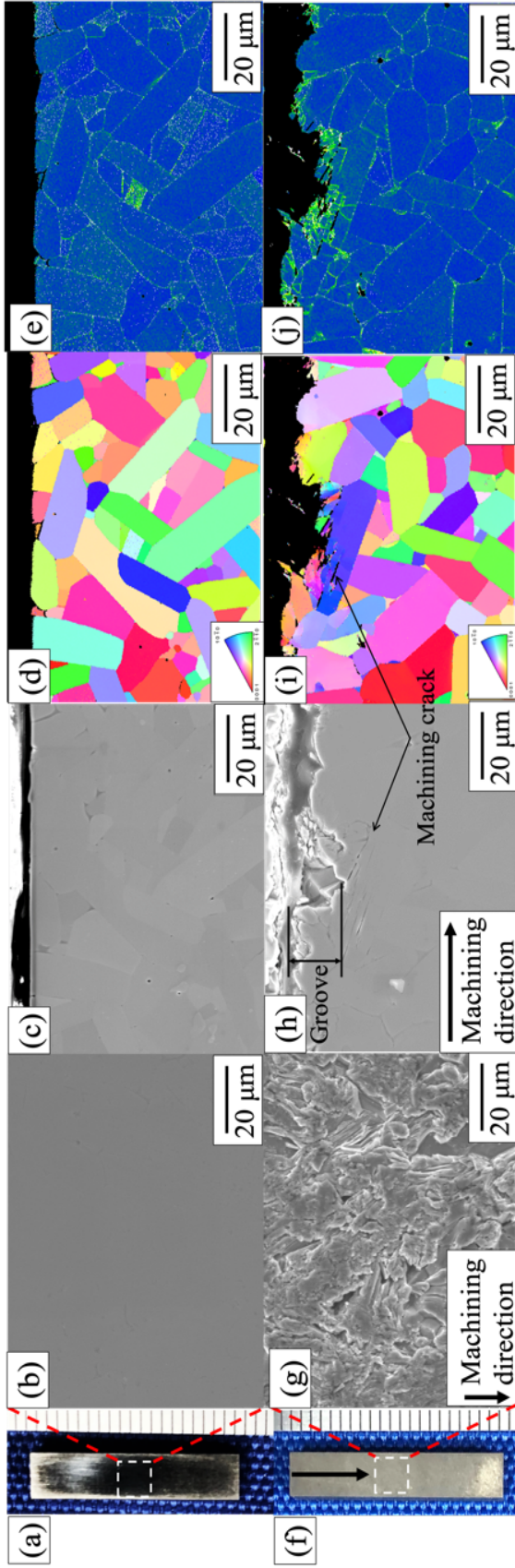


Figure 4-8 Microstructures of polished (top row) and machined (bottom row) Ti_2AlC ceramics specimens. (a,f) Appearance of the polished and machined specimens; (b,g) backscattered electron images of the polishing and cutting surfaces; (c,h) backscattered electron images of the cross-sections; (d,i) backscattered electron diffraction inverse pole figure maps of the cross-sections, (e,f) kernel average misorientation maps of the cross-sections.

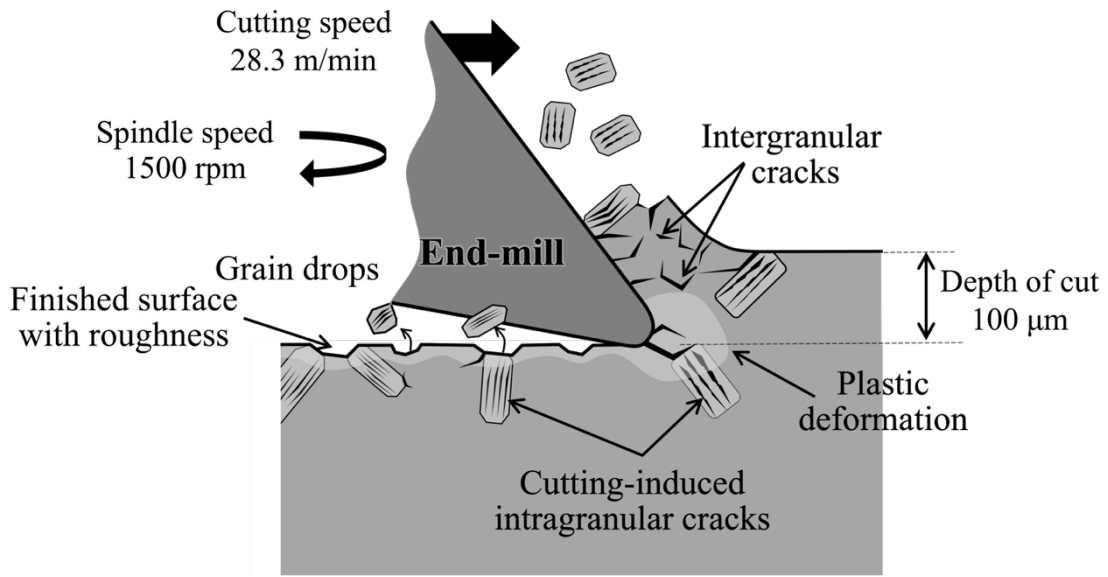


Figure 4-9 Schematic of the cutting damage during end-mill cutting of the Ti_2AlC ceramics.

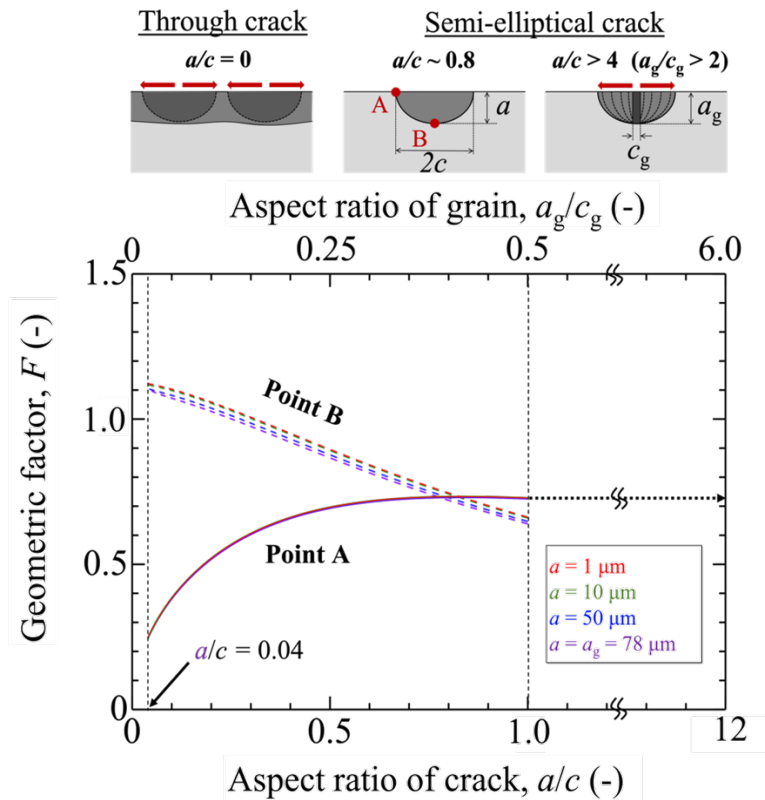


Figure 4-10 Geometric factor (F) vs. aspect ratio and initial crack height and expected F at point A at aspect ratios higher than 1.

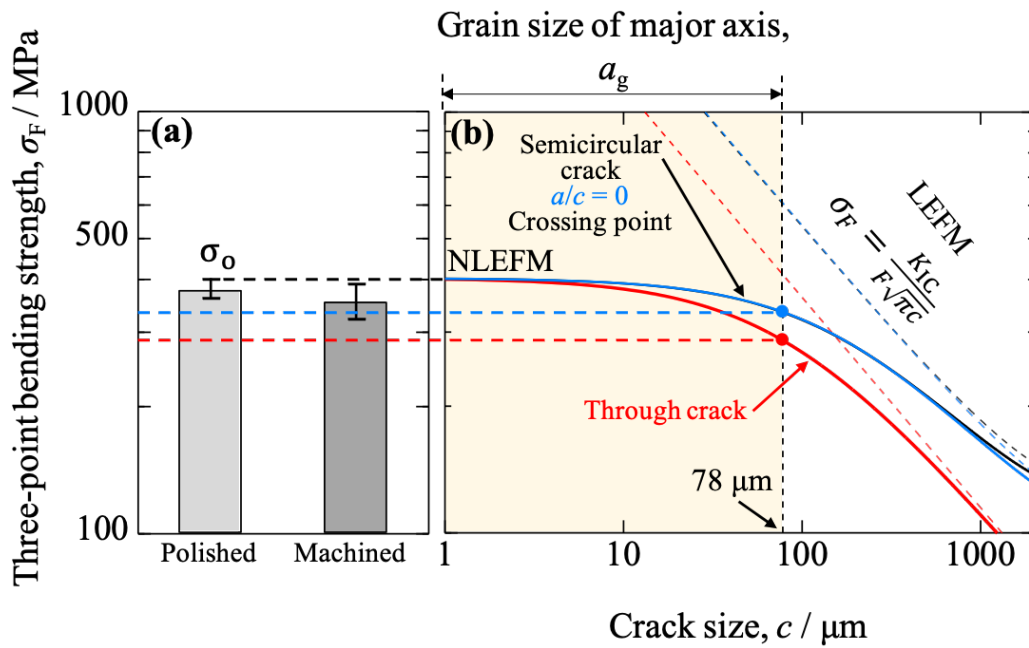


Figure 4-11 Minimum strength calculated via nonlinear fracture mechanics and actual bending strength. (a) Comparison of the bending strength of the polished and machined Ti_2AlC ceramics and the minimum strength. (b) Nonlinear fracture behavior of the Ti_2AlC ceramics and crack length.

Chapter 5: Materials design strategy for Ti₂AlC ceramics for high-temperature components

5.1 Introduction

The TRL level is necessary to be increased to promote MAX phase ceramics. Materials design strategy need to be developed to raise the TRL level above 2. The current material design phase is at phase 1 and does not control the synthesis process. Therefore, the properties of Ti₂AlC varied greatly, making it difficult to implement Ti₂AlC products in society. Chapters 2, 3 and 4 discussed oxidation resistance, mechanical strength, and machinability, which are particularly important for the application of Ti₂AlC ceramics to high-temperature material components. As a result, it became clear that material properties can be influenced by controlling dissimilar phases and additive elements. This knowledge can be used to establish materials design strategy for high-temperature components.

5.2 Summary of materials design strategy

In high-temperature environments for long periods or in repetitive oxidation conditions, high oxidation resistance is particularly important. In such cases, Ti₂AlC oxidation resistance can be improved by increasing the amount of Al to precipitate TiAl₃ or by adding Nb. Examples of Ti₂AlC ceramic products that require high strength include ceramics screw and Die for PECS as shown in Figure 5-1.

It is necessary to improve the strength by refining the crystal grains when Ti₂AlC is applied to parts that especially require bending strength. When Ti₂AlC is to be applied to a component that requires a particularly high fracture toughness value, it is

necessary to avoid grain refinement. In this case, the Ti content can be reduced to decrease TiC and coarsen the crystal grains. Ti₂AlC ceramics are expected to be used in products requiring high strength, such as injection molds and ceramic gears as shown in Figure 5-1.

Material design strategy for high-temperature components of Ti₂AlC ceramics were established. The material design phase could be Phase 2 because the synthesis state could be controlled. Figure 5-2 shows a summary of the material design guidelines.

5.3 Future of materials design strategy

To reach level 3 of TRL, all the material properties required by the market must be clarified by actually producing Ti₂AlC ceramic products. It is necessary to collaborate with companies for research and product fabrication. To make the material design phase to phase 3, it is necessary to disseminate the products and build a material database. Currently, machine learning and Materials informatics are being promoted. Ti-Al-C MAX phase ceramics are expected to further improve mechanical strength and oxidation resistance through composition optimization using machine learning [1,2]. The construction and utilization of a material properties database for Ti₂AlC ceramics will promote the social implementation of Ti₂AlC ceramic products.

5.4 Conclusion

It is possible to control the properties of Ti₂AlC ceramics by controlling the different phases and adding elements. Material design guidelines were established for mechanical properties and oxidation resistance which are important for high-

temperature components. The material design phase for high-temperature components of Ti_2AlC ceramics has reached Phase 2 on a limited basis.

References

- [1] C. Guo, X. Duan, Z. Fang, Y. Zhao, T. Yang, E. Wang, X. Hou, A new strategy for long-term complex oxidation of MAX phases: Database generation and oxidation kinetic model establishment with aid of machine learning, *Acta Mater.* 241 (2022) 118378.
- [2] X. Duan, Z. Fang, T. Yang, C. Guo, Z. Han, D. Sarker, X. Hou, E. Wang, Maximizing the mechanical performance of Ti_3AlC_2 -based MAX phases with aid of machine learning, *J. Adv. Ceram.* 11:8 (2022) 1307–1318.

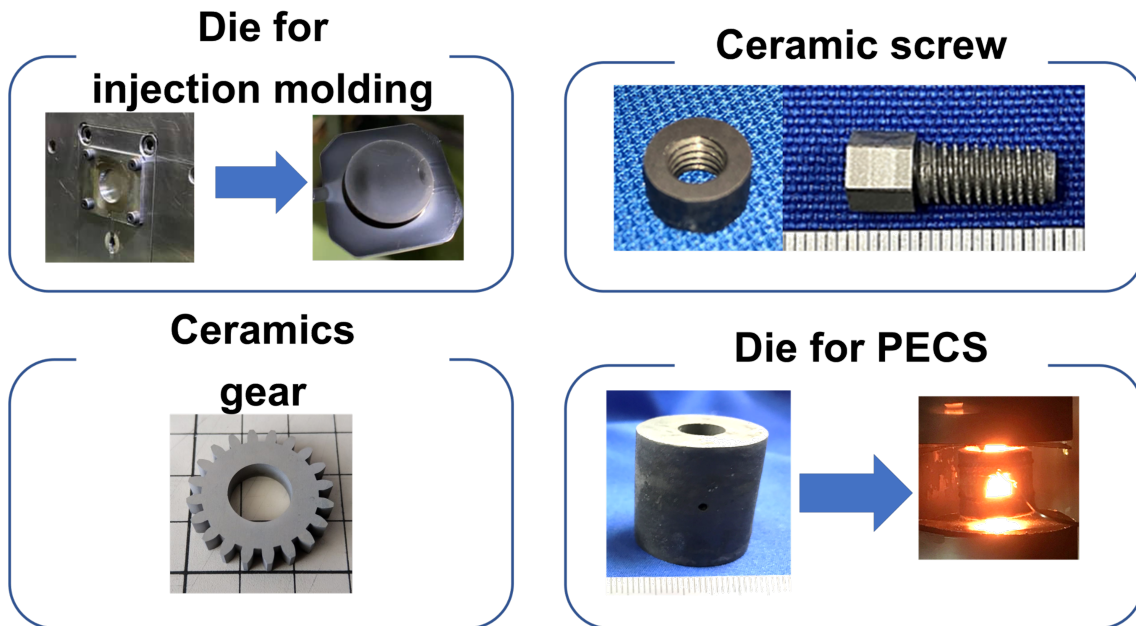


Figure 5-1 Examples of Ti₂AlC Ceramics Products.

		Oxidation resistance	
		Room temperature	High temperature
Mechanical strength	Low strength	<p>Normal Ti₂AlC</p> <p><u>Problems</u> Unstable in oxidation resistance and mechanical strength</p> <p>↓</p> <p>Difficult to commercialize</p>	<p>Solutions</p> <p>Al-rich or Nb doped Ti₂AlC</p> <p>Improved oxidation resistance</p> <p>↓</p> <p><u>Product Examples</u> High-temp. ceramic screw Die for PECS</p>
	High strength	<p>Solution</p> <p>Al-poor Ti₂AlC</p> <p>Improved mechanical strength</p> <p>↓</p> <p><u>Product Examples</u> Die for injection molding Ceramics gear</p>	<p>Future research</p> <p>Optimization of properties</p> <p>↓</p> <p><u>Material design phase 3</u> Construction of material database</p>

Figure 5-2 Summary of materials design strategy.

Chapter 6: The potential of Ti_2AlC ceramics

screw components

6.1 Introduction

Ti_2AlC ceramics are expected to be used as ceramic components in high-temperature environments. Screw components are expected to be one of the applications for Ti_2AlC ceramics. Ti_2AlC ceramics can be recycled at each production stage, consumption, and disposal, making it an ideal structural ceramic for building circular economy (CE). To form such CE, Ti_2AlC ceramics must be used in many products. It is necessary to promote the use of Ti_2AlC ceramics in screw parts, the most basic mechanical parts. In addition, as the concept of CE using Ti_2AlC ceramics spreads throughout the industry, it is expected that various materials other than Ti_2AlC ceramics will be developed that are suitable for CE formation. This will accelerate material-driven innovation. Carbon steels are the most common materials used for screws. Exports of carbon steel screws by category in trade statistics show that steel screws account for the overwhelming share of exports [1]. Carbon steel screws are heavy and cannot be used in high-temperature environments due to their poor oxidation resistance. For this reason, nonferrous metal screws are sometimes used for lightweight products or products used in high-temperature environments. Transportation equipment manufacturers are currently taking the lead in reducing the weight of machine parts to improve energy efficiency and reduce CO_2 emissions [2]. The machine parts can be made lighter by using screws that are lighter than steel screws. Typical lightweight screws include light metal screws made of aluminum alloys, titanium alloys, etc. and

plastic screws. These lightweight screws are expected to become more widespread, but their range of use is limited. The nonferrous metal screws cannot be used in high-temperature environments because of their low melting point and oxidation resistance. Screws in high-temperature environments include stainless steel screws, nickel alloy Inconel screws, and molybdenum alloy screws. Although these screws have high heat resistance, they are dense and heavy. Within this context, ceramic screws are expected for lightweight screws that can be used in high-temperature environments. Several companies sell ceramic threaded parts. The materials used in commercially available ceramic threaded parts are alumina and zirconia. These ceramic materials have lightweight, highly corrosion and heat resistant, and are expected to be used in high-temperature and corrosive environments. Commercially ceramic threaded parts can be produced in two main ways. The first is to slip-cast or injection-mold a molded part in the shape of a screw and then sinter it [3]. The second is to cut the green body into a screw shape and then sinter it [3].

The commercially ceramic threaded parts are not manufactured by cutting sintered ceramics. Therefore, the ceramic threaded parts are more expensive than metal or plastic threaded parts due to higher machining costs, and mass production is difficult.

Machinable ceramics can be cut with general tools. However, machinable ceramics have low mechanical strength [4]. In addition, it is difficult to cut to precise dimensions because cutting is based on the shedding of surface grains [5]. For this reason, general machinable ceramics are not used in products such as screw parts, which require precise shapes and high mechanical strength. Ideal ceramic materials for screw parts have free-machinability and high mechanical strength. Ti_2AlC MAX phase ceramics are expected to become such a material.

Ti₂AlC ceramics have high oxidation resistance, mechanical strength, and good machinability [6-9]. Furthermore, Ti₂AlC ceramics have self-healing capability [10-11]. Ti₂AlC ceramics can be used as a new material different from conventional screw materials. In order to apply Ti₂AlC ceramics to products, observing the thread shape after cutting and measuring the mechanical strength after cutting is necessary.

In this study, it was assumed that screw parts made of ceramics would be inexpensive and highly oxidation resistance. Therefore, Ti₂Al_{1.2}C_{0.9} was used based on the material design guidelines for Ti₂AlC ceramics. Ti₂Al_{1.2}C_{0.9} has high oxidation resistance without using expensive Nb. In this study, cutting tests were performed using a commercial cemented carbide tool on Ti₂AlC ceramics and other materials for comparison. Mechanical strength tests were also conducted on the machined Ti₂AlC ceramic screw parts.

6.2 Experimental

6.2.1 Materials

Commercial Ti (Kojundo Chemical Laboratory Co., Ltd.), Al (Kojundo Chemical Laboratory Co., Ltd.), and C (Aldrich Chemical Company), powders were mixed in a Ti:Al:C molar ratio of 2:1.2:0.9. The particle sizes of the Ti, Al, and C powders were 38 μm, 3 μm, and 1–2 μm, respectively, and the purity of each of the three powders was 99.9%. The powder mixture was treated in a vacuum at 1300 °C for 16 h in an alumina container before being dry-milled using a mortar. The obtained powder was consolidated for 15 min via a pulsed electric current sintering technique (LABOX-1550i75S, SinterLand Inc.) using a graphite die and punch at 1300 °C in a vacuum under 30 MPa uniaxial pressure. The dimensions of the sintered samples were

30 mm in diameter and 7 mm in height, and 10 mm in diameter and 5 mm in height.

The density was measured via the Archimedes method using toluene as the immersion medium to confirm the relative density and porosity of the sintered sample. Nearly fully densified Ti_2AlC ceramics were used. Phase identification was conducted via X-ray diffraction (XRD, Rigaku Corporation MiniFlex 600) using monochromatic $\text{Cu K}\alpha$ radiation.

6.2.2 Cutting process

In the case of nut fabrication, the Ti_2AlC ceramics were drilled with a diameter of 10 mm using a carbide drill. The holes were threaded with an M6 tap using a lathe under dry conditions. Thickness of the M6 nuts is 5 mm. The nut was cut with a ceramic cutter. The female threads of the nut were observed with a laser microscope. Al_2O_3 M6 nuts (WILCO.JP Co., Ltd.) were commercially available. In the case of bolt fabrication, the Ti_2AlC sintered body and glass-bonded mica (Nilaco Co., Ltd.) were cut into a square cylinder using a ceramic cutter. The outer circumference of the square prism was lathed using a carbide turning tool and then threaded to M6 using a threading tool. The thread length is 20 mm. The same threading conditions were also used for threading mica. Al_2O_3 M6 bolts (WILCO.JP Co., Ltd.) were commercially available. Table 6-1 shows the typical properties of Ti_2AlC , mica and Al_2O_3 [12]. The threaded part of the bolts was observed by laser microscopy.

6.2.3 Mechanical test

Load tests and guaranteed load tests of 6000 N were conducted on Ti_2AlC nuts and commercially available Al_2O_3 M6 nut following JIS B 1051. Figure 6-1 shows the

appearance of the compression test equipment. The nut threads were observed under a laser microscope after the compression test. Tensile load tests were conducted on Ti₂AlC ceramic bolts, mica bolts, and commercial Al₂O₃ M6 bolts (WILCO.JP Co., Ltd.) following JIS B 1051. Figure 6-2 shows the appearance of the tensile test apparatus.

6.3 Results

6.3.1 Thread shape of Ti₂AlC ceramic nut

Figure 6-3 shows the appearance of the Ti₂AlC ceramic nut and Al₂O₃ nut. There are no major deformations or surface cracks in the nut. Figure 6-4 shows a 3D image of a threaded part of a Ti₂AlC ceramic nut. There are no cracks or chips on the threads. The *R_a* values for the cutting surface of the Ti₂AlC ceramic nut and the Al₂O₃ nut were 2.7 and 3.5 μm respectively. The *R_a* value of the Ti₂AlC ceramic nut was lower than that of the commercial Al₂O₃ nut and no significant spikes were observed on the cutting surface.

6.3.2 Mechanical strength of Ti₂AlC ceramic nut

Figure 6-5 shows a compressive strength of the Ti₂AlC ceramic nut and Al₂O₃ nut. The compressive strength of the Ti₂AlC ceramic nut and Al₂O₃ nut were equal to be 4.6 and 3.5 kN respectively. The Ti₂AlC ceramic nut had a higher load strength than the Al₂O₃ nut. Figure 6-6 shows an appearance of a piece of nut after a compression test. The threads were not destroyed after the compression test. The results of the guaranteed load test on the Ti₂AlC ceramic nut showed that the strength was guaranteed up to 6000 N. Figure 6-7 show compressive strength of Ti₂AlC ceramics nut, CU1 (Electroplated copper) and AL1 (Aluminum alloy). The values for CU1 and AL1 are taken from JIS B

1051. Ti₂AlC ceramic nut has a higher guaranteed load rating than typical light alloy CU1 and AL1 nuts. Figure 6-8 shows a laser microscope image of the threads of a piece of Ti₂AlC ceramic nut after guaranteed load test. The threads were not destroyed even after the compression test.

6.3.3 Thread shape of Ti₂AlC ceramic bolt

Figure 6-9 shows the appearance of the Ti₂AlC ceramic bolt, mica bolt and Al₂O₃ bolt. There are no major deformations or surface cracks in the Ti₂AlC ceramic bolt. Figure 6-10 shows a 3D image of a Ti₂AlC ceramic bolt thread and mica bolt thread. The R_a values for the cutting surface of the Ti₂AlC ceramic bolt and the mica bolt were 4.6 and 6.5 μm respectively. There are no surface cracks or chips on the threads of the bolt made of Ti₂AlC ceramic. Threads of bolts made of mica are cracked and chipped.

6.3.4 Mechanical strength of Ti₂AlC ceramic bolt

Figure 6-11 shows tensile strength of the Ti₂AlC ceramic bolt, mica bolt and Al₂O₃ bolt. The tensile strength of the Ti₂AlC ceramic bolts was equal to be 50 ± 2 MPa. The tensile strength of the mica bolts was equal to be 18 ± 5 MPa, and that of the Al₂O₃ bolts was 34 ± 9 MPa. Ti₂AlC ceramic bolts had higher strength than the Al₂O₃ and mica bolts. Figure 6-12 shows appearance of the broken Ti₂AlC ceramic bolt. Figure 6-13 shows SEM images of the broken Ti₂AlC ceramic bolt and mica bolt. All Ti₂AlC ceramic bolts and mica bolts broke at the first thread of the male thread.

6.4 Dissection

Mechanical strength is important for threaded components. Ti_2AlC ceramic nuts and bolts have higher mechanical strength than commercially available ceramic and some light alloy threaded parts. Further improvements in mechanical strength are important for the widespread use of Ti_2AlC ceramic bolts and nuts. Ti_2AlC ceramic nuts and bolts may be able to further improve the mechanical strength. All bolts fractured at the first thread of the male thread. This failure mode was consistent with that of common bolts, and no special failure phenomena occurred. However, the failure mode of the Ti_2AlC ceramic nut is not shear failure of the threads, which generally occurs at the time of screw failure. Nut parts are generally destroyed from the threaded part. Ti_2AlC ceramic nuts are destroyed by axial displacement. Increasing the circumferential thickness may be an effective way to increase the strength of Ti_2AlC ceramic nuts.

The properties of Ti_2AlC ceramics may be used to improve mechanical strength. Ti_2AlC ceramics have self-healing capability [10-11]. Ti_2AlC ceramics can self-heal machining damage by heat treatment after cutting or by use in high-temperature environments. Therefore, heat treatment on Ti_2AlC ceramic bolts and nuts may improve their strength. As discussed in Chapter 2, Ti_2AlC ceramics have high oxidation resistance by controlling the amount of Al and added elements. Ti_2AlC bolts and nuts with cutting surface have higher strength than commercially available ceramic and light metal screw parts. Ti_2AlC ceramics based on materials design strategy are expected to be used as a substitute for High-temperature threaded parts.

The measurement of properties important for screw components is necessary for the social implementation of screw components made of Ti_2AlC ceramics. Creep test, junker vibration test and torque tests have not been conducted on Ti_2AlC ceramic

screw parts. These tests will be conducted in the future. The widespread use of screw parts made of Ti_2AlC ceramics with these excellent characteristics is expected to not only reduce CO_2 emissions from individual products and improve energy and resource efficiency by reducing product weight and increasing product life but also to form a CE, replacing the recycling economy.

6.5 Conclusions

Demand for ceramic threaded parts as heat-resistant lightweight screws is expected to increase. Ti_2AlC ceramics has many excellent properties and is expected to be applied as a ceramic screw material. Ti_2AlC ceramics with high oxidation resistance and machinability were prepared based on the material design strategies discussed in Chapter 5. The features of the Ti_2AlC ceramic screw parts are as follows:

- Low machining cost because of precision machining with commercially available cemented carbide tools.
- Higher mechanical strength than glass-bonded mica bolts and commercially available alumina bolts and nuts.
- Excellent resistance to oxidation and corrosion, allowing use in high-temperature and corrosive environments.
- Self-healing capability means that cracks heal automatically in an oxidizing atmosphere, making them easy to reuse.

The widespread use of screw parts made of Ti_2AlC ceramics with these excellent characteristics is expected to not only reduce CO_2 emissions from individual products and improve energy and resource efficiency by reducing product weight and increasing product life but also to form a CE, replacing the recycling economy.

References

- [1] Trade statistics of Japan, Ministry of Finance Japan (2021)
- [2] I. Takeshi, Evaluation model to calculate duplicated effect of CO₂ reduction countermeasures of road transportation, *Journal of Environmental Information Science* 25 (2011) 365-370
- [3] S. Malkin, T.W. Hwang, Grinding mechanisms for ceramics, *CIRP Annals* 45 (1996) 569–580.
- [4] J.B. Davis, D.B. Marshall, R.M. Housley, P.E.D. Morgan, Machinable ceramics containing rare-earth phosphates, *J. Am. Ceram. Soc.* 81 (1998) 2169–2175.
- [5] K. Chihiro Y. Akira, Machinability of High-Strength Porous Silicon Nitride Ceramics, *Journal of the Ceramic Society of Japan.* 106 (1998) 1135–1137.
- [6] M.W. Barsoum, MAX phases: properties of machinable ternary carbides and nitrides, Wiley-VCH, Weinheim, 2013.
- [7] N. Yamaguchi, M. Okada, K. Yanagisawa, Y.-L. Kuo, M. Nanko, New material for screws –The potential of Ti₂AlC ceramic screw components, *J. Jpn. Soc. Precis. Eng.* 87 (2021) 353–357.
- [8] S.S. Hwang, S.C. Lee, J.H. Han, D. Lee, S.W. Park, Machinability of Ti₃SiC₂ with layered structure synthesized by hot pressing mixture of TiC_x and Si powder, *J. Eur. Ceram. Soc.* 32 (2012) 3493–3500.
- [9] C.F. Hu, Y.C. Zhou, Y.W. Bao, Material removal and surface damage in EDM of Ti₃SiC₂ ceramic, *Ceram. Int.* 34 (2008) 537–541.

- [10] T. Osada, A. Watabe, J. Yamamoto, J.C. Brouwer, C. Kwakernaak, S. Ozaki, S. van der Zwaag, W.G. Sloof, Full strength and toughness recovery after repeated cracking and healing in bone-like high temperature ceramics, *Sci. Rep.* 10 (2020) 18990.
- [11] S. Li, G. Song, K. Kwakernaak, S. van der Zwaag, W.G. Sloof, Multiple crack healing of a Ti_2AlC ceramic, *J. Eur. Ceram. Soc.* 32 (2012) 1813–1820.
- [12] Technical Ceramics Characteristics Table, NGK SPARK PLUG CO., LTD. OC-2111(8)-0904.

Table 6-1 Typical properties of Ti_2AlC , mica and Al_2O_3 .

	Ti_2AlC (A11.2)	Mica[12]	Al_2O_3 [12]
Bending strength MPa	376	100	350
Young's modulus GPa	248	50	320
Fracture toughness $MPa\ m^{1/2}$	6.9	-	4
Machinability	◎	○	✕

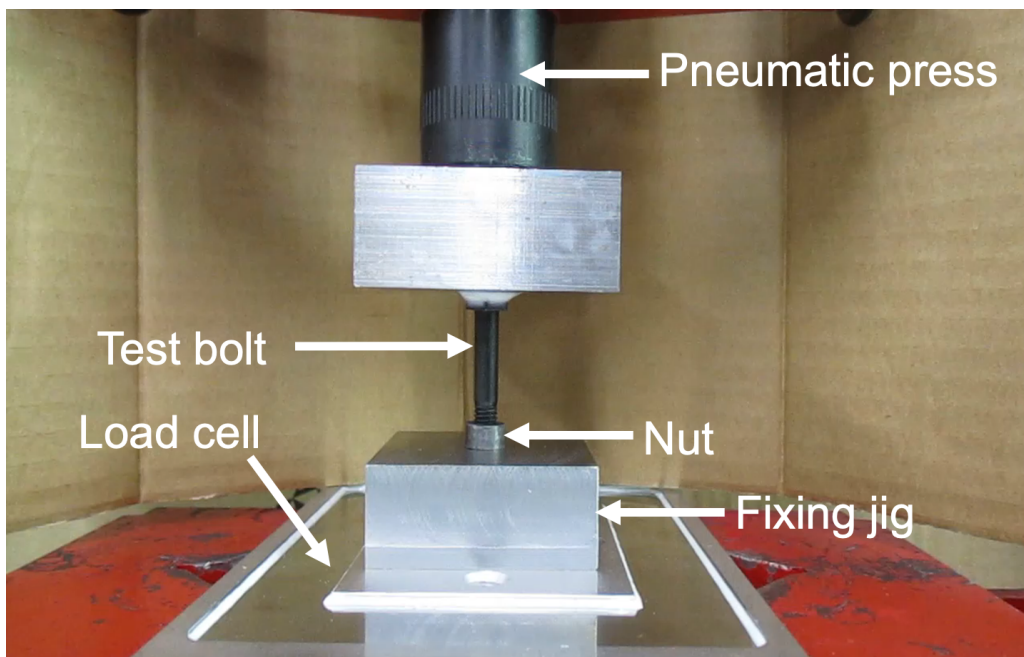


Figure 6-1 Appearance of the compression test equipment.

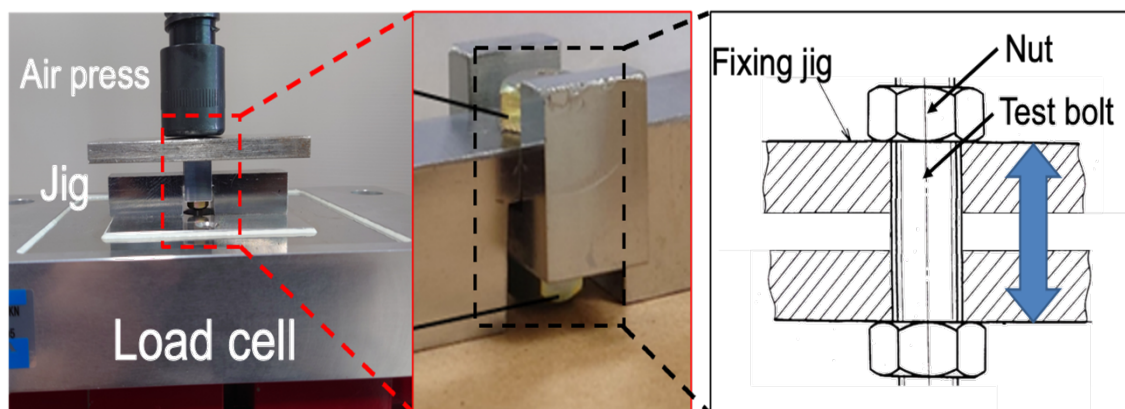


Figure 6-2 Appearance of the tensile test equipment.

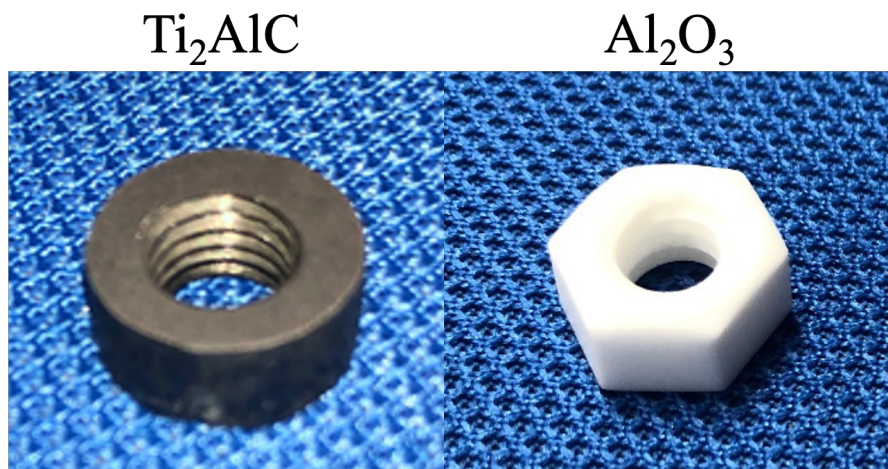


Figure 6-3 Appearance of the Ti_2AlC ceramic nut and Al_2O_3 nut.

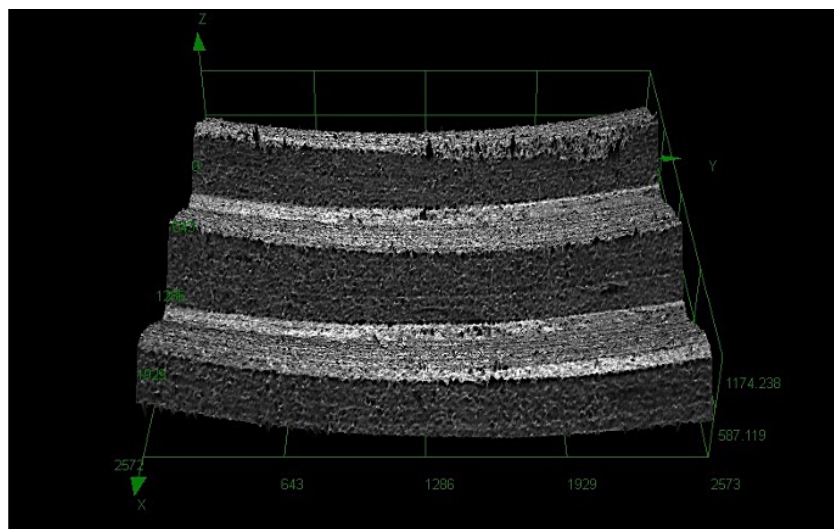


Figure 6-4 3D image of a threaded part of a Ti_2AlC ceramic nut.

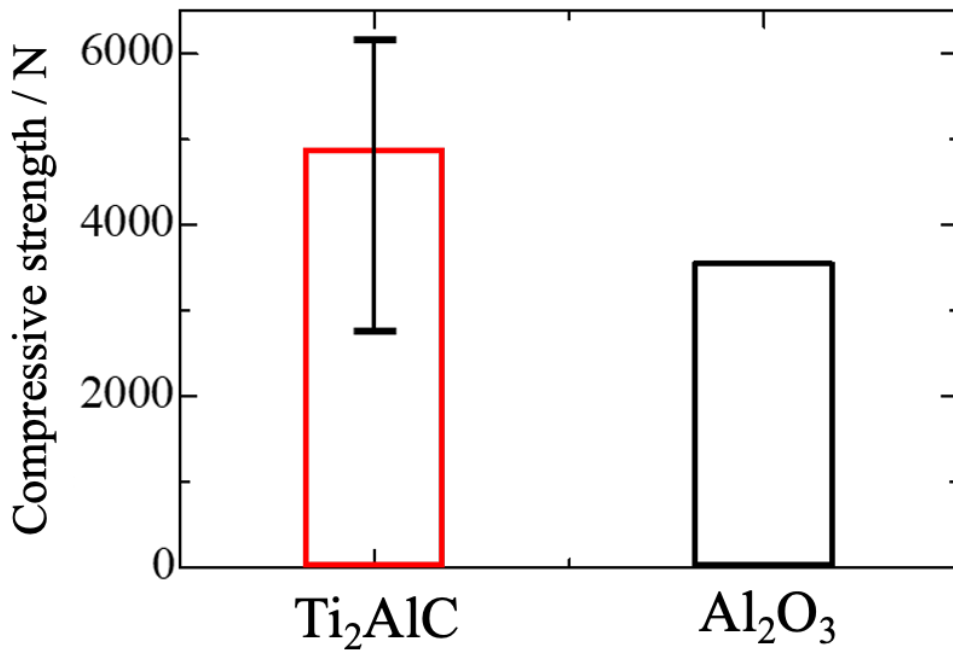


Figure 6-5 Compressive strength of Ti_2AlC ceramic nut and Al_2O_3 nut.

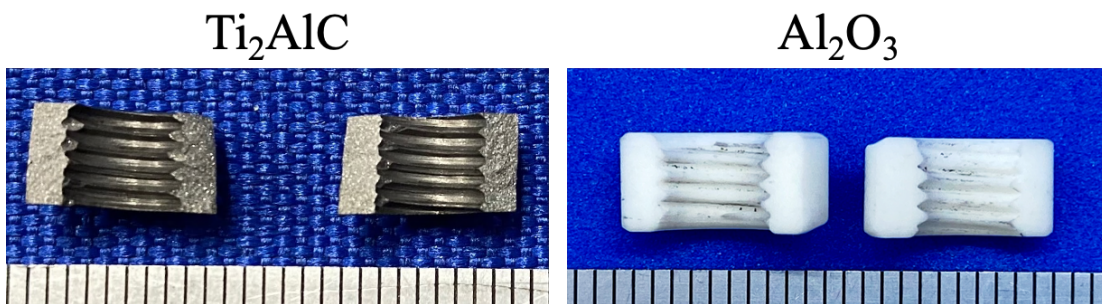


Figure 6-6 Appearance of a piece of nut after a compression test.

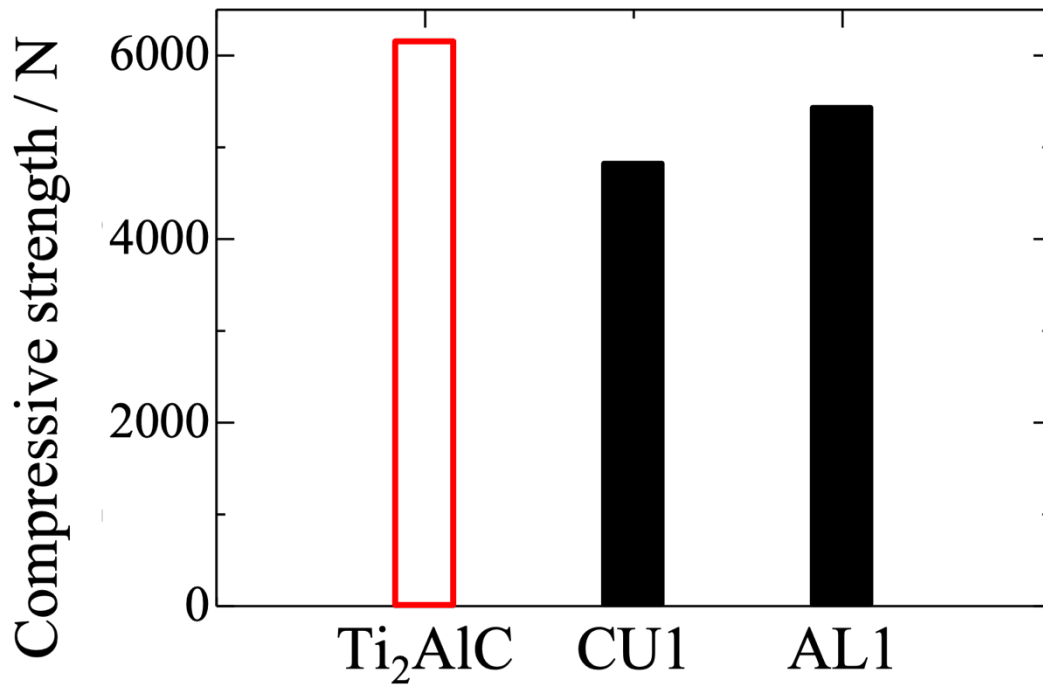


Figure 6-7 Compressive strength of Ti₂AlC ceramics nut, CU1 (Electroplated copper) and AL1 (Aluminum alloy).

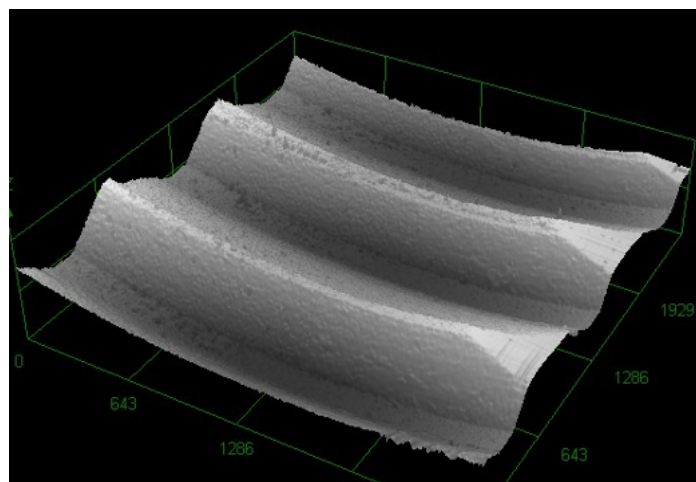


Figure 6-8 Laser microscope image of the threads of a piece of Ti₂AlC ceramics nut after a compression test.

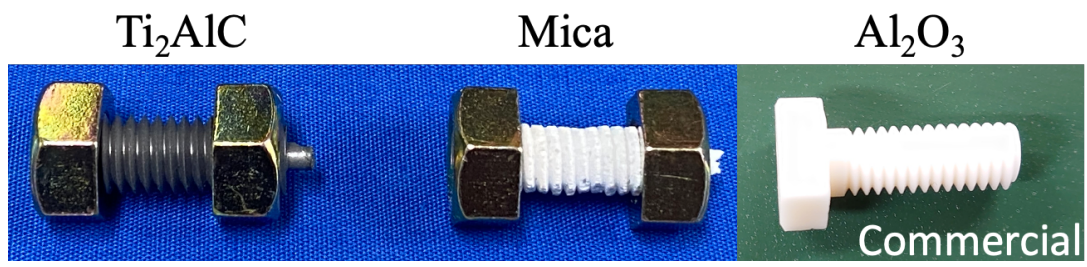


Figure 6-9 Appearance of the Ti₂AlC ceramic nut, mica nut and Al₂O₃ nut.

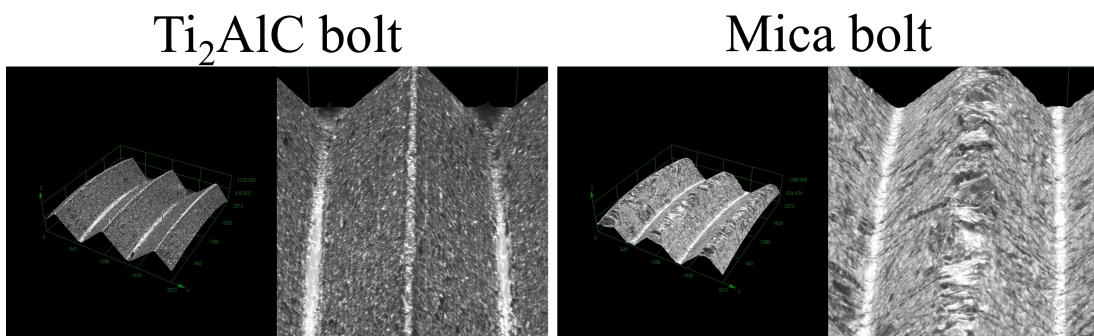


Figure 6-10 3D image of a Ti₂AlC ceramic bolt thread and mica bolt thread.

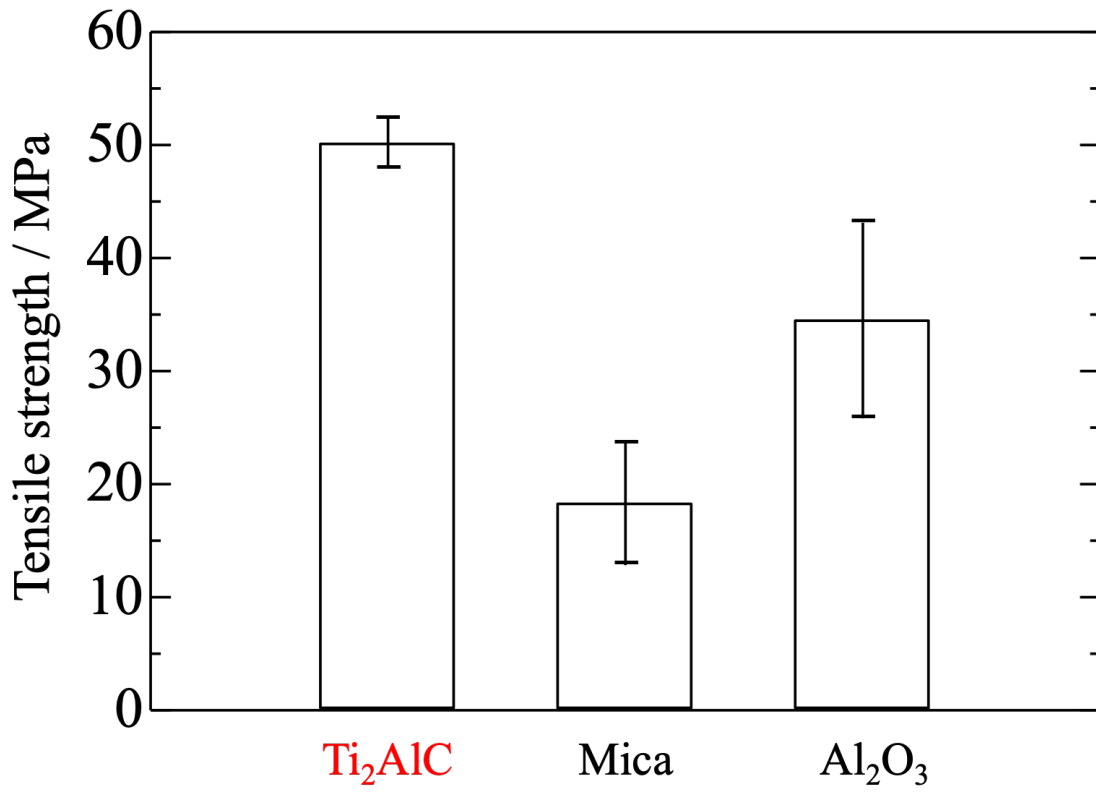


Figure 6-11 Tensile strength of the Ti₂AlC ceramic bolt, mica bolt and Al₂O₃ bolt.

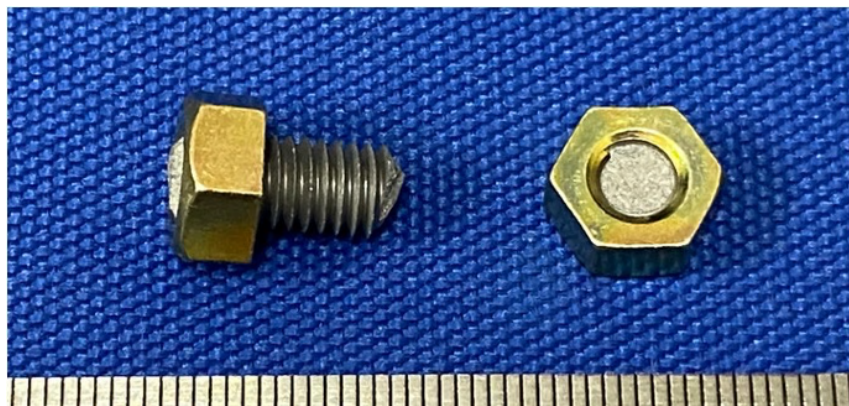


Figure 6-12 Appearance of the broken Ti₂AlC ceramic bolt.

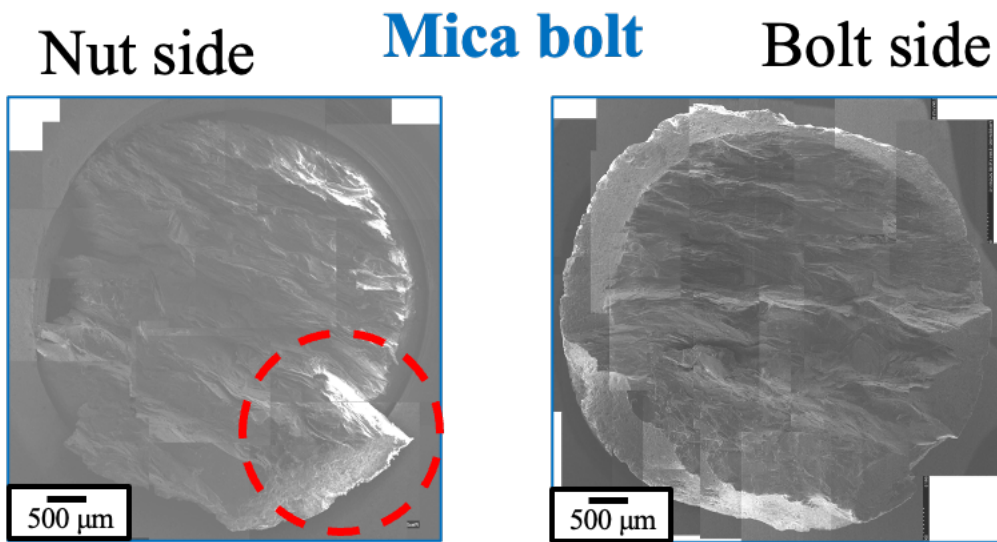
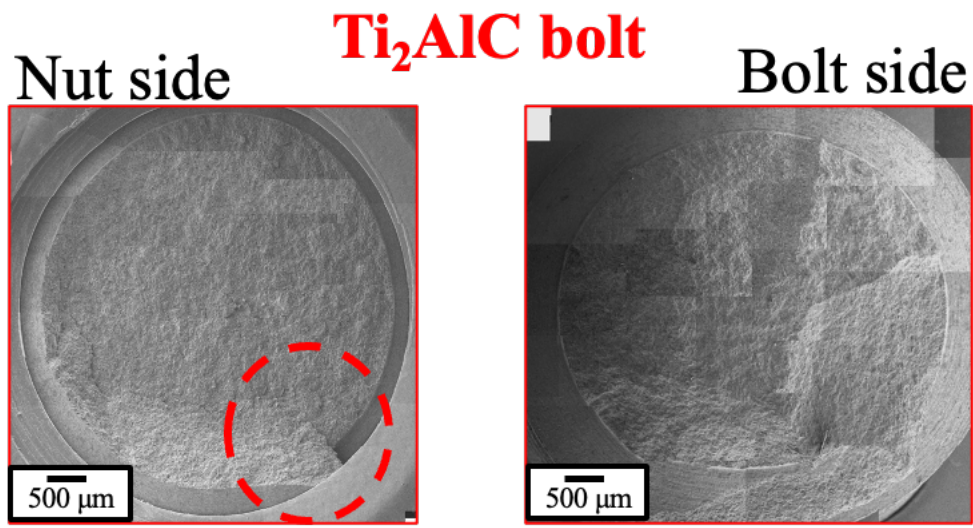


Figure 6-13 SEM images of the broken Ti₂AlC ceramic bolt and mica bolt.

Chapter 7: Summary and conclusions

7.1 Conclusions of the present thesis

The main objective of this thesis is to establish a materials design strategy for Ti_2AlC MAX phase ceramics and to fabricate products based on the strategy. The effects of microstructure control and composition adjustment on high-temperature oxidation resistance, mechanical strength, and machinability were investigated to establish a materials design strategy for high-temperature components. The materials design strategy was then applied to high-temperature screw parts and their properties were evaluated.

In chapter 1, the actual conditions of social implementation of Ti_2AlC ceramic products and concept of materials design strategy are described.

Chapters 2, 3 and 4 discussed oxidation resistance, mechanical strength, and machinability, which are properties especially needed to establish materials design strategy for high-temperature components. In Chapter 2, It was found that Ti_2AlC with high Al concentration has good oxidation resistance and addition of Nb prevents non-protective oxidation of Ti_2AlC with low Al concentrations. This result is useful for stabilizing the oxidation resistance of Ti_2AlC . In Chapter 3, it was found that bending strength is improved by dispersing TiC grains and as well, Nb does not affect mechanical strength. This result is useful for improving the mechanical strength of Ti_2AlC . In Chapter 4, It was found that Ti_2AlC can be cut under the same conditions as graphite and JIS-SKD61 and the bending strength of Ti_2AlC does not decrease

significantly after cutting. These results suggest that Ti_2AlC ceramics were shown to be highly practical machinable ceramics that do not significant reductions in bending strength upon machining. This means that Ti_2AlC ceramics may not require subsequent polishing to remove the machining affected zone.

In Chapter 5, the materials design strategy for high-temperature components was developed based on the results of Chapters 2, 3 and 4. In Chapter 6, the properties of Ti_2AlC ceramic bolt and nut fabricated based on the materials design strategy were evaluated. It was found that Ti_2AlC has better machinability than mica and Ti_2AlC ceramics bolt and nut has higher strength than commercial alumina bolt and nut. These results suggest that Ti_2AlC ceramics is suitable for heat-resistant screw components.

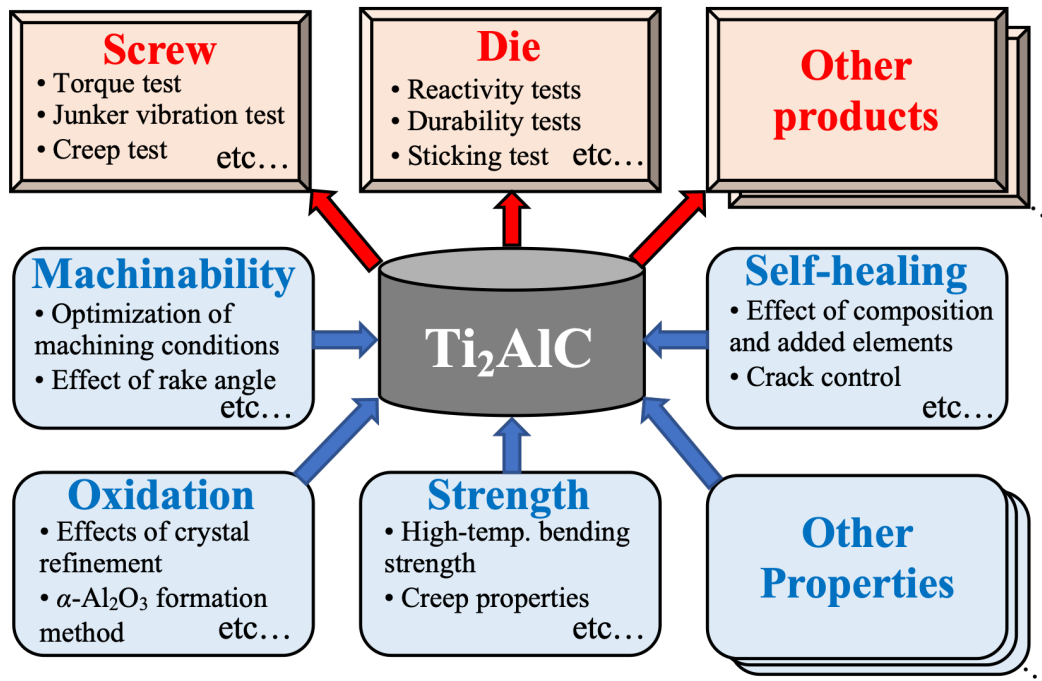
All the results obtained in this work show that controlling minor phases and additives improves the properties of Ti_2AlC . The precipitation of Al-rich phases and the addition of Nb dramatically improved the oxidation resistance at high-temperatures. The mechanical strength was improved by controlling the grain size by adjusting the amount of Ti-rich phase, which tends to generate a pinning effect. Fracture mechanics analysis was also performed to confirm that the mechanical strength of Ti_2AlC does not deteriorate drastically after cutting. The Ti_2AlC ceramic screw parts fabricated based on the material design guidelines showed superior characteristics to conventional screw parts. Therefore, promising materials design strategy have been established for high temperature components.

7.2 Future research

The future challenge for Ti_2AlC ceramics is the mass production of high quality Ti_2AlC powder prepared in the present study. The synthesis of Ti_2AlC powder may fail due to a self-propagating reaction. Thermal shock and expansion of synthesis pellets caused by the self-propagating reaction may destroy the synthesis equipment. The synthesis method must be optimized. Ti_2AlC is a line phase and every Ti_2AlC synthesized powder contains other phases, such as TiC , Ti_3AlC_2 or $TiAl_3$. This makes studying Ti_2AlC using Ti_2AlC synthesized powder with a controlled phase ratio necessary. The synthesis method described in this thesis can be used to control minor phases. The results of this study will contribute to the future development of Ti_2AlC synthesis. Another problem in commercializing Ti_2AlC ceramics is the need for more data on their several properties and performance. Figure 7-1 shows the several properties and performance of Ti_2AlC ceramics that require further investigation. For oxidation resistance, the effect of crystal refinement on oxidation resistance, oxidation resistance in atmospheres other than air and the $\alpha-Al_2O_3$ formation method are necessary to be investigated immediately. For mechanical strength, high temperature bending strength tests, creep tests and fatigue tests are necessary. With respect to machining process, optimization of the machining conditions and the proper tool selection are necessary. Self-healing ability of Ti_2AlC ceramics is also important. Crack introduction methods and the effects of additive elements and composition on self-healing performance should be investigated. For applying Ti_2AlC ceramics into a specific product, the proper properties and performance required for that product must be investigated. Ti_2AlC ceramic samples with low variation in individual properties and performance are essential. The present thesis shows the variation of important properties

of Ti_2AlC can be controlled. The understanding in the present thesis can help to make breakthrough in research and product development of Ti_2AlC ceramics. The results of this thesis will be used to further elucidate the properties of Ti_2AlC ceramics and develop new products.

Social implementation



Investigation of Ti₂AlC properties

Figure 7-1 Properties of Ti₂AlC ceramics that require further investigation.

Nomenclature

K_p : Parabolic oxidation rate constants

θ : Diffraction angle

I : Intensity

t : Time

T^{-1} : Reciprocal temperature

x : Scale thickness

K_{IC} : Fracture toughness

F : Geometric factor

σ_b : Maximum stress

a : Notch depth

W : Specimen height

α : a divided by W

c_g : Grain size of the minor axis

a_g : Grain size of the major axis

σ_F : Tree point bending strength

σ_y : Yield strength

d : Grain size

σ_0 : Internal strength

k : Constant

c : Crack size

σ_0 : Strength of the specimen without surface cracks

R_a : Arithmetic mean roughness

R_z : Ten-point average roughness

R_{sk} : Skewness

R_q : Root mean square roughness parameter

Y_i : Height of the profile at point i

a_e : Equivalent crack size

List of tables and figures

Tables

Table 1 Summarizing the reported mechanical strength of Ti_2AlC ceramics.

Table 2-1 Sample symbols and categories.

Table 2-2 Parabolic rate constants of oxidation (k_p) of all samples determined after 150 h of isothermal oxidation in laboratory air at 800°C.

Table 6-1 Typical properties of Ti_2AlC , mica and Al_2O_3

Figures

Figure 1-1 Constituent elements of MAX phase ceramics.

Figure 1-2 TRL of Ti_2AlC ceramics.

Figure 1-3 Synergy map of my research on Ti_2AlC ceramics.

Figure 1-4 Structure of the thesis.

Figure 2-1 X-ray diffraction patterns recorded for bulk samples: A11, A11.2, A11.5, A11Nb and A11.2Nb.

Figure 2-2 Magnified images of Ti_2AlC and Nb-doped Ti_2AlC samples with various Al molar ratios after 2-14d of isothermal oxidation in laboratory air at 800°C.

Figure 2-3 X-ray diffraction patterns recorded for samples A11, A11.2, A11.5, A11Nb and A11.2Nb after 14 d of isothermal oxidation in laboratory air at 800°C.

Figure 2-4 SEM and EDS images of the cross-sections of samples A11.2, A11Nb and A11.2Nb after 14 d of isothermal oxidation in laboratory air at 800°C.

Figure 2-5 SEM and EDS images of the surface of Al_{1.2}Nb after 14 d of isothermal oxidation in laboratory air at 800°C.

Figure 2-6 SEM and EDS images of the cross-sections of Al₁ after 14 d of isothermal oxidation in laboratory air at 800°C.

Figure 2-7 Oxide scale thickness (x) versus time (t) for Al₁ oxidized at 800°C for >14 d.

Figure 2-8 Oxidation kinetics for all investigated samples over 150 h of isothermal oxidation in laboratory air at 800°C, presented in a linear plot.

Figure 2-9 Magnified images of Ti₂AlC samples with various Al molar ratios after 0.5-2 d of isothermal oxidation in laboratory air at 1200°C.

Figure 2-10 Magnified images of Al_{1.2}Nb with various Al molar ratios after 1-7 d of isothermal oxidation in laboratory air at 1200°C.

Figure 2-11 X-ray diffraction patterns recorded for Al_{1.2}Nb after 7 d of isothermal oxidation in laboratory air at 1200°C.

Figure 2-12 SEM and EDS images of the cross-sections of Al_{1.2}Nb after 7 d of isothermal oxidation in laboratory air at 1200°C.

Figure 2-13 Oxidation kinetics for Al_{1.2}Nb over 168 h of isothermal oxidation in laboratory air at 1200°C, presented in a linear plot.

Figure 2-14 Arrhenius plot showing the parabolic rate constants determined for the oxidation of Ni₅₀Al₅₀ [19] and the k_p values determined in the present experiment (Table 2-2).

Figure 3-1 X-ray diffraction patterns recorded for bulk samples: Al₁, Al_{1.2} and Al_{1.2}Nb.

Figure 3-2 SEM images of the hand milled and ball milled powder.

Figure 3-3 Grain analysis of Al1 via scanning electron microscopy and backscattered electron diffraction. (a) Inverse pole figure map of the observed section; (b) pole figure of the observed section; (c) grain size distributions along the major and minor axis; (d) aspect ratio distribution (c_g/a_g).

Figure 3-4 Grain analysis of Al1.2 via scanning electron microscopy and backscattered electron diffraction. (a) Inverse pole figure map of the observed section; (b) pole figure of the observed section; (c) grain size distributions along the major and minor axis; (d) aspect ratio distribution (c_g/a_g).

Figure 3-5 Grain analysis of Al1.2Nb via scanning electron microscopy and backscattered electron diffraction. (a) Inverse pole figure map of the observed section; (b) pole figure of the observed section; (c) grain size distributions along the major and minor axis; (d) aspect ratio distribution (c_g/a_g).

Figure 3-6 Grain analysis of ball milled Al1.2 via scanning electron microscopy and backscattered electron diffraction. (a) Inverse pole figure map of the observed section; (b) pole figure of the observed section; (c) grain size distributions along the major and minor axis; (d) aspect ratio distribution (c_g/a_g).

Figure 3-7 Bending tests and fracture surface microstructure. (a) Bending strength and fracture toughness value of ball milled Al1.2, Al1, Al1.2 and Al1.2Nb; the error bars represent standard deviation value values.

Figure 3-8 Scanning electron microscopy (SEM) image of the fracture surface of ball milled Al1.2, Al1, Al1.2 and Al1.2Nb and fracture surface around the fracture origin.

Figure 3-9 Bending strength versus grain length for Ti_2AlC ceramics.

Figure 3-10 Fracture toughness versus grain length for Ti_2AlC ceramics.

Figure 4-1 Composition of the sintered Ti_2AlC ceramic. (a) X-ray diffraction profiles; (b) X-ray diffraction profiles with the bottom portion enlarged; (c) backscattered electron image of the observed section; (d) inverse pole figure map of the observed section; (e) phase map of $TiAl_3$; (f) elemental map of Al in the observed section.

Figure 4-2 Grain analysis of Ti_2AlC ceramics via scanning electron microscopy and backscattered electron diffraction. (a) Inverse pole figure map of the observed section; (b) pole figure of the observed section; (c) grain size distributions along the major and minor axis; (d) aspect ratio distribution (c_g/a_g).

Figure 4-3 Scanning electron microscopy images of the machined Ti_2AlC ceramics. (a) Image of the cutting surface showing the surface roughness measurement along the machining direction; (b) image of the cutting chips.

Figure 4-4 Scanning electron microscopy images of end-mill cutting edge. (a) Image of end-mill cutting edge before cutting; (b) Image of end-mill cutting edge after 10 cuts.

Figure 4-5 Surface roughness measurement of the milled samples. (a) Surface profile of the machined Ti_2AlC ceramics; (b) arithmetic mean roughness (R_a) of the Ti_2AlC ceramics ($N=10$); (c) surface profile of the machined graphite; (d) surface profile of the machined tool steel.

Figure 4-6 Amplitude distributions of the surface profiles of the milled samples: (a) Ti_2AlC , (b) graphite, and (c) tool steel.

Figure 4-7 Bending tests and fracture surface microstructure. (a) Bar graph of the bending strength of the polished and machined Ti_2AlC ceramic samples; the error bars represent the maximum and minimum values. (b) Scanning electron microscopy (SEM)

image of the fracture surface of the machined Ti₂AlC ceramic specimen with the lowest bending strength. (c-d) SEM images of the fracture surface around the fracture origin.

Figure 4-8 Microstructures of polished (top row) and machined (bottom row) Ti₂AlC ceramics specimens. (a,f) Appearance of the polished and machined specimens; (b,g) backscattered electron images of the polishing and cutting surfaces; (c,h) backscattered electron images of the cross-sections; (d,i) backscattered electron diffraction inverse pole figure maps of the cross-sections, (e,f) kernel average misorientation maps of the cross-sections.

Figure 4-9 Schematic of the cutting damage during end-mill cutting of the Ti₂AlC ceramics.

Figure 4-10 Geometric factor (F) vs. aspect ratio and initial crack height and expected F at point A at aspect ratios higher than 1.

Figure 4-11 Minimum strength calculated via nonlinear fracture mechanics and actual bending strength. (a) Comparison of the bending strength of the polished and machined Ti₂AlC ceramics and the minimum strength. (b) Nonlinear fracture behavior of the Ti₂AlC ceramics and crack length.

Figure 5-1 Examples of Ti₂AlC Ceramics Products.

Figure 5-2 Summary of materials design strategy.

Figure 6-1 Appearance of the compression test equipment.

Figure 6-2 Appearance of the tensile test equipment.

Figure 6-3 Appearance of the Ti₂AlC ceramic nut and Al₂O₃ nut.

Figure 6-4 3D image of a threaded part of a Ti₂AlC ceramic nut.

Figure 6-5 Load strength of the Ti_2AlC ceramic nut and Al_2O_3 nut.

Figure 6-6 Appearance of a piece of nut after a compression test.

Figure 6-7 Compressive strength of Ti_2AlC ceramics nut, CU1 (Electroplated copper) and AL1 (Aluminum alloy).

Figure 6-8 Laser microscope image of the threads of a piece of Ti_2AlC ceramics nut after a compression test.

Figure 6-9 Appearance of the Ti_2AlC ceramic nut, mica nut and Al_2O_3 nut.

Figure 6-10 3D image of a Ti_2AlC ceramic bolt thread and mica bolt thread.

Figure 6-11 Tensile strength of the Ti_2AlC ceramic bolt, mica bolt and Al_2O_3 bolt.

Figure 6-12 Appearance of the broken Ti_2AlC ceramic bolt.

Figure 6-13 SEM images of the broken Ti_2AlC ceramic bolt and mica bolt.

Figure 7-1 Properties of Ti_2AlC ceramics that require further investigation.

Research activities

Periodic academic publication

- [1] N. Yamaguchi, J. Dąbek, T. Brylewski, Y. Kuo, M. Nanko, Influences of Al concentration and Nb addition on oxidation behavior of Ti₂AlC ceramics at high temperatures, J. Asian Ceram. (2022) 1-8.
- [2] N. Yamaguchi, T. Osada, Y. Kuo, M. Nanko, Influence of the cutting damage on the bending strength of Ti₂AlC MAX phase machinable ceramics, JCS-Japan (2023)

Other's publication

- [1] 山口直也, 岡田学, 柳澤憲史, 南口誠, 新素材のねじ -Ti₂AlC セラミックスねじ部品の可能性-, 精密工学会誌 2021 年 87 巻 4 号 p. 353-357, 2021 年 4 月
- [2] 山口直也, 岡田学, 柳澤憲史, 郭妍伶, 南口誠, 機械加工が可能なセラミックス製ねじが開く未来 -耐熱軽量 Ti₂AlC MAX 相セラミックスの展望-, 日本ねじ研究協会誌 2022 年第 53 巻第 3 号 p.81-89, 2022 年 4 月
- [3] H.Saito,T.Kuribayasi, K. Kaneko, N. Yamaguchi,H. Kawasaki, M. Nanko, Electrical Discharge Machining by Using MAX Phase Ceramic Tool Electrodes, International Journal of Electrical Machining, 25 (2020) 21-26.

[4] K. Kensei, R. Tamura, S. Takeru, K. Keita, K.Kotaro, N. Yamaguchi, M. Nanko, Evaluation of Releasability Between Molding Resin and MAX Phase Ceramics, Transactions on GIGAKU. 9:2 (2021) 1-8.

International Conference Presentations

[1] N. Yamaguchi, T. Brylewski, J. Dąbek and M. Nanko, Oxidation Behavior of Ti_2AlC MAX Phase Ceramics at 800 and 1200°C in Air, Pacific rim meeting on electrochemical and solid state science 2020(PRiME 2020), C02-1193,Online, 2020 October 6 (Oral presentation).

[2] N. Yamaguchi, T. Brylewski, J. Dąbek ,M. Nanko, Influences of Al concentration and Nb addition on oxidation behavior of Ti_2AlC ceramics, 8th International Congress on Ceramics (ICC8), A20210114-3725, Online, 2021 April 29 (Oral presentation).

[3] N. Yamaguchi, M. Nanko, The potential of Ti_2AlC MAX phase ceramics for the root technology (HyMaP 2021), C02-1193,Online, 2021 August 5 (Oral presentation).

[4] N. Yamaguchi, T. Brylewski, J. Dąbek, Y. Kuo, M. Nanko, Influence of Al_2O_3 scale on high-temperature oxidation of Ti_2AlC MAX phase ceramics, International Symposium on High-temperature Oxidation and Corrosion 2022 (ISHOC-2022), Takamatsu, 2022 October 21 (Oral presentation).

- [5] N. Yamaguchi, S. Okumura, K. Iihara and M. Nanko, High temperature oxidation resistance of Ti_3AlC_2 Ceramics coated with C and BN powder, International Symposium on High-temperature Oxidation and Corrosion2018, 2018 October 26 (Poster presentation).
- [6] N. Yamaguchi, S.Okumura, K.Iihara and M. Nanko, Influences of C and BN powder coating on high-temperature oxidation of Ti-Al-C MAX phase ceramics, The 20th International Symposium on Eco-Materials Processing and Design, 2019 January 5 (Poster presentation).
- [7] N. Yamaguchi and M. Nanko, Influence of machining on bending strength of Ti_2AlC and Ti_3AlC_2 MAX phase ceramics, XVI ECerS CONFERENCE, 2019 June 20 (Poster presentation).
- [8] N. Yamaguchi and M. Nanko, High temperature oxidation behavior of Ti_2AlC MAX phase ceramics with various Al concentration, Gordon Research Conference, 2019 July 21 (Poster presentation).
- [9] N. Yamaguchi and M. Nanko, The MAX phase ceramics to achieve a circular economy, 4th STI-Gigaku2019, 2019 November 18 (Poster presentation).
- [10] N. Yamaguchi and M. Nanko, Life Cycle Assessment of Ti_2AlC MAX Phase Ceramics, 5th STI-Gigaku2020, 2020 October 30 (Poster presentation).

[11] N. Yamaguchi, H. Kawasaki, M. Nanko, Oxidation resistance of Ti_2AlC MAX phase ceramics with different phase composition, High Temperature Corrosion and Protection of Materials, 2021 April 1 (Poster presentation).

Domestic Conference Presentations

[1] 山口直也, 奥村駿介, 飯原和喜, 南口誠, 出発組成の異なる Ti_2AlC のパルス通電焼, 日本セラミックス協会第 31 回秋季シンポジウム, 2018 年 9 月 7 日(口頭発表)

[2] 山口直也, 奥村俊介, 飯原和喜, 南口誠, 出発組成の異なる Ti_2AlC 焼結体の切削面粗さ, 日本金属学会 2018 年秋期講演大会, 2018 年 9 月 19 日 (ポスター発表)

[3] 山口直也, 奥村駿介, 飯原和喜, 南口 誠, MAX 相セラミックスのパルス通電焼結に対する焼結条件の影響, 粉体粉末冶金協会 平成 30 年度秋季大会, 2018 年 10 月 31 日 (口頭発表)

[4] 山口直也, 奥村駿介, 飯原和喜, 南口 誠, Ti_3AlC_2 MAX 相セラミックスの曲げ強度における切削加工面表面粗さの影響, 日本金属学会北陸信越支部・日本鉄鋼協会北陸信越支部総会, 2018 年 12 月 1 日 (口頭発表)

[5] 山口直也, 南口誠, 1200°C大気中で酸化試験を行った際の Ti_2AlC MAX 相セラミックスの酸化特性, 日本金属学会 2019 年春期講演大会, 2019 年 3 月 22 日 (口頭発表)

[6] 山口直也, 南口誠, 出発組成の異なる Ti_2AlC MAX 相セラミックスの耐酸化性, 日本金属学会 2019 年秋季講演大会, 2019 年 9 月 11 日 (口頭発表)

[7] 山口直也, 川崎裕貴, 南口誠, Ti_2AlC MAX 相セラミックスの曲げ強度における切削加工面表面粗さの影響, 日本金属学会 2020 年秋期講演大会, 2020 年 9 月 18 日 (口頭発表)

[8] 山口直也, 南口誠, 粒径微細化による Ti_2AlC MAX 相セラミックスの曲げ強度向上, 日本金属学会北陸信越支部・日本鉄鋼協会北陸信越支部総会, 2020 年 12 月 5 日 (口頭発表)

[9] 山口直也, T. Brylewski, J. Dąbek, 南口誠, Ti_2AlC MAX 相セラミックスの耐酸化性における Nb 添加の影響, 日本金属学会 2021 年春期講演大会, 2021 年 3 月 19 日 (口頭発表)

[10] 山口直也, 郭妍伶, 南口誠, Ti_2AlC の耐酸化性と曲げ強度に及ぼす Nb 添加の影響, 日本金属学会 2021 年秋期講演大会, 2021 年 9 月 17 日 (口頭発表)

[11] 山口直也, 吉竹巧, 吉崎滉祐, 郭妍伶, 南口 誠, MAX 相セラミックスのパ
ルス通電焼結とその特性評価, 日本学術振興会 先進セラミックス第 124 委員会,
2021 年 12 月 16 日 (口頭発表)

[12] 山口直也, 郭妍伶, 南口誠, MAX 相セラミックスの社会実装による循環型
経済の構築, 大学院教育改革フォーラム 2021, 2022 年 1 月 8 日 (口頭発表)

[13] 山口直也, 須貝龍太郎, Jaroslav Dąbek, Tomasz Brylewski, 郭妍伶, 南口
誠, Ti_2AlC セラミックスの耐酸化性における組成制御と Nb 添加の影響, 日本金属
学会 2023 年春期講演大会, 2023 年 3 月 8 日 (口頭発表)

Acknowledgments

I would like to thank Professor Makoto Nanko of Nagaoka University of Technology for his kind and precise guidance in research and thesis writing and for providing other opportunities for study abroad and collaborative researches. I would like to express my sincere gratitude to Prof. Yukio MIYASHITA, Prof. Hiromi ISOBE and Associate Prof. Tomoyuki HOMMA of Nagaoka University of Technology and Dr. Toshio OSADA of NIMS, who kindly agreed to review this paper despite their very busy schedules and gave me a lot of advice. I would like to express my sincere gratitude to Assistant Prof. Yen-Ling Kuo of Nagaoka University of Technology for her valuable guidance in reviewing and preparing papers and the thesis. I would like to express my sincere gratitude to Associate Prof. Kensei KANEKO of National Institute of Technology, Nagaoka College, Mr. Takuma KOHATA, the technical staff in NIMS and Specially Appointed Prof. Akihiro NINOMIYA of Nagaoka University of Technology for their valuable comments, understanding and support in carrying out this research. I would like to thank Prof. Manabu OKADA and Associate Prof. Kenji YANAGISAWA for their support and advice during my research internship and research at the National Institute of Technology, Nagano College, and Prof. Tomasz Brylewski and Assistant Prof. Jarosław Dąbek for their support and advice during my research internship and research at AGH University. We would like to express our sincere gratitude to them. I would like to express my sincere gratitude to the Japan Student Services Organization and the Scholarship Support Division and Doctoral Program for World-leading Innovative and Smart Education of Nagaoka University of Technology for their support during my student life. I would like to express my sincere gratitude to Ms Yukiko

KATAGIRI of the secretary, my seniors, colleagues and juniors in the laboratory with whom I have shared a lot of time. I would like to express my heartfelt gratitude to all my relatives who have cared for me and supported me from afar. Thank you very much. I would like to express my heartfelt gratitude to my parents and family, who have always looked after me with warmth and love. Thank you very much. Finally, I am grateful for all the encounters I have had in my life. I would like to thank all the people who have been involved in my life. Thank you very much.